1-1-2004

Investigation of Inductively Coupled Plasma as an Atomization Source for Analytical and Fundamental Measurements Using Cavity Ringdown Spectroscopy

Fabio Jerome Mazzotti

INVESTIGATION OF INDUCTIVELY COUPLED PLASMA AS AN ATOMIZATION SOURCE FOR ANALYTICAL AND FUNDAMENTAL MEASUREMENTS USING CAVITY RINGDOWN SPECTROSCOPY

By

Fabio Jerome Mazzotti

A Dissertation
Submitted to the Faculty of
Mississippi State University
In Partial Fulfillment of the Requirements
for the Degree of Doctor of Philosophy
in Engineering Physics
in the James Worth Bagley College of Engineering
and in the Department of Physics and Astronomy

Mississippi State, Mississippi

December 2004

INVESTIGATION OF INDUCTIVELY COUPLED PLASMA AS AN ATOMIZATION SOURCE FOR ANALYTICAL AND FUNDAMENTAL MEASUREMENTS USING CAVITY RINGDOWN SPECTROSCOPY

By

Fabio Jerome Mazzotti

Approved:

David L. Monts Professor of Physics and Astronomy and Graduate Coordinator of the Department of Physics and Astronomy (Director of Dissertation)	G. Marshall Molen Distinguished Professor Electrical and Computer Engineering (Committee Member)
Christopher B. Winstead Associate Professor of Physics and Astronomy University of Southern Mississippi (Committee Member)	Chuji Wang Adjunct Assistant Professor of Physics Assistant Research Professor Diagnostic Instrumentation and Analysis Laboratory (Committee Member)
Nicolas Younan Professor and Graduate Coordinator Electrical and Computer Engineering (Committee Member)	Stephen Foster Associate Professor Chemistry (Committee Member)

W. Glenn Steele
Interim Dean and Professor of the
James Worth Bagley College of Engineering

Name: Fabio Jerome Mazzotti

Date of Degree: December 11, 2005

Institution: Mississippi State University

Major Field: Physics

Major Professor: Dr Christopher B. Winstead

Dissertation Director: Dr David L. Monts

Title of Study: INVESTIGATION OF INDUCTIVELY COUPLED PLASMA AS AN ATOMIZATION SOURCE FOR ANALYTICAL AND FUNDAMENTAL MEASUREMENTS USING CAVITY RINGDOWN SPECTROSCOPY

Pages of study: 143

Candidate for degree of Doctor of Philosophy

Analytical as well as fundamental measurements were performed with an inductively coupled plasma (ICP) using the novel technique of cavity ringdown spectroscopy. A newly designed ICP torch was presented. Limits of detection were measured for elemental mercury, both in an ICP as well as in a cold mercury chemical generator. The efficiency of the technique was compared with laser-induced fluorescence (LIF) in the ICP. Isotopically resolved spectra of uranium were collected with this technique and results were compared to previous studies using LIF. Gas temperature and electron density estimations were done by lineshape measurements on lead atoms in the ICP. Abel inversion technique was used to extract absolute atom densities and ringdown proved to be an excellent candidate for trace detection when coupled with an atomization source. Spectra of hydroxyl radical coming from dissociation of water molecules in air

were recorded and OH density was estimated. The plasma was found to be in local thermal equilibrium by comparing simulated and measured OH emission spectra. Future developments of cavity ringdown with ICP using continuous-wave lasers are discussed.

ACKNOWLEDGEMENTS

It is with great pleasure and honor that I wish to sincerely acknowledge my research advisor, Dr Christopher B. Winstead for the invaluable training that he provided to me and for his constant advice while I was working under his direction. I would also like to thank Dr George P. Miller for hiring me as a graduate candidate and research assistant, as well as Dr David L. Monts for being my dissertation supervisor and for his excellent guidance through the arduous process of dissertation writing.

I also would like to thank the staff of D.I.A.L. for hiring me and for their enthusiasm which enabled a very creative working environment without which none of this work would have been possible.

I also thank all the professors of the M.S.U. Physics Department and of the College of Engineering for providing excellent teaching to me.

Lastly, I would like to express my deep gratitude to my parents and my two brothers who encouraged me and showed support through all my Doctoral work at Mississippi State University as well as my friend Michel for his excellent sense of humor.

TABLE OF CONTENTS

CHAPTER Page

CHAPTER Page

CHAPTER Page

LIST OF TABLES

TABLE Page

LIST OF FIGURES

FIGURE Page

FIGURE Page

FIGURE Page

CHAPTER I

INTRODUCTION

1.1 Research Aim

Since its beginnings, cavity ringdown laser absorption spectroscopy (CRDS) has been used to make measurements on many radicals and molecules, as well as atoms. It is a rather sophisticated technique based on the measurement of the decay of a laser beam injected into an optical cavity. In 1988, O'Keefe and Deacon proved the high potential of the technique by measuring doubly forbidden electronic transitions in molecular oxygen with sub-ppm absorption sensitivity. It is an absorption technique based on Beer's law and its extreme sensitivity originates from the great number of passes made by the laser beam, or equivalently, to the long residence time of the laser pulse in an optical cavity. Since, unlike standard absorption, the measured quantity is a decay time rather than light intensity, it does not suffer from pulse-to-pulse laser intensity fluctuations that are non-negligible when pulsed lasers are used. Since its invention, cavity ringdown has been used to make very sensitive measurements on tens of molecules and radicals, such as O_2,[1,2,3] H_2O,[4] NO_2,[4] CO,[5] NH_2,[6] NH_3,[7] CH_4,[8] and $C_6H_5O_2$ [9] to name a few. Among these

molecules and radicals, OH [10] was extensively studied through a series of measurements that will be described in further detail below.

The aim of this work is to extend the use of cavity ringdown to the analytical atomic absorption field as well as to demonstrate that it is an excellent plasma diagnostic tool. The main challenge in this work is to adapt cavity ringdown to an atomization source, such as a plasma, which has been shown to make the experimental baseline unstable. For such studies, a well-known, widely used and commercially available atomization source, such as the inductively coupled plasma (ICP), has been used. For some elements, heated gas and use of reagents will be enough to achieve atomization. For these elements, CRDS using a graphite furnace is worth investigating for its simplicity of design.

1.2 Experimental Technique

Ringdown was originally conceived in the early 1980s to measure the reflectivity of highly reflective mirrors which are used for several different applications, such as ring gyroscopes in civilian and military aviation. The accuracy of the gyro was determined in part by the length of the residence time of the light beam within the ring cavity which depends on the mirror reflectivity. In 1980, Herbelin et al.[11] demonstrated a novel phase shift method that could accurately measure the reflectivity of a pair of highly reflective mirrors with an accuracy of 0.01%. In 1984, Anderson et al.[12] designed an experimental setup that could measure mirror reflectivity with an accuracy of 0.0005%. Their setup consisted of a pair of mirrors that faced each other, a Pockels cell shutter, a polarizer and a pair of mode matching lenses. The laser source couples randomly into the cavity, as it would in an interferometer, when the intracavity power reaches a certain threshold, the

Pockels cell is set to shut off transmission of the beam and a transient, or ringdown, is measured. Assuming that the response time of the Pockels cell is short relative to the cavity decay time, a decreasing exponential signal is then obtained.

Consider an empty optical cavity formed by two mirrors facing each other. If we inject a laser pulse that we take to be of short duration for explanatory purposes, we will observe its intensity decrease exponentially according to the following relationship:

$$i(t)=i_0 \bullet e^{-2 \bullet loss/reflection \bullet number\ of\ round\ trips} \tag{1.1}$$

That is, at each reflection, the light intensity will decrease by a factor equal to the loss at the mirror surface. Figure 1.2-2 is a schematic diagram of a ringdown setup. A light detector placed behind the back mirror will measure a signal proportional to $i(t)$, namely a decreasing exponential with time. The above formula will explicitly be

$$i(t) = i_0 \cdot e^{-\left[(1-R)\frac{tc}{2}\right]} \tag{1.2}$$

at each round-trip, where R is the reflectivity of the mirrors, t time and c the speed of light. The measured function of time is shown in Figure 1.2-1 as a succession of peaks.

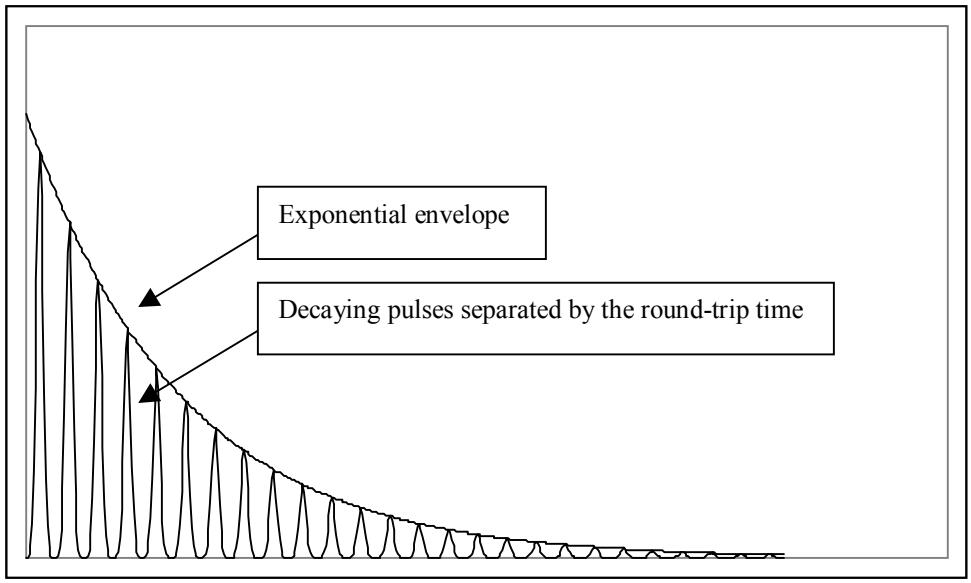

Figure 1.2-1. Schematic representation of the ringdown pattern produced by a short laser pulse injected into the cavity

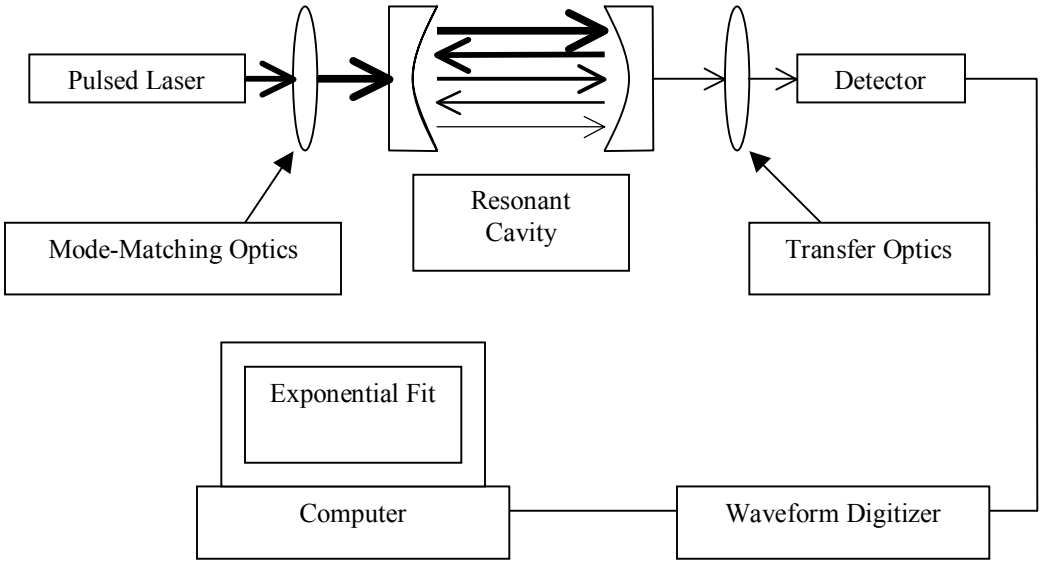

Figure 1.2-2. Schematic diagram of a cavity-ringdown setup using a pulsed laser source.

In case the pulse duration is longer, one obtains an exponential envelope, called a ringdown curve. Such a signal can be digitized and fitted so as to extract the *ringdown*

time τ_0, which by definition is the time needed for the intensity to decrease by a factor of 1/e. In case an absorber with total absorption α_{abs} is present inside the cavity, the newly measured ringdown time τ will experience a drop according to the following equation:

$$\frac{1}{\tau} = \frac{1}{\tau_0} + \alpha_{abs} \cdot \frac{c}{L}, \tag{1.3}$$

where c is the speed of light and L the length of the cavity.

Cavity ringdown spectroscopy gives absolute absorption measurements rather than relative as in standard absorption. The latter property originates from the fact that a decay is measured rather than the intensity. To us, it seems that ringdown is the way absorption measurements should be always made. To give an order of magnitude, 99.99% reflective mirrors separated by a 1 m distance would produce an effective path-length through the whole empty cavity of 10 km during the time constant and a residual time of 33.4μs. An absorbance of 10^{-6} would be readily detectable with a 1% ringdown change, whereas standard absorption would detect at best changes on the order of 10^{-3}.

1.3 Experimental Results

In Chapter II we both describe the general technique of Cavity Ringdown Spectroscopy and we also make a review of it in the literature. In Chapter III, the experimental setup used in the present work is described.

The first part of this study is focused on testing the atomic analytical applicability of cavity ringdown spectroscopy. We tried several atomization systems in conjunction with CRDS and we present our results. Several mercury atomization systems were used and the analytical figures of merit are compared with standard, commercial system performance. It is our goal to test the versatility of CRDS with any of these techniques.

The relatively poor mirror reflectivity over the wavelength range used for mercury and the continuous improvements made in mirror technology makes this technique very promising.

We started with a chemical mercury cold vapor generator and obtained fairly promising results (Chapter IV). First, the chemical or ionic form of mercury is reduced, then heated, mixed with an inert gas and finally flowed through the cavity where absolute absorption measurements were made. With this type of approach, we were able to set up two systems: a continuous (or on-line) one where mercury is flowed continuously and a 'batch' one where inert gas is flowed into a buffer recipient containing a known initial concentration of mercury, so that it is possible to monitor the variation of mercury concentration in the cell with time.

The results with ringdown are directly compared with standard atomic absorption spectroscopy (AAS). For gas phase mercury and a path-length of 18 cm, the detection limit figure of merit found with cavity ringdown is 25 ng/m^3, whereas for standard absorption it is 830 ng/m^3. Hence a factor of thirty three improvement with mirrors that are only 99.7% reflective. Improvement in the mirror coating would easily lead to a two or even a three order of magnitude improvement in the technique compared to standard AAS.

We also successfully interfaced cavity ringdown with a graphite furnace atomizer. The latter is of relatively simple design and is usually interfaced with a standard absorption apparatus: a narrow line-width light source is employed (like a hollow cathode lamp) and a grating disperses the light. This atomization source will generate a short (less than a few seconds), rapidly varying absorption profile signal. The atomic elements we have investigated are Pb and Hg. The results obtained are really encouraging, since we

obtained with CRDS a detection figure of merit almost one order of magnitude better than that reported by Perkin-Elmer data sheets for commercially available AAS systems. These detection limits were obtained with only fair quality mirrors and with a laser repetition rate that was clearly not sufficient to sample the atomization process (at best 20 Hz versus hundreds of Hertz theoretically needed). The desired repetition rate may be reached with already commercially available laser sources.

We also proved that the inductively coupled plasma (ICP) is analytically worthwhile when used with cavity ringdown spectroscopy (Chapter IV). ICP-CRDS has much better detection limits than those obtained with ICP emission spectroscopy (by several orders of magnitude). We also compare cavity ringdown with LIF measurements. LIF sometimes suffers from quenching and also from level branching while CRDS does not. The excitation wavelength and emission wavelength were the same in this experiment (253.7 nm). We varied ICP parameters so as to optimize fluorescence for LIF measurements and absorption for CRDS measurements. With this experiment, we prove that the ICP can be used as an atomic reservoir as well as an ion reservoir, as commonly used. For this, we found that it is sufficient to lower the radio frequency ICP power. A specially designed ‘low-flow’ quartz torch with a wider inner injector was used for this experiment. This torch has the advantage of making the baseline more stable than that from a standard torch.

We also studied isotopic splitting of uranium at three different wavelengths: neutral uranium at 258.49 nm and 409.01 nm, and ionic uranium (UII) at 286.57 nm (Chapter V). At 286.57 nm, we observed the isotopic shift between ^{235}U and ^{238}U. There was an interference in the background (probably OH) that reduced the analytical performance that was at least equal to or better than that of LIF. The background

interference was located near the ^{238}U absorption peak. At 358.49nm, we obtained a detection limit of 300 ppb and could easily resolve the ^{235}U peak from the ^{238}U peak. At 409.01 nm, the isotopic splitting was fairly small (only 0.283 cm^{-1}) and needed better laser linewidth and data processing to be resolved. The latter wavelength is very interesting because of high reflectivities available for the mirrors and also because some small, relatively inexpensive laser diode systems are available at this wavelength. All in all, we also verified that the ICP works as an atom reservoir as well as an ion reservoir.

Line broadening studies were also performed with an atomic lead absorption line in the ICP (Chapter VI). We first obtained Abel inversions of line-of-sight data so as to obtain the radial absorption profile. We also studied the Voigt absorption lineshape so as to obtain the Gaussian and Lorentzian components, corresponding respectively to Doppler broadening and to pressure broadening. From these components, we calculated Pb kinetic temperature as well as Stark broadening. With a simple assumption, we obtained an estimate of the electron density in the plasma.

Lastly, we made a study of OH emission and absorption spectra in the ICP (Chapter VII). The radical mainly comes from dissociation of H_2O molecules. We estimated kinetic temperature by lineshape broadening and excitation temperatures by spectral simulation in emission. The plasma was found to be in local thermal equilibrium, the kinetic and excitation temperatures being approximately the same.

CHAPTER II

CRDS TECHNIQUE DESCRIPTION AND ITS REVIEW IN THE LITERATURE

2.1 Absorption Spectroscopy Techniques and Their Relative Sensitivities

Absorption spectroscopy is based on measurement of the attenuation of electromagnetic energy when radiation passes through a cell containing the sample to be analyzed. Atoms, ions, radicals and molecules will absorb radiation at a wavelength λ_{ik} and will be excited from a lower energy state E_i to an upper energy state E_k. According to the Beer-Lambert absorption law, if I_0 is the light intensity before the sample of absorbance α and of effective pathlength L, the transmitted intensity is $I_{trans}(\lambda) = I_0(\lambda) \cdot e^{-\alpha L}$, so that, with a first-order Taylor expansion of this formula, one obtains for weak absorption:

$$\alpha(\lambda) = \frac{I_0(\lambda) - I_{trans}(\lambda)}{I_0(\lambda) \cdot L} \tag{2.1}$$

The minimal measurable absorbance is hence inversely proportional to the pathlength L and directly proportional to the intensity fluctuations.

To be able to quantify the minimum detectable absorption, we need to introduce some notation. Let $\langle \ldots \rangle$ denote the average of a measurement over the duration of an

absorption measurement. If we call S the absorption signal, then the mean of S is $\langle S \rangle$ and the standard deviation is $\sigma_S = \sqrt{\left\langle \left(S - \langle S \rangle\right)^2 \right\rangle}$. The minimum detectable fractional signal per shot is $MDFS_{shot} = \frac{\sigma_S}{S}$ and the minimum detectable absorption loss per shot is $MDAL_{shot} = \frac{MDFS_{shot}}{L}$, which has units of cm^{-1} if L is in cm. If N shots are acquired, then the minimum detectable absorption loss varies as $1/\sqrt{N}$, that is $MDAL(N) = MDAL_{shot}/\sqrt{N}$, and for a repetition rate of frequency f (Hz), the sensitivity is defined as $S_y = MDAL(f)$, with S_y in $cm^{-1}Hz^{-1/2}$.

Laser spectroscopy is a great improvement over standard absorption spectroscopy where a broadband light source is used in conjunction with a spectrometer. Laser light, which is coherent and spectrally narrow, can be scanned across the absorption line so that no spectrometer is needed. Owing to high laser spectral power density, detector noise becomes negligible in general. Furthermore, laser light can be collimated, allowing the use of long pathlength absorption cells. Therefore, lasers are well suited for the spectroscopy of weak transitions and the measurement of ultralow concentrations, making them an ideal candidate for usage in industry and in medical applications, especially when laser sources are becoming more compact, more reliable, and cheaper.

More complex ways exist to cancel out the excess noise and power drift experienced by single-path absorption spectroscopy. These fluctuations can exceed the shot noise by 50dB. One way to circumvent such noise is to use a dual detector scheme: the initial laser beam is split into sample and reference beams so that spurious modulations and drift can be tracked and cancelled. Such noise cancellation schemes

have been proposed by Hobbs[13] and applied by others[14] for the detection of NO_2, H_2O, and O_2 using diode lasers, with successful noise suppression of as much as 60 dB, leading to $MDAL_{shot}$ of 10^{-8} $cm^{-1}Hz^{-1/2}$.

Another way of increasing the absorption sensitivity is to extend the effective pathlength without increasing the physical cell length. This is done by folding the light path around the input and output surfaces many times with a set of two mirrors. Such setups can easily increase the effective pathlength by a factor of 10-1000; kilometers can be achieved with temperature stabilized cells. One can typically achieve $MDAL_{shot}$ of the order of 10^{-5} to 10^{-7} cm^{-1} with direct detection.[15] This technique still suffers from intensity fluctuations of the light source. Combined with frequency modulation spectroscopy, which will be described below, excellent results can be attained, with $MDAL_{shot}$ values as low as 10^{-10} cm^{-1}.

Frequency modulation (FM) spectroscopy is achieved as follows: the frequency of the laser is modulated around the absorption frequency, so that the laser light will have frequency $\omega_L = \omega_C + \Omega \cdot \sin(\omega_m \cdot t)$ with the condition of small absorbance ($\alpha L << 1$) and of a small modulation amplitude ($\Omega / \omega_C << 1$). Then, the lock-in signal $S(\Omega)$ will directly depend on the derivative of the absorption lineshape $\alpha(\omega)$:

$$S(\Omega) = -\Omega L \frac{d\alpha(\omega)}{d\omega} \sin(\Omega t) \tag{2.2}$$

Such techniques typically lead to sensitivity in the range of 10^{-6}-10^{-7} cm^{-1} ($MDAL_{shot}$). This absorption method is still relative; it is not possible to obtain absolute concentrations unless the system is calibrated.

The last, but not least traditional method is intracavity laser absorption spectroscopy (ICLAS) which relies on placing a narrow linewidth absorber in a broadband active laser cavity. It is a highly sensitive absorption technique whose MDAL is in the range 10^{-6}-10^{-11} cm^{-1}. It has a great advantage versus cavity ringdown in the sense that it can be used with "dirty windows" containing the species to be analyzed. It necessitates rather expensive equipment and is also difficult to realize. Pathlength enhancements of up to 30 km have been achieved. However, ICLAS remains limited by the laser spectral range (300 to 1600 nm), one of the greatest drawbacks in detecting trace pollutants.

Rather than being based on transmitted intensity measurements, cavity ringdown spectroscopy (CRDS) is based on a decay measurement. Hence, it is not, in theory, sensitive to light intensity fluctuations. Furthermore, it is an absolute, self-calibrated technique. The pathlength enhancement originates from the long residence time of the light in a low-loss resonator. Cavity ringdown achieved with pulsed lasers is of moderate cost and is simple to implement. It has been used for many species and has been proved to be ultra-sensitive with sensitivity ranging from 10^{-6} cm^{-1} to 10^{-10} cm^{-1}. It has been thoroughly used. Continuous-wave cavity ringdown (the light source is a continuous laser source) can be more difficult to implement; however its sensitivity range is from 10^{-10} cm^{-1} to 10^{-12} cm^{-1}. Lastly, heterodyne cavity ringdown schemes ought to perform better than $10^{-12}cm^{-1}$, reaching the shot-noise limit.[16,17,18,19,20,21]

In the array of available absorption techniques, cavity ringdown appears as one of the best to use, especially when high sensitivity is needed, as in trace gas detection. It is by far the most sensitive and its ease of implementation as well as its moderate costs

make it an excellent candidate for some specific applications where sensitivity is crucial, namely fundamental physics and chemistry, combustion control, environmental analysis and medical applications.

2.2 Principle of CRDS

2.2.1 Introduction

Used during the seventies to measure mirror reflectivities for military aviation purposes, cavity ringdown has undergone many changes and has been applied since 1988 to measure absorption features of many species including molecules, radicals and atoms. Its sensitivity makes it a good candidate for the following applications:

- Fundamental atmospheric modeling studies
- On-line pollution monitoring
- Detection of chemical warfare agents, explosives or drugs for military purpose
- Combustion control

This technique is based on the Beer-Lambert law of standard absorption stated below. Consider a beam of light passing through a homogeneous gas sample of length L (in cm), of cross section σ (in cm^2), and containing a species under study with a number density N. Then, if I_0 is the incident beam intensity, under Beer's law conditions, the transmitted intensity will simply be:

$$I_t = I_0 \cdot e^{-\sigma NL} \tag{2.3}$$

If the parameter under study is the gas number density N, then one needs to measure I_0 and I_t (the cross-section and the path-length L are considered known). One way to increase the sensitivity of this technique is to make the path-length L as long as

possible by for example, making the beam bounce back and forth through the sample with a pair of mirrors, taking care that the beam does not reflect back onto itself. Sophisticated techniques can be employed to diminish background noise by modulating the incident intensity I_t. However, these direct absorption measurement techniques do not perform as well as cavity ringdown (by a factor of at least 100).

2.2.2 Principle: a Simple Description

Cavity ringdown spectroscopy is based on the measurement of the decay of a light pulse injected into a stable optical cavity composed of two (or more) mirrors. Such a decay is due to the very weak transmission of such high quality mirrors with reflectivity of 99.9% or above. Such a cavity in vacuum will decay with a 1/e time constant τ (often called the ringdown time) given by:

$$\tau = \frac{L}{-\ln R \cdot c}, \tag{2.4}$$

where L is the distance separating the two mirrors facing each other, c the speed of light in vacuum, and R the reflectivity of the two mirrors. When an absorbing species with absorption coefficient α is present inside the cavity with a line-of-sight denoted l_s, with gas uniformly filling the whole cavity with Rayleigh coefficient β, the ringdown time can be expressed as

$$\tau = \frac{L}{c\left(-\ln R + \alpha \cdot l_s + \beta \cdot L\right)}, \tag{2.5}$$

sometimes written as

$$\frac{t_r}{2\left(-\ln R + \alpha \cdot l_s + \beta \cdot L\right)}, \tag{2.6}$$

where t_r is called the round-trip time. Note that all these terms are dependent on the wavelength λ (since $\beta(\lambda) \propto \lambda^{-4}$), so that a scan versus λ will give the absorption line profile. When no absorber is present in the cavity, the ringdown time is simply given by

$$\tau_0 = \frac{L}{c(-\ln R + \beta \cdot L)}, \tag{2.7}$$

so that

$$\frac{1}{\tau} - \frac{1}{\tau_0} = \frac{c}{L} \cdot \alpha \cdot l_s = \frac{c}{L} \alpha_p, \tag{2.8}$$

where α_p is the loss per pass which is given by a straightforward relationship

$$\alpha_p(\lambda) = \frac{L}{c} \cdot \left(\frac{1}{\tau(\lambda)} - \frac{1}{\tau_0(\lambda)} \right), \tag{2.9}$$

when measurements are made with and without the sample in the cavity. Equation (2.3) is valid when Beer's absorption law is valid for the sample so that, when we consider a light pulse making a single pass through the sample, its intensity will experience a factor $e^{-\alpha_p}$ decrease, and after a single pass through the cavity, the total factor will be

$$e^{-\alpha_p} \cdot R \cdot e^{-\beta L} = e^{-(\alpha \cdot l_s - \ln R + \beta L)}, \tag{2.10}$$

within a time frame of $\frac{t_r}{2}$.

When the light pulse duration t_d is smaller than the characteristic time t_r, a fast enough optical detector placed near the end-mirror of the cavity will see an exponentially decaying succession of pulses, rather than an exponential continuous envelope (true when $t_d > t_r$). Note that expression (2.5) does not depend on the light pulse intensity, and hence not on pulse-to-pulse intensity fluctuations, which make this a valid technique to use with pulsed lasers.

2.2.3 A Good Approximation: Ray Optics

Through ray optics formulation, it is possible to deduce a stability condition for an empty optical resonator. Assuming the cavity formed by two mirrors has an optical axis Oz (which is an axis of revolution), a light ray is then simply represented by two quantities: the angle α from the optical axis and its displacement at position z on its optical ray. With paraxial conditions, we can make a first order approximation relatively to the angle α. Let $\begin{bmatrix} r(z) \\ \alpha(z) \end{bmatrix}$ be the matrix element representing the ray. If we consider propagation of the ray through a homogeneous medium of length L, at the location $z' = z + L$, the resulting ray will simply be given by the formula $\begin{bmatrix} r(z') \\ \alpha(z') \end{bmatrix} = N \bullet \begin{bmatrix} r(z) \\ \alpha(z) \end{bmatrix}$ where N is a 2x2 matrix. It is straightforward to verify that $N = \begin{bmatrix} 1 & L \\ 0 & 1 \end{bmatrix}$ (note that the angle α does not change, as expected). The transformation undergone by the ray when it is reflected by a spherical concave mirror is $M_i = \begin{bmatrix} 1 & 0 \\ -\frac{2}{R_i} & 1 \end{bmatrix}$ where R_i is the radius of curvature of the mirror. If we use these results to determine how a ray is changed by successive reflections in a cavity composed by two mirrors of respective radii of curvature $R_{i=1,2}$, we get for the n-th round trip $P^n \bullet \begin{bmatrix} r(z_0) \\ \alpha(z_0) \end{bmatrix}$ where $P = M_2 \bullet N \bullet M_1 \bullet N$, the product of four matrices. It can be proven that, for the cavity to be stable, that is $r(z)$ does not grow indefinitely, we need the condition $0 \le g_1 \cdot g_2 \le 1$ where $g_i = 1 - \frac{L}{R_i}$ (for $i = 1,2$). This condition arises when linearization of matrix P is done. The ray matrix

method is useful when working with White or Herriott absorption cells, where the light is reflected back and forth without crossing its path (unlikely cavity ringdown). This stability condition is very useful for cavity ringdown since it enables us to build a stable cavity; however to fully explain the mechanism going on in the cavity, it is necessary to take into account the mode structure of the electromagnetic field which will be briefly described.

2.2.4 A Modal Description of CRDS

When solving the wave-propagation equation for separable variable solutions and looking for those solutions which remain structurally unchanged after a round-trip in the cavity, one ends up with a whole set of solutions indexed by three integers p,n,m, where:

- p indexes the longitudinal modes and gives the number of nodes of the solution on the optic axis.
- n and m index the transversal modes and gives the number of nodes in the two orthogonal transverse directions of the solution.

Each mode possesses a definite spatial structure as well as a certain frequency. The spatial, transverse structure is given by Hermite polynomials (for rectangular symmetry) or Laguerre polynomials (for cylindrical symmetry). The frequency of a particular mode depends on the mode number and is given in rectangular symmetry by

$$\nu_{pmn} = \frac{c}{2L}\left[p + (n+m+1)\cdot \frac{\cos^{-1}\left(\pm\sqrt{g_1 \cdot g_2}\right)}{\pi} \right] \tag{2.11}$$

One can easily see that the longitudinal mode spacing is $\frac{c}{2L}$ as in a standard Fabry-Perot resonator, and the transverse mode spacing is equal to the term

$$\frac{c}{2L}\cdot\frac{\cos^{-1}\left(\pm\sqrt{g_1\cdot g_2}\right)}{\pi} \tag{2.12}$$

An illustration of the transverse mode spatial profile can be easily found in standard laser books. The expression giving the electromagnetic wave spatial structure $u(x,y,z)$ involves other parameters which are:

- the width of the beam w_0 (distance at which the amplitude of the field drops by a factor of 1/e)
- the Rayleigh distance $z_R=\frac{\pi\cdot w_0^2}{\lambda}$, where λ is the wavelength
- the radius of curvature of the wave front $R(z)=z\cdot\left[1+\left(\frac{z_R}{z}\right)^2\right]$
- a phase factor equal to $\Phi(z)=\tan^{-1}\left(\frac{z}{z_R}\right)$

The beam waist at position z is the given by

$$w^2(z)=w_0^2\cdot\left[1+\left(\frac{z}{z_R}\right)^2\right] \tag{2.13}$$

These parameters do not depend on mode number. To give an example, the m=0, n=0 mode is called TEM_{00} and has a gaussian transverse profile and we simply have

$$|u(x,y,z)|\propto e^{-\frac{x^2+y^2}{w^2(z)}} \tag{2.14}$$

As we will see later, these relationships are very useful for the design of ringdown cavities.

2.3 Literature Review of Cavity Ringdown Spectroscopy

2.3.1 Cavity Ringdown Spectroscopy of Molecules and Radicals

The cavity ringdown technique as we now know it was first reported in a paper written by O'Keefe in which a dye laser emitting at 690 nm was used to measure weak overtone transitions of O_2 using a pair of highly reflective mirrors. The minimum detectable losses reported were only about 2.10^{-8} cm^{-1}. This publication served both as a basic citation and as a reference work for many ringdown experiments and is still very modern today. Since then, many experiments involving CRDS of O_2 have been done. For example, coefficients for pressure broadening of O_2 in N_2 were measured at 688 nm.[22] Polarization spectroscopy was combined with CRD Spectroscopy to measure transitions of molecular oxygen around 628 nm.[23] The oxygen A band was measured by CRD Spectroscopy in magnetic fields up to 20 T.[24] High resolution scans of $^{16}O_2$ and $^{18}O_2$ were recorded[25] to determine accurate line positions. O_2-O_2 collision-induced absorption was also investigated[26] in the 540-650 nm wavelength region from 0 to 730 Torr. Similarly, CRDS measurements of O_2-O_2 collision-induced absorption resonance at 477 nm were performed.[27] Einstein coefficients and integrated absorption were also measured for O_2 .[28] Measurements of the radiative lifetime of O_2 near 1274 nm have also been carried out[29].

Since the first reports, hundreds of ringdown experiments have been successfully performed; the technique has been applied to tens of species (about a hundred, most of them molecules and radicals) with unprecedented accuracy in absorption sensitivity.

O'Keefe et al.[30] presented one of the first CRD spectra of a jet-cooled metal cluster. In their work, they recorded spectra of Cu_2, and Cu_3 and were able to measure bands that in previous LIF studies were weaker, due to predissociation of the upper level.

Romanini et al. reported CRDS of very weak HCN overtone bands[31,32,33] in different spectral ranges. Zalicky et al. made measurements of CH_3 radical in a hot filament reactor at a wavelength of 213.9 nm.[34] The spectroscopy and predissociation dynamics of HNO were studied in another work by CRDS.[35] The electronic spectrum of C_6H was measured [36,37]. Similarly, the C_6H radical was studied in a supersonic slit nozzle discharge, along with $C_6H_2^+$.[38]

Ball et al. obtained spectra of HC_7H and HC_9H in the gas phase with astrophysical applications[39] as well as of the linear carbon chains $HC_{11}H$, and $HC_{13}H$.[40] O-H stretching of jet-cooled methanol clusters were investigated[41] as well as methanol trimer[42] and 2-butanol.[43] Work on ethylene[44] shows the first Doppler-free nonlinear absorption of this very important chemical compound. Another study was also performed on the same species.[45] CRD was also used for ethyl and methyl peroxy radicals.[46]

The spectrum of photochemically produced NaH was measured at 382 nm by CRDS combined with degenerate four-wave mixing for spectroscopic studies, temperature determination, and measurement of relative dipole transition moments[47,48]. Predissociation of sulfur dimer S_2 state has also been investigated.[49] The spectrum of FCO radical was recorded around 30000 cm^{-1}.[50] Jet-cooled disulfur monoxide (S_2O) was investigated in the 29500-33000 cm^{-1} range.[51] Lithium dimer was generated and measured in a heated pipe oven.[52] It was also investigated in a laser-produced plume.[53] Kinetic observations on the CF_3O_2 radical have been reported using CRDS to monitor its concentration.[54]

Four reactive organic molecules of astrophysical interest have been identified in a supersonic discharge by CRDS.[55] The H_2O spectrum was recorded in the infrared[56] and in the context of isotope $^{18}O/^{16}O$ ratio measurements.[57] High-resolution Fourier Transform infrared and cw-diode laser cavity ringdown spectroscopy were performed on methane around 7510 cm^{-1} in a slit jet expansion and at room temperature.[58] A spectroscopic study of 1,3 butadiene around 20000 cm^{-1} has been reported.[59] OIO radical, important for the study of the ozone-depleting potential of iodine, was studied by Ashworth *et al*.[60] A demonstration of formaldehyde monitoring in ambient air was presented.[61] Alkyl peroxy radical kinetics were measured in the near infrared by CRDS .[62] Measurements of a UV-photolyzed naphthalene gas mixture around 650 nm were published.[63] Trace detection of NO_2 was carried out with a diode laser at 410 nm with sub-ppb detection.[64] Spectroscopic and kinetic investigations of methylene amidogen were reported in the 278-288 nm wavelength region.[65] Lastly, methyl iodide clusters $(CH_3I)_n$ in a supersonic jet were photolyzed, and the iodine molecule I_2 product was detected by CRDS.[66]

2.3.2 Cavity Ringdown Spectroscopy with Plasmas

A challenging issue is to use CRDS to make direct quantitative measurements on a plasma where direct sampling is not efficient because of continuing change in the sampled gas composition. Many techniques have been used, ranging from standard emission, which is only capable of detecting species in high electronic states, to LIF, which works well even in an intense background emission environment. Furthermore, most of these techniques yield relative measurements, except for Intracavity Laser Absorption and Cavity Ringdown Spectroscopy, which yield absolute absorbance. It is interesting that CRDS is now cited in reviews of Laser Aided Plasma Diagnostics.[67] It has

the potential of determining “the concentration of very dilute gas-phase species in hostile environments”. The applications of a continuous-wave laser source to the technique are discussed in a publication.[68] Another discussion can be found in ref. 69 with the description of broadband absorption spectroscopy, intra-cavity laser absorption spectroscopy (ICLAS) and cavity ringdown spectroscopy, and their recent application to measure the density of SiH_2 radicals and dust particles formed in a silane discharge plasma is reported in reference.[70] In the previous work, performance of CRDS and ICLAS are compared. Grangeon et al.[71,72] evalutated cavity ringdown with a large-area rf-plasma reactor for determination of negative ion densities in pure oxygen and hydrogen plasmas as well as observing nano-particles trapped in silane plasmas. Furthermore they reported an observed long-term plasma-induced drift of the ring-down decay time. A broadband absorption was due to the dust particles formed in the plasma volume.

CRDS has also been applied to the absolute detection of low-density species in a H_2-plasma to detect H^- ions as well as atomic hydrogen.[73]

Absolute concentrations of reactive species in etching plasmas have been measured by ultraviolet CRDS.[74] Measurements of CF and CF_2 radicals were made with standard absorption and compared to CRDS spectra; absorbance coefficients were on the order of 10^{-2} to 10^{-4}. Another work[75] obtained spectra for CF, CF_2, AlF and SiF_2 radicals in capacitively-coupled radio-frequency plasmas in fluorocarbon gases. This technique could be used for real-time (1 second time scale) absolute concentration measurements during wafer processing.

CH was detected in an expanding argon/acetylene plasma[76] and rotational spectra measurements were used to determine the total CH ground state density as a function of the current through the plasma arc and as a function of the injected acetylene flow.

Conclusions were drawn relative to the growth mechanism of hydrogenated amorphous carbon films.

Linnartz et al.[77] have measured the electronic spectrum of linear C_4 in a supersonic planar plasma around 379 nm. They determined molecular constants. Capability of CRDS to measure small broadband absorption in the deep UV (215 nm) in the hostile environment of a deposition plasma was demonstrated by Boogaarts et al.[78] They achieved measurements of the silyl radical (SiH_3) in a remote Ar-H_2-SiH_4 plasma during hydrogenated amorphous silicon (Si:H) film growth.

Hemerik et al.[79] reviewed their efforts to build a mid-infrared cavity ringdown spectrometer; their main goal was to perform spatially and temporally resolved radical density measurements on a real depositing silane discharge. Another paper[80] underlines the importance of probing gas mixture in chemical vapor deposition; this can be achieved with pulsed and continuous cavity ringdown spectroscopy. A CRDS study[81] at Eindhoven University determined absolute gas number densities of various SiH_4 radicals crucial for film growth deposition.

Non-exponential behavior study has been carried out by a Universite Joseph Fourier group[82] in a neon + argon discharge. The wavelength of interest was about 653 nm at which neon lines were observed. The saturation resulted from either depletion of the lower state or overpopulation of the upper state.

N_2^+ spectra measurements around 390 nm were obtained in pulsed and DC atmospheric pressure discharges.[83] Such discharges are of interest for applications such as biological decontamination and electromagnetic shielding. N_2^+ is the dominant charged species and thus enables one of the most direct measurements of electron density. An Abel inversion method is used to recover the radial profile of electron number density.

Authors insist on the fact that CRDS could also be used in the case of a pulsed discharge, with the necessity to fit different temporal windows within the ringdown. This approach is investigated as a mean of measuring the peak electron concentration. N_2^+ ions were also studied in a pulsed nitrogen plasma[84] and in an atmospheric pressure nitrogen glow discharge[85] by temporally resolved cavity ringdown spectroscopy. In the latter work, radial profiles have been measured and compared with a collisional-radiative model. Time-resolved cavity ringdown spectroscopy was also used to study the gas phase and surface loss rates of Si and SiH_3 plasma radicals.[86] A first work on N_2^+ in a hollow cathode source was carried out by Kotterer et al.[87] for rotational temperature measurements. Macko et al.[88] measured densities of N_2 molecules in a glow discharge at 227 nm.

Kessels et al.[89] from Eindhoven University of Technology, Netherlands, used cavity ringdown absorption spectroscopy for the detection of Si and SiH in a remote Ar-H_2-SiH_4 plasma used for high rate deposition of device-quality hydrogenated amorphous silicon (a-Si:H). The rotational temperature of SiH is deduced to be 1500K and among the results, it is demonstrated that both Si and SiH have minor contribution to a-Si:H film growth. The same group also reported cavity ringdown detection of SiH_3 in a remote SiH_4 plasma.[90] They achieved spatially resolved SiH_3 measurements at 217 nm. More specifically, the axial and radial densities in the cylindrical deposition reactor were compared with simulations by a two-dimensional axi-symmetric fluid dynamics model, showing fairly good agreement with the experimental results. Using CRDS and threshold ionization mass spectrometry, the authors of this work[91] proved from measurements in a remote Ar-H_2-SiH_4 plasma that film growth is by far dominated by SiH_3.

Furthermore, CRDS in conjunction with 1-D Laser-Induced Fluorescence has been used to measure OH density in an intense pulsed electrical DC discharge source for

OH molecular beams.[92] Cavity ringdown yielded absolute line-of-sight OH density while the off-axis distribution of the radical has been determined by 1-dimensional LIF spectroscopy.

Schwabedissen et al.[93] made absolute density measurements by CRDS of eroded silicon in the gas phase from the interaction of a target with a rf plasma. As a target, either a quartz plate or a silicon wafer was used. The Si density was determined from the decrease of the CRD decay time around 252 nm and typical Si densities were on the order of only 10^7-10^8 cm^{-3}. They also found that Si distribution in the plasma extended over a wider area than the dimensions of the target and that the densities increased with rf power and argon pressure. CRDS has also been used for a SiO_2 film-deposition setup.[94] Cavity ringdown spectroscopy has been used simultaneously with time-of-flight mass spectroscopy on jet-cooled copper silicides[95], silver silicides[96] and gold silicides[97]. Measurements were done in the visible and UV and the molecules were generated in a pulsed UV laser vaporization plasma reactor.

Rotational constants were determined by Vaizert et al.[98] when measuring spectra of HC_6N with CRDS in a supersonic planar plasma. An electronic transition of NC_5N was also studied by the same group[99] as well as NC_6N^+ in a supersonic plasma with determination of molecular parameters. More recently, Cias et al.[100] measured spectra of penta-acetylene cation ($HC_{10}H^+$) and isotopic species ($HC_{10}D^+$, $DC_{10}D^+$), permitting determination of ground and excited state spectroscopic constants. Similarly, the di-acetylene cation (HC_4H^+) was also studied[101] as well as tetra-acetylene cation[102] (HC_8H^+) electronic origin band and its deuterated derivative (DC_8D^+).

Infrared high-resolution continuous-wave diode laser cavity ringdown spectroscopy has also been carried out in a microwave discharge.[103] The apparatus was

built to study the recombination of H_3^+ with electrons. The technique had enough sensitivity ($<2.0x10^{-8}cm^{-1}$) to accomplish the desired task.

Kinetics of C-H radicals produced by a pulsed electric discharge in methane have been studied with CRDS and changes of concentration were determined on a microsecond time scale.[104] Another work on CH radicals[105] displayed spectra of different dissociation products, such as C, C_2, CH and C_2H, in a remote Ar/C_2H_2 plasma. C_2 was also studied in a microwave plasma[106] and in a dc arc jet[107] where concentrations and temperatures of C_2 and CH were measured.

Quandt et al.[108] reported the first application of cavity ringdown spectroscopy to the quantitative detection of negative ions H^- into a magnetic multiple source.

Finally, CRDS has also been coupled to a 27-MHz low-power argon inductively coupled plasma at atmospheric pressure for atomic absorption measurements[109]. A lead aqueous solution was introduced into a modified torch design to enhance the ICP conditions for atomic absorption measurements at 283.3 nm. This work will be described in detail elsewhere in this dissertation.

2.3.3 Cavity Ringdown Spectroscopy with Flames

Cavity ringdown spectroscopy has been successfully applied to several species in flames, such as CN, NO, OH and H_2O, to name a few. We will give a brief description of these experiments with their results. It is important to note that the growing number of investigations of flames and plasmas tend to prove that CRDS is an excellent candidate for combustion monitoring and plasma diagnostics.

Measurements of OH in flame were reported in several works. Its spectrum was recorded around 298 nm in a flame with coherent cavity ringdown spectroscopy[110].

Another work[111] recorded spectra of OH radicals absorption profiles and rotational temperature profiles in a flame. Experimental results were in agreement with computer-simulated results. CRDS was also used in a low-pressure (30-Torr) methane/air flame to measure OH radicals.[112] Non-equilibrium concentration of vibrationally excited OH radical from water vapor in an atmospheric flame was determined.[113] Strong deviation from Maxwell-Boltzmann equilibrium for populations of excited vibrational levels of OH radicals were observed in the pre-flame zone. Finally, Mercier et al.[114] compared OH concentration profiles recorded with CRDS and those recorded with laser-induced fluorescence and laser-absorption. They noticed that index of refraction gradients could be responsible for important off-resonance losses that perturbed CRDS measurements. Line-of-sight CRDS measurements performed along the axis of gradients were found to be very accurate.

Mercier et al.[115] also measured absolute CH concentration in an atmospheric diffusion flame by cavity ringdown spectroscopy. They reported these measurements around 315 nm for the first time and a comparison with laser-induced fluorescence measurements was made. CH concentration measurements were also made in a low pressure methane/air flame[116] and in a diamond-depositing oxyacetylene flame.[117] CRDS was also applied in conjunction with planar laser-induced fluorescence to map quantitatively the spatial distribution of CH_2O and CH in a methane/air low pressure flame.[118,119]

Near-infrared cavity ringdown spectra of water vapor were recorded in an atmospheric flame.[120] The rotational temperature and concentration of water vapor as a function of distance from the plane burner surface were mapped out. CRDS of HCO in a

low pressure flame was reported by Scherer et al.[121] The same authors made measurements of methyl radical in a methane/air flame by infrared CRDS.[122,123] Direct measurements of CH_2, an important combustion intermediate in flames, was possible with good spatial resolution with CRDS.[124]

Mercier et al.[125] recorded CN radical spectra in a low-pressure methane/air flame by CRDS around 387 nm. Profiles of the cyano (CN) radical were measured during oxyacetylene flame deposition of diamond.[126] The results were in agreement with a previous laser-induced fluorescence work.

Furthermore, a technique called cavity enhanced magneto-optic rotation spectroscopy[127] has been used in an air-acetylene flame for Ga atoms at the resonance line of 417.2 nm.

Pillier et al.[128] measured NO mole fraction formed in the burnt gases of a low-pressure premixed flame. C_2 absolute concentrations were measured in an oxyacetylene flame.[129]

Last but not least, a numerical analysis of beam propagation in a pulsed cavity ringdown spectroscopy has been carried out by Spuler and Linne[130], especially when a flame is present inside a ringdown cavity.

2.3.4 Trace Gas Detection

Inherent to its great sensitivity, CRDS can be used for trace gas detection. Very low-level detection of species is very difficult to achieve, especially in dusty or hostile environments. Detection can be carried out directly in plasmas, flames or low-pressure environments. Usually the measurement apparatus is remotely located and is placed after equipment like filters, dryers or any device cleaning the gas flow. The first commercial

instrument based on infrared cavity ringdown was developed by Tiger Optics. It is a fast and reliable instrument made for detection of trace water vapor and ultra-trace gas impurities, such as NH_3, CO, HCl, HF and CH_4 with sub parts-per-billion concentrations[131,132]. Similarly, Stry et al.[133] reported a portable spectrometer based on a continuous-wave variant of cavity ringdown technique called the leak-out method. This portable laser system achieves sensitivity of 10^{-8} cm^{-1}, corresponding, for example, to part per billion ethane detection limits.

One of the first trace gas detection experiments was carried out by Jongma et al.[134] in the near U.V., while measuring absolute concentration of the OH radical present in trace amounts in heated air due to thermal dissociation of water. They also achieved detection of NH_3 at the 10 ppb level in calibrated gas flows and of background Hg concentration with detection limit of below 1 part per trillion in air.

Romanini et al.[135] demonstrated noise equivalent absorption of 10^{-9} cm^{-1} with a CW laser CRDS setup. A section of the HCCH overtone transitions was recorded near 570 nm and compared to existing photo-acoustic data. Elsewhere, CW-CRDS has been used to detect acetylene[136] with $3x10^{-9}$ cm^{-1} sensitivity. This new setup blocks the incident CW laser by quickly scanning the cavity length off-resonance with a piezoelectric transducer.

Use of compact and reliable light sources has made realization of small, portable instruments within reach. A fiber optic system has been designed for ICLAS and CRDS in conjunction with a micro-optic gas cell.[137]

Detection of trace amounts of moisture (water vapor) has been demonstrated[138] within the frame of two different experiments: one realized with a continuous CO_2 laser working around 1000 cm^{-1} and the other realized in the vicinity of 10000 cm^{-1}.

Gopalsami et al.[139] investigated the applicability of CRDS in the millimeter wave region. The apparatus consisted of a tunable Fabry-Perot cavity, a fast PIN diode switch that turned off the continuous wave phase-locked source, and a photodetector to record the ringdown. Czyzewski et al.[140] used CRD-spectrography, a variant of CRDS in which the signal is simultaneously analyzed within a broad spectral range to monitor trace gases, like nitrogen oxides, in the atmosphere. This technique was also used for the study of the CH radical produced by a pulsed electric discharge in methane. Measurements of NO_3 and N_2O_5 have been done with a sensitivity of 0.25 parts-per-trillion.[141] The paper overviews the pit falls of trace gas detection specific to their case.

Trace explosives vapor detection has been achieved by Todd et al.[142] Their instrument, a mid-infrared CRDS tool, was tested on several vapor phase common explosives that were readily detected at part per billion concentrations. Such a device has evident military and safety applications.

CHAPTER III

EXPERIMENTAL

3.1 Inductively Coupled Plasma

The inductively coupled plasma (ICP) is a tiny, low temperature (<10000 K) weakly ionized (<2%), near thermal discharge. Energy is transferred to the plasma by inductive coupling from the induction coil to charged particles, primarily electrons, in the induction region. The plasma gas retains much of the energy gained in the induction region and extends several centimeters above the load coil. ICPs are widely used in the analytical community. A modified, lower outer-flow ICP torch shown in Figure 3.1-1 with wider inner channel was designed for the particular needs of cavity ringdown spectroscopy. The torch is composed of three concentric channels. Samples are injected in the central channel. During "normal" operation, a nebulizer converts sample solution into a fine mist of aerosol droplets prior to injection in the central channel. The mist is mixed with hot gases in the thoroidal induction zone. Above the load coil (3-turn load coil used for argon in our experiments), the plasma has a conic shape because of air entrainment. As sample progresses up through the aerosol channel, it undergoes the processes of desolvation, vaporization, excitation, ionization, emission and recombination more or less in sequence from bottom to top.

The ICP has already been used in the past in conjunction with a variety of spectroscopic techniques such as the highly sensitive mass spectroscopy which requires high vacuum, optical emission spectroscopy and laser-induced fluorescence to name a few. Extensive fundamental studies on the ICP have been performed such as plasma temperature measurements, electron number densities, atom and ion number density, spectral linewidths, collision rates and even time-resolved, cross-correlated, ion-atom emission intensities.

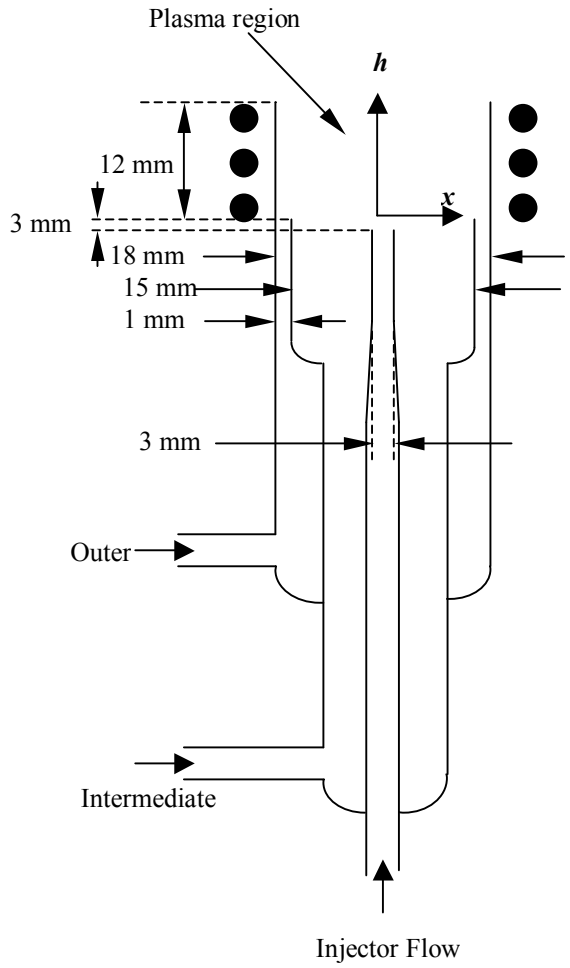

Figure 3.1-1. Diagram of the modified ICP torch used throughout this work

3.2 Lasers

The lasers used in this experiment are described in this section as well as optical instruments used to produce laser radiation in the desired frequency range. The use of pulsed lasers is particularly suited for cavity ringdown since it is based on recording of a transient signal. The laser components are all commercially available and came with a manual. The details of the aligning procedures are skipped here, but we will outline the general method for using the experimental system. These high precision lasers require knowledge of laser theory to align them.

The frequency-doubled or frequency-mixed output from a Nd:YAG laser is used to pump a dye laser. The Nd:YAG is the Powerlite Precision 8020 model of Continuum (Continuum, Santa Clara, California). It delivers a fundamental beam of wavelength 1064 nm and of duration 6-8 nanoseconds with nominal maximum pulse energy of 1200 mJ, which can be frequency doubled to obtain a 532 nm beam of nominal maximum pulse energy 550 mJ. This beam is then used as a pump beam for the dye laser. The dye laser is made of a set of optics specially coated for the pump beam, with lenses and coated mirrors whose purpose is to focus the beam into the dye cells. A second set of optics comprised roughly of a cavity (one or two gratings to disperse the light and a coated mirror on the output), and a collimating telescope for the dye laser beam. The pump beam enters the two dye cells at an angle that can be modified so as to optimize for minimum spontaneous emission and to maximize for laser power. The first dye cell serves as the oscillator as well as pre-amplifier, the second one amplifies the laser beam.

The frequency doubler holds a crystal whose incidence angle can be modified relative to the laser beam which comes out of the dye laser. The crystal is a beta-barium borate (BBO) type I. A fraction of the beam is filtered by color filters and is sent onto

two photodiodes so that auto-tracking of the frequency-doubled laser power is possible by monitoring for maximum output. This enables varying the laser wavelength (by changing the grating angle controlled by software provided by the manufacturer) without having to re-adjust manually the frequency doubler since the Auto-Tracker (Inrad, Northvale, New Jersey) will tune the crystal angle so as to maximize the output of frequency-doubled light. A four prism-filter that selects the shortest wavelength is then used to filter out the fundamental beam and let the frequency doubled laser beam through. A block diagram (Figure 3.2-1) displays all the components of the laser beam generation.

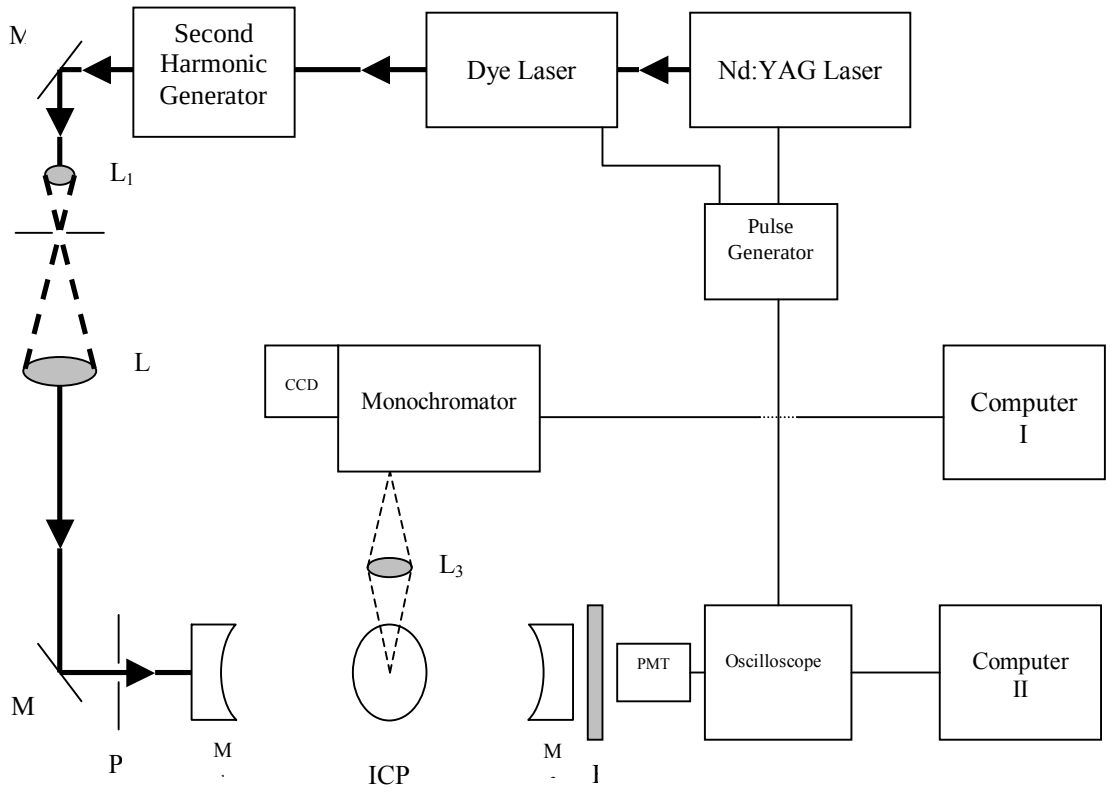

Figure 3.2-1. Schematic of experimental apparatus. M, M_1 and M_2 are mirrors; L_1, L_2 and L_3 are lenses; P is pinhole aperture; F is a narrow band filter; CCD is a charge-coupled device detector; PMT is a photomultiplier tube; ICP is an inductively coupled plasma.

3.3 Cavity Design

We first consider a cavity formed by two identical plano-concave mirrors with radii of curvature equal to R, separated by a distance L. The input mirror acts as a diverging lens of focal length that is equal to:

$$f = -\frac{R}{n-1} \tag{3.1}$$

where n is the index-of-refraction of the substrate.

The apparent wavefront curvature at the mirror will be computed according to the lens law, that is:

$$R' = \frac{R \cdot f}{f - R} \tag{3.2}$$

The radius of curvature of the wavefront is equal to the radius of the mirrors at the mirror surface so as to produce a self-replicating beam. One can show that for wavelength , the beam waist $_0$ at the center of the mirrors is given by the following equation:

$$\omega_0^2 = \frac{\lambda \cdot L}{2\pi}\sqrt{2\frac{R}{L} - 1} \tag{3.3}$$

From the propagation relationship for the beam at a distance L/2 from the center of the mirror, one obtains for the beam waist at the mirrors the following relationship:

$$\omega_1 = \frac{\lambda}{\pi\omega_0}\sqrt{\frac{R \cdot L}{2}} \tag{3.4}$$

In the case where the mirrors have different radii (say R_1 and R_2), one obtains two equations by noting that at the mirrors, the wavefront has same curvature as the mirrors, that is:

$$R_1 = -d \cdot \left[1 + \left(\frac{z_R}{d} \right)^2 \right] \tag{3.5}$$

and

$$R_2 = (L-d) \cdot \left[1 + \left(\frac{z_R}{L-d} \right)^2 \right] \tag{3.6}$$

where Z_R is the Rayleigh distance, d the distance of the beam waist location with the input mirror located on the left. One then needs to express Z_R as a function of d, replace it in the other expression and solve for d. This gives:

$$\omega_0^2 = \frac{L\lambda}{\pi} \sqrt{\frac{g_1 \cdot g_2 \cdot (1 - g_1 \cdot g_2)}{(g_1 + g_2 - 2g_1 \cdot g_2)^2}} \tag{3.7}$$

(where the g parameters have already been defined in Chapter II), with spot sizes w_1 and w_2 at the ends of the resonator:

$$w_1^2 = \frac{L\lambda}{\pi} \sqrt{\frac{g_2}{g_1 \cdot (1 - g_1 \cdot g_2)}} \tag{3.8}$$

and

$$w_2^2 = \frac{L\lambda}{\pi} \sqrt{\frac{g_1}{g_2 \cdot (1 - g_1 \cdot g_2)}} \tag{3.9}$$

Lastly, the locations of the two mirrors relatively to the gaussian beam waist are given by:

$$z_1 = \frac{g_2 (1 - g_1)}{g_1 + g_2 - 2g_1 \cdot g_2} L \tag{3.10}$$

and

$$z_2 = \frac{g_1(1-g_2)}{g_1+g_2-2g_1 \cdot g_2} L \tag{3.11}$$

The image of the cavity mode given by the plano-concave lens formed by the substrate of mirror M_1 has its waist located a distance z' from the input mirror (mirror M_1) where:

$$z' = \frac{R'}{1+\left(\frac{\lambda \cdot R'}{\pi \cdot \omega_1^2}\right)^2} \tag{3.12}$$

and a beam waist equal to:

$$\omega' = \frac{\lambda}{\pi \omega_1} \sqrt{R' \cdot z'} \tag{3.13}$$

The two last parameters completely specify the gaussian input beam. It is then necessary to mode-match the incident laser beam to this calculated beam, both in waist position as well as waist value. This is done with a set of two lenses and a pinhole located at the focal point of the input lens. Knowing the position of the telescope, one can back-propagate the beam waist at the telescope output for example. The size of the pinhole is taken as two to three times the waist value that the beam should have at the location of the pinhole.

3.4 Experimental Apparatus

3.4.1 Laser System: Dyes Used

The Radiant Narrow Scan grazing incidence dye laser was used with double gratings when possible; when used with simple grating (and mirror), the linewidth measured by a Fabry-Perot with a free spectral range of 0.25 cm^{-1} was about 0.08 cm^{-1} at 590 nm and about 0.04 cm^{-1} when used with double gratings. All desired wavelengths

necessitated frequency doubling and dyes with long lifetimes (in terms of Watt-hours) were used, namely Rhodhamine 6G for 286.57 nm, LDS 750 for 358.49 nm and LDS 820 for 409.01 nm.

3.4.2 Cavity

Mode-matching was accomplished with a 5x beam expander, a 100-mm focal objective lens, and a 25-μm pinhole located at the focal point. These produced a nearly gaussian laser pulse with accurate parameters. The cavity length used was about 77 cm, and was always formed by two plano-concave super mirrors (Los Gatos Research, Los Gatos, CA) with radii of curvature of 6 meters. The reflectivities of the super mirrors at selected wavelengths were, respectively, 99.7% at 253.7, 99.85% at 286 nm, 99.9% at 369 nm, and 99.99% at 409 nm. For each absorption line, a 10-nm narrow band pass filter (CVI Laser, Albuquerque, NM) was used in front of the Hamamatsu photo-multiplier tube (model R106UH). Typically, 10 to 100 ringdown curves were averaged with no renormalization before being fitted.

3.4.3 Laser-Induced Fluorescence Setup

The laser-induced fluorescence (LIF) signal was collected perpendicular to the laser beam by a lens on the entrance slit (120-μm wide) of the monochromator (0.5-m monochromator, ARC, Spectra Pro 500) and detected by a PMT at the exit slit (also set to 120 μm).

3.5 Standards Preparation

3.5.1 Mercury and Lead Standard Preparation

All solutions were prepared by diluting a stock solution of concentration 1000 parts-per-million, corresponding to 1g/L. Standards were from Absolute Standard Inc., Hamden, CT. Solutions were made by diluting microliter quantities of the initial stock solution into 250 mL of acidified, purified water. Successive dilutions were used to reach the desired concentration. The acidified water solutions, also called blanks, were obtained by diluting 2% nitric acid. The solutions are then pumped into an ultrasonic nebulizer (CETAC U-5000AT+) that converted these dissolved metals into dry aerosol particles with an efficiency of 15%.

3.5.2 Uranium Standard Preparation

^{235}U standard solutions were made by diluting solid phase uranium. More precisely, one gram of uranium, consisting of highly purified U_3O_8 was dissolved into 10 mL of 65% nitric acid solution. The isotopic richness of the solution in ^{235}U was about 97.663% in mass. Standard solutions of 1000 µg/mL of ^{238}U were prepared from 1g/L solutions purchased from Absolute Standard Inc, Hamden, CT. These two solutions were mixed with different ratios so as to obtain different isotopic ratios. All standard solutions were carefully diluted in 2% nitric acid de-ionized blank water solutions. The solutions were then flown through an ultrasonic nebulizer (CETAC U-5000AT+), which had 7-10% conversion efficiency for uranium.

3.6 Mercury System Experimental Setup

The apparatus for this experiment is similar to those of other ICP-CRDS experiments. The data acquisition system was a GPIB interface connected to a Tektronix 400MHz scope (model TDS 460A). The ringdown waveforms of 100 laser shots were averaged 'as is'. Because of the low transfer speed between the oscilloscope and the computer, the system was only able to provide a new ringdown waveform every ten seconds. The same acquisition system was used for the ICP-CRDS lead and uranium measurements. The other elements of the experimental apparatus are described below.

For atomic absorption spectroscopy (AAS) measurements, either a quartz T-shaped cell with open ends (5-mm diameter holes drilled on each end) or a π-shaped cell with closed ends could be used for the detection cell. In both cases, the length of the cell was 18 cm and its inner diameter was 1 cm. For CRDS measurements, only the open-end cell could be used in order to avoid optical losses from the quartz windows.

A 0.5-meter echelle spectrometer with a charge-coupled device (CCD) detector (Spectrum One CCD-200, Jobin Yvon-Spex) was used as the atomic absorption spectroscopy (AAS) detection system to detect light from a mercury lamp placed on the opposite side of the cell.

The reducing vessel used for batch mode was a 1.08-L plastic bottle. The mercury vapor was then carried by argon to the quartz cell through Teflon tubes of 0.75-mm diameter. For continuous mode reduction, a Gilson Minipuls peristaltic pump (Gilson Inc., Middleton, WI) was used to inject the mercury and reagent solution at a rate of 1.3 mL/min. The two solutions were mixed at a "Y" joint and passed through a 3-meter long Teflon tube (0.75-mm outer diameter) where mercury reduction and extraction took place before reaching a spray chamber of a pneumatic nebulizer. Finally, before entering the

quartz absorption cell, argon carrier gas at a flow rate of 0.4 L/min flowed through a gas-liquid separator that retained moisture which otherwise caused an unwanted ringdown time drop because of scattering.

Solutions of 5% $SnCl_2$ in 10% HCl were made by dissolving 3.0 g of $SnCl_2 \cdot 2H_2O$ (J.T.Baker, Phillipsburg, NJ) in 50 mL of 10% HCl for use in batch mode experiments. Solid tin beads were added to stabilize the reagent. For continuous mode generation, $NaBH_4$ solution was made by dissolving solid $NaBH_4$ (Sigma Chemical Co., St. Louis, MO) in water and by adding NaOH to stabilize the reagent. Mercury standard solution is made by diluting standard stock solution (1 mg/mL, High Purity Standards, Charleston, SC) with 10% HCl solution.

3.6.1 Batch Reduction System

The batch system consisted of a 1.08-L plastic container in which a volume of 1.0 mL mercury standard solution was mixed with 0.2 mL of the $SnCl_2$ reduction agent. Two drops of solution were mixed in only after the container was properly sealed so as to ensure no loss of analyte. Then, argon gas is flowed into the container at a rate of 1.0 L/min, carrying the Hg atoms into the quartz cell.

3.6.2 Continuous Reduction System Setup

The mercury standard solution and the 0.5% $NaBH_4$ reagent solution were mixed in a Y joint tube prior to traveling through a long Teflon tube in which, in addition to mercury reduction, H_2 gas was formed. The H_2 helped carry the Hg into the separation chamber where argon gas would push it toward the absorption cell at a flow rate of 0.4 L/min.

CHAPTER IV

MERCURY ANALYTICAL RESULTS

4.1 Introduction

Mercury is a poisonous element that can cause kidney injury, nervous system disorders and even death.[143] The importance of mercury in the environment has been increasingly known for the last decades and input of heavy metals into the atmosphere has been carefully tracked.[144] Elemental mercury can be released from ore deposits, volcanic and seismic activities as well as man-made activity such as from industrial activities and inadequately managed waste facilities. Water-soluble forms of mercury, e.g. CH_3HgCl, can be even more toxic. Already in the early 1950s, after an accident in Japan that caused the death of more than 100 people, nations around the world prohibited dumping of methyl mercury in water streams. Occurring with background concentrations of ng/m^3 in the atmosphere, elemental mercury has to be detected with very sensitive systems. The basic technique relies on pre-concentration (accumulation) of the element on a gold foil, followed by a sudden release by a heating procedure, and detection by atomic absorption or laser-induced fluorescence. Because of the relative stability of the elemental form, chemical reduction as well as thermal atomization routes are possible. In most cases, when high sensitivity is required, pre-concentration is used. A good review of

analytical sensitivity of various techniques for mercury detection can be found in a review paper by Clevenger *et al*.[143]

4.2 Using CRDS for Hg detection

The feasibility of using CRDS for Hg detection was accidentally demonstrated by a background CRDS wavelength scan that was obtained when an unsealed mercury waste container was placed near an open-air 56-cm long ringdown cavity (Figure 4.2-1). The resulting CRDS spectrum clearly showed the mercury absorption line at 253.65 nm, demonstrating a below 1 part-per-trillion (ppt) limit of detection under atmospheric conditions. Reports of elemental Hg detection by CRDS have until recently been relatively scarce. Jongma *et al*. mentioned the potential for trace gas analysis.[145] S. Tao *et al.* realized a cold vapor Hg detector using CRDS and performed some Hg spectroscopic interference studies with H_2S.[146] The present work demonstrates that CRDS is not only a very sensitive technique for analytical atomic measurements, but also is a very versatile technique usable with various atomization sources for analytical purposes. The atomizers successfully coupled with CRDS were: cold vapor generation, electrothermal atomizer, and inductively coupled plasma. The limits of detection (LOD) will be given for the various atomizers.

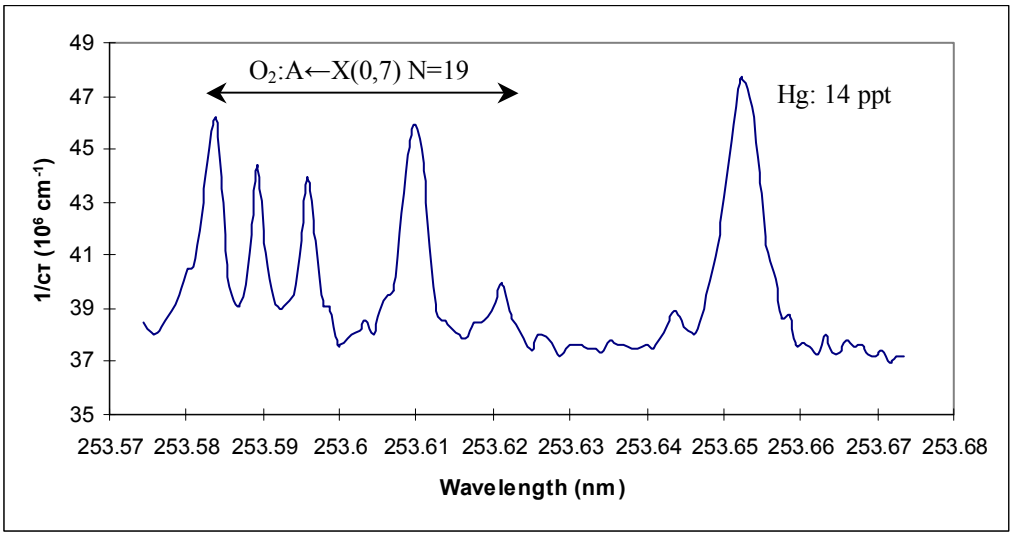

Figure 4.2-1. Hg background scan acquired with CRDS in our lab.

4.3 Hg Cold Vapor Generation

4.3.1 Introduction

In chemical reduction, molecular forms of mercury are reduced to mercury atoms that are then carried into an absorption cell by flowing inert gas through a reaction vessel. In standard atomic absorption spectroscopy (AAS), high sensitivity is achieved by pre-concentration that is usually accomplished by a reduction/trap concentration/release-by heating procedure. Once trapped Hg atoms are released, an absorption transient signal will follow. Usually this process occurs by flowing neutral gas containing organic and inorganic forms of mercury through gold, sand or beads which have to be changed after several uses and which are heated to around 800°C. CRDS is a method that is orders of magnitude more sensitive than AAS. No sample pre-concentration was used in this work, enabling batch as well as an on-line, continuous detection system described in the experimental chapter. In this work, AAS was used as a way to evaluate the increased sensitivity offered by CRDS.

4.3.2 Batch Reduction System

Figure 4.3-1 shows an example of the recorded CRDS profile obtained for an injected Hg mass of 2 ng. The absorption signal can then be quantified by dividing the maximum absorbance value by the time profile (called peak height) or the integrated signal (called peak area). Both signal peak height and peak area (integrated over 23 data points) displayed a linear behavior (Figure 4.3-2) with the injected Hg mass. The measured LOD were 0.12 ng with peak height and 0.027 ng for peak area. Assuming that 100% of the mercury is atomized, this corresponds to sampling a gas Hg concentration of 25 ng/m^3 in the reaction vessel. Because of dilution in the carrier gas and loss from the open windows, the actual gas concentration is lower. The same procedure for standard AAS was also repeated. The LOD for AAS using peak height was found to be 9 ng with end windows. When using an open-ends cell with AAS, the detection limits were noticeably reduced so that a direct comparison with CRDS experiment was not possible.

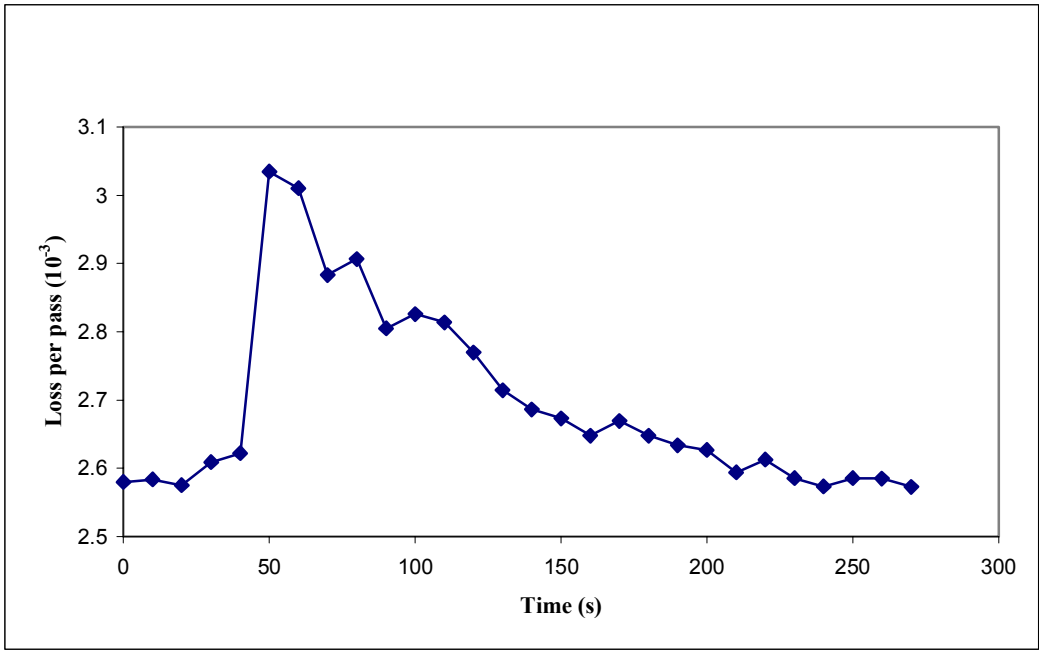

Figure 4.3-1. Batch CRDS signal for 2ng of Hg.

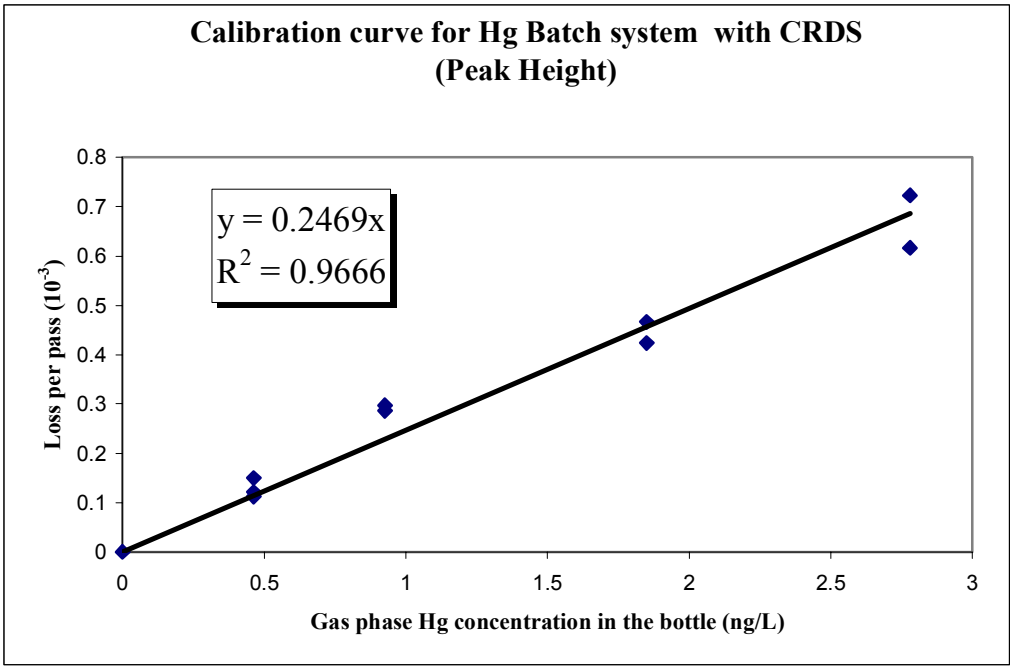

Figure 4.3-2. Batch system calibration – peak height.

4.3.3 Continuous Reduction System

Figure 4.3-3 gives the absorption profile obtained for the calibration of continuous mode mercury vapor generation. The baseline stability was found to be worse than in the batch process (around 2% for the former). This excess noise was attributed to the production of H_2 bubbles following the decomposition of $NaBH_4$ by the standard acidic solution. In such conditions, the detection limit for Hg was found to be 0.12 ppb.

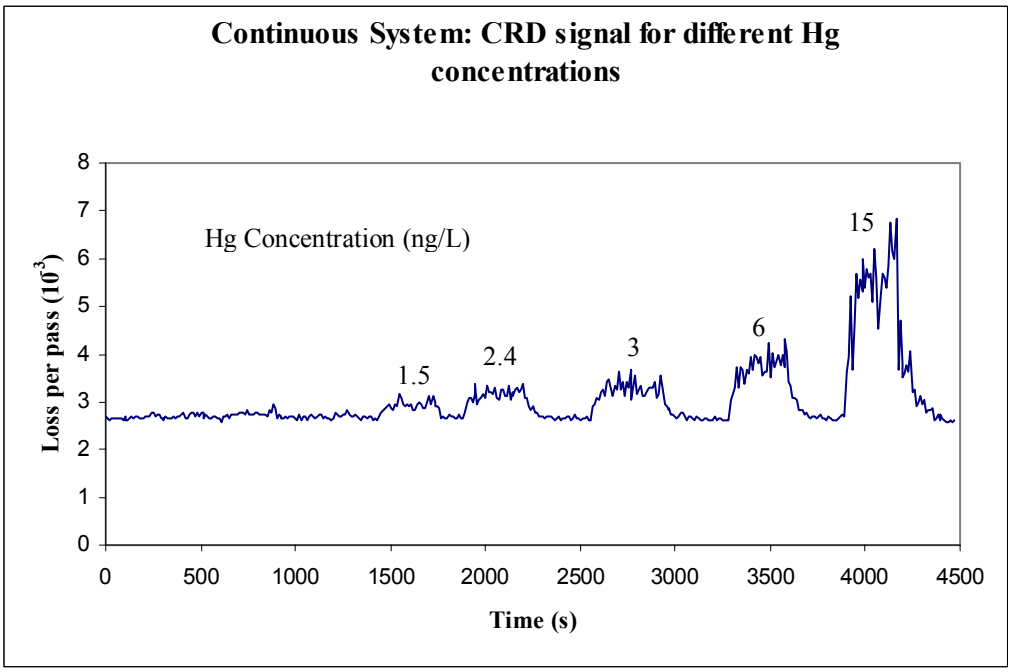

Figure 4.3-3. Continuous System calibration data.

4.3.4 Comparison with Expected Results

The parameters for the experiment were: 0.18-m absorption sample length *l*, a ringdown 1-σ variation $\Delta\tau_0$ of approximately 0.4% for peak height measurement, a ringdown time for the L=55 cm cavity of 700 ns, and Hg absorption cross section of $3.3\text{x}10^{-18}$ m^2 for atmospheric temperature and pressure[147]. The 3-σ limit of detection *DL* is defined as:

$$DL = \frac{\alpha}{\sigma_{ij} l} \tag{4.1}$$

where α is the minimum detectable absorbance defined as:

$$\alpha = \frac{L}{c}\left(\frac{1}{\tau_0 - 3\Delta\tau_0} - \frac{1}{\tau_0}\right) \tag{4.2}$$

where L is the distance between the mirrors, c is the speed of light and τ_0 is the measured CRDS decay time. This gives an expected LOD of 18 ng/m^3. For batch mode, we found a detection limit of 0.12 ng. This corresponds to a 110 ng/m^3 gas concentration in the reaction vessel, which is predicted to be larger than the actual gas phase concentration in the quartz cell. Peak area yields a detection limit of 0.027 ng, because of a better stability (0.1%). This corresponds to a 25 ng/m^3 gas phase concentration in the reaction vessel. For standard AAS, measurements performed by Dr. Shinquan Tao at DIAL gave the following results: 9 ng LOD (830 ng/m^3 gas concentration) in the case of a closed absorption cell and a limit of 0.12 ppb for the continuous system. In the case of the continuous system, the AAS and CRDS limits of detection are the same. For the AAS measurements, only the π-shaped closed cell was used because of significant loss in sensitivity while using the open-end cell. The similarity in CRDS and AAS limits of detection can be explained by the decrease in sensitivity due to air mixing in the open-end cell and by baseline CRDS fluctuations (about 1.7%), probably due to scatter by residual water droplets in the carrier gas.

Given that this was a preliminary experiment, the results obtained are in good agreement with the expected theoretical sensitivities. The CRDS setup could be improved by including the mirrors within the absorption cell, thus preventing any loss of analyte and protecting the cavity mirrors by a buffer gas. Such a system, which necessitates no pre-concentration, could have important applications such as on-line monitoring for mercury in a stack emission.

4.4 Electrothermal Atomization

4.4.1 Introduction

A commonly used atomization source in analytical spectroscopy is the graphite furnace or electrothermal atomizer. Atomization by heating is realized by passing electric current through a graphite cylinder into the center of which sample has been deposited. In commercially available analytical instruments, it is usually coupled with AAS to provide an extremely sensitive instrument for atomic spectroscopy. Extremely good results have been obtained also when coupled with laser fluorescence spectroscopy. W. Resto *et al.* [148] used two-step laser-excited fluorescence with an electrothermal atomizer for detecting mercury. By using palladium which avoids loss of analyte during the drying step, their absolute mass detection limits were around 90 fg. This is a laboratory instrument that only requires small quantities of sample (tens of microliters) and as such is still a centerpiece in an analytical lab. This very preliminary work with mercury was done mainly to estimate how CRDS would perform in such an environment. As a measure of comparison, the LODs will be compared with numbers of merit given by manufacturers of commercially available instruments.

4.4.2 Principle

A liquid or solid sample containing the element to be analyzed is deposited into a hollow cylindrical graphite tube which is connected to two electrodes. A strong electrical current is then flowed through the electrodes, which results in a rapid heating of the tube. The thermal energy generated causes dissociation of any molecular form, resulting in atomization of the selected element of interest. By controlling the current, it is possible to

control the temperature. Normally, a graphite furnace cycle will be composed of the following steps:

1) Drying: The temperature is slowly increased to approximately 100-200ºC for about 30 seconds to make sure that all moisture is evaporated.
2) Ashing
3) Atomization: The temperature depends on the element to be analyzed (1200ºC-2300ºC). For a transversely heated graphite tube, this step lasts less than five seconds.
4) Clean-up: The temperature is raised to its maximum value which depends on the element for a brief period of time in order to vaporize any residue and clean the graphite tube for the next cycle.

The graphite tube is enclosed by a casing filled with chemically neutral argon buffer gas in order to avoid oxidation of the graphite by atmospheric oxygen and to avoid reaction of the element with any atmospheric molecule. A jet of argon with a controllable flow rate is flowed around the graphite tube. During the atomization step, the argon flow is stopped so as to prevent any loss of analyte. To enable optical analysis, two 1-inch diameter quartz windows are mounted in the housing of the graphite tube. These windows were replaced with aluminum disks pierced with a 5-mm diameter hole so as to let the laser beam pass; this prevents optical losses from the quartz windows (which would be far greater than the losses of our ringdown mirrors). This modification increases air infiltration and might have an impact on sensitivity.

4.4.3 Experimental Procedure

Aqueous mercury standard solutions were obtained by successively diluting a stock solution of 1000 µg/mL (High Purity Standards, Charleston, SC) in a 2% nitric acid high-

purity blank solution. A small volume of the solution (5-20 µl) was then manually injected into the graphite tube through a small hole with a high-precision pipette (Eppendorf, NY). The graphite furnace (model GF 110, transversely heated, Aurora Instruments, Vancouver, Canada) controlled by a computer interface, was set with the following program:

1) Drying for 30 seconds at 120ºC
2) Atomization for three seconds at temperatures ranging from 1000ºC to1600ºC
3) Clean-up of five seconds at 1850ºC

Because of mercury's high volatility, the ashing step was skipped so as to avoid any loss of analyte. In order to record the rapid transient absorption signal, it was necessary to make a drastic change to our acquisition system. A fast 14-bit analog-to-digital conversion card (Compuscope 14200, Gage Applied Technologies Inc., Lachine, Canada) was used to record ringdown curves during the atomization step. Two seconds of data were saved each time, which corresponds to 40 ringdowns with a 20-Hz laser. The ringdown times and the corresponding absorbances were extracted off-line so as to obtain absorption signal versus time. Such a profile is shown in Figure 4.4-1 for 20 pg of Hg. A trigger from the graphite furnace provided timing for data acquisition. The signal was TTL (3-5V) on pins 24 and 25 (ground) of the DP25 RF interface (described in the manufacturer manual), situated at the back of the GF110 power supply (Aurora Instruments, Canada). When the atomization occurred, the signal was 'low'. The signal was logically NANDed to the laser trigger with a simple homemade electronic circuit. The output was used to trigger the acquisition card. The first 0.5 seconds after the atomization started were discarded.

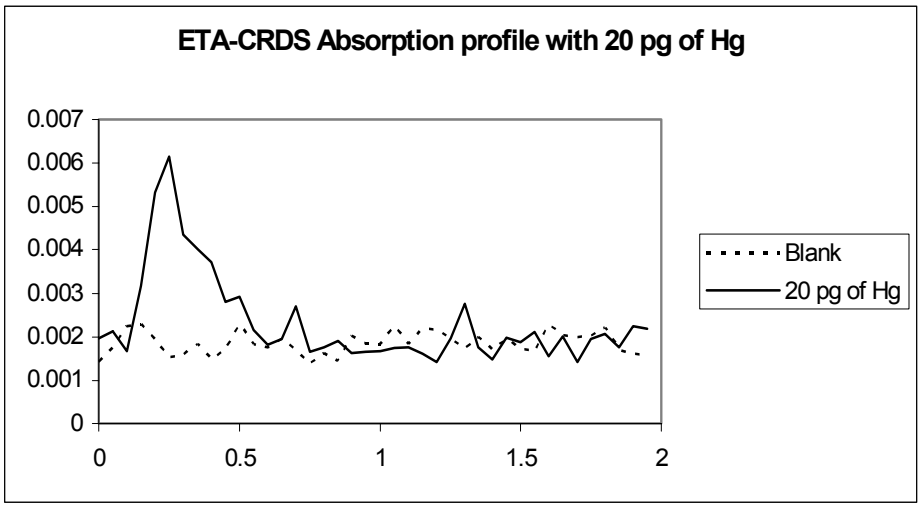

Figure 4.4-1. Hg 20 pg absorption signal in graphite furnace.

4.4.4 Results

The atomization temperature was found to give maximum absorption signal for a value of 1100ºC. In this experiment, because of the relative low laser repetition rate compared with the duration of the signal (less than 2 seconds), the absorption peak during the first half second (10 data points) was integrated rather than using maximum peak absorption which displayed much greater fluctuations (see Figure 4.4-2). The last 10 points of the signal were summed and subtracted from the integral of the absorption peak to correct for background. For blank solutions, the ringdown time was around 1 μs for a 65-cm long cavity with a shot-to-shot stability of around 10% during atomization. A higher laser repetition rate would offer the possibility to smooth the signal (by adjacent averaging for example), giving a better peak-height baseline stability. With our current system, the minimum detectable absorbance 3σ limit is 1.78×10^{-3} (per pass) for peak height, which based on peak height stability and 20 pg absorbance peak value of 4.0×10^{-3} above the blank absorption signal, places the detection limit at around 9 pg. Using peak

area, the signal for 20 pg is equal to 2.5 times the 3σ limit, which gives a detection limit of around 8 pg. Although we did not add any palladium which avoids analyte loss during the drying procedure, we were able to achieve a limit of detection almost one order of magnitude better than the figures of merit given by the manufacturer of commercial AAS graphite furnace systems (Perkin Elmer Corporation, MA).

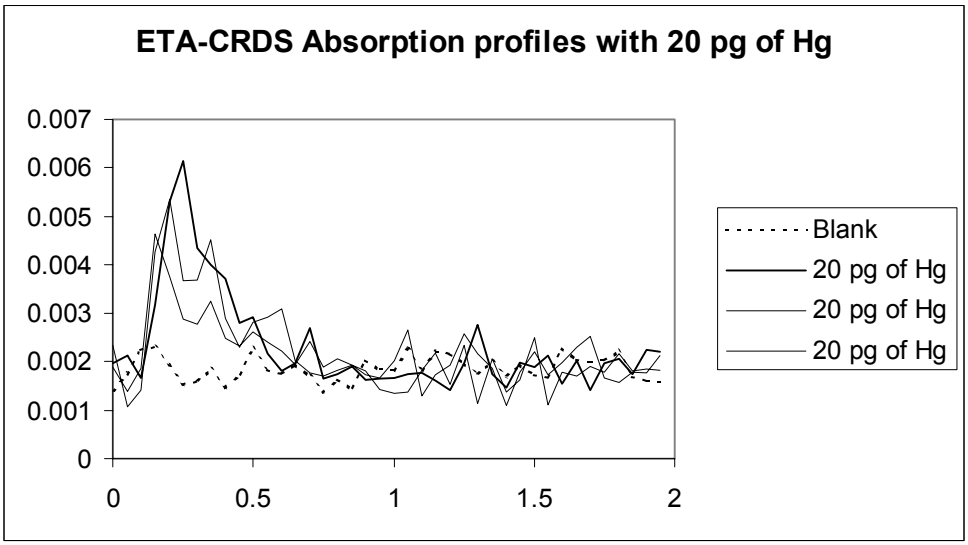

Figure 4.4-2. Illustration of GF profile reproducibility for 20pg of Hg. This graph shows repeated measured absorption profiles with same experimental conditions for 20 pg of mercury compared with one blank absorption trace.

4.5 Argon Inductively Coupled Plasma

4.5.1 Hg with ICP-LIF

The laser induced fluorescence (LIF) experimental procedure was similar to work done by Human *et al.*[149,150] The LIF signal was observed at 90° and the excitation wavelength was the same as the emission wavelength (253.7 nm).

4.5.1.1 Experimental Setup

The LIF signal was collected by a 1-inch diameter, 10-cm focal length lens and imaged in a 2-f configuration onto the entrance slit of a 1.5-m monochromator (Jobin-Yvon THR 1500) entry slit. The laser beam was collimated with a home-made telescope. For analytical LOD measurements, the position of the second lens of the telescope was set so as to obtain the maximum LIF signal intensity. For plasma diagnostic measurements, the laser beam was focused on the central channel of the ICP so as to have best spatial resolution. The emission intensity was measured with a photomultiplier (from Hamamatsu, model R106UH) whose output voltage was recorded on a Tektronix 400 MHz digital oscilloscope (model TDS 460A). The LIF signal was then sent to a computer through a GPIB interface and integrated by home-made software written by Ping Rey Jang of DIAL. The software integrated the signal recorded by the oscilloscope on a range delimited by the two vertical cursors of the oscilloscope. Since the fluorescence wavelength and the excitation wavelength were the same, it was important to reject all light scatter. An iris placed at the focal plane of the collecting lens helped reduce the scattered light. To be sure to discard all scattered light, the integration window was delayed for a period of about 20 ns (the laser pulsewidth was about 8 ns). The PMT output voltage was integrated for a duration of 200 ns.

To ensure correct alignment of the collecting optics, a planar obstacle making a 45° angle with the laser beam was placed at the position of the central channel and the scattered light was centered on the collecting lens and on the spectrometer entrance slit.

In all LIF experiments, it is important to saturate the excited state population in order to avoid baseline fluctuations proportional to laser power fluctuations. In our case, shot-to-shot laser power variations were about 20-30%.

4.5.1.2 ICP Conditions

The ICP parameters were optimized so as to maximize the ground state population of Hg atoms. The ICP parameters were varied within the following ranges:

- RF power : 200-500 W
- Main flow : 15.0 L/min (not varied)
- Intermediate flow : 0.4 L/min (not varied)
- Injector flow : 0.7-2.0 L/min
- Observation height : 2.5-25 mm above load coil (ALC)

4.5.1.3 ICP Torches

For this work, torches with a narrower outer gas channel were used and thus require lower argon outer flow rates. These are more stable than the standard torches [151]. For plasma diagnostic measurements, we had a special torch made with a shorter outer shield so as to enable low height ALC measurements (see Chapter 3). For the CRDS measurements, we used a 3-mm diameter injector torch so as to increase the sample path-length (1.5-2 mm for standard torches). A 4-mm diameter injector torch was also tested, but was not used because the resulting plasma was too unstable and would frequently extinguish.

4.5.1.4 Results and Discussion

The LIF signal was composed of a sharp peak when the laser fired (light scatter) and then a decaying exponential curve. The lifetime of the excited state was measured to be around 70 ns. The Einstein A coefficient for this atomic Hg transition is 8.0×10^6 s^{-1},[152] which yields an excited state lifetime of 125 ns in vacuum. The actual lifetime of the excited state is shortened because some the excited atoms decay into the $6^3P_0^0$ state and mainly because collisions in the plasma cause non-radiative transitions. In this work, we observed variation of Hg LIF signal with several ICP parameters, namely ICP RF power, central channel (or injector) flow, and observation height. The graphs showing LIF integrated signal versus any of these parameters are shown in Figure 4.5-1. A wavelength scan of the atomic line is also shown in Figure 4.5-2. The scan shows a linewidth of about 6 pm that is to be compared with 3.8 pm for the collision-free transition.[153] This broadening comes from the linewidth of our laser (measured to be 0.1 cm^{-1} before frequency doubling). The curves showing the dependence of the LIF signal on ICP parameters were used to optimize the conditions so as to obtain the best sensitivity for Hg measurements. The calibration of LIF signal versus analyte concentration shows good linear behavior (Figure 4.5-3). Because of poor dye efficiency, the laser power fluctuations were around 20-30% so the stability of the LIF signal was less than desired. Note also that the Coumarin 500 dye used in this experiment had a short lifetime (a few hours with a 20-Hz repetition rate). With the LIF signal averaged on 100 shots, and given the baseline stability, this yielded a LIF detection limit of around 20 ppb.

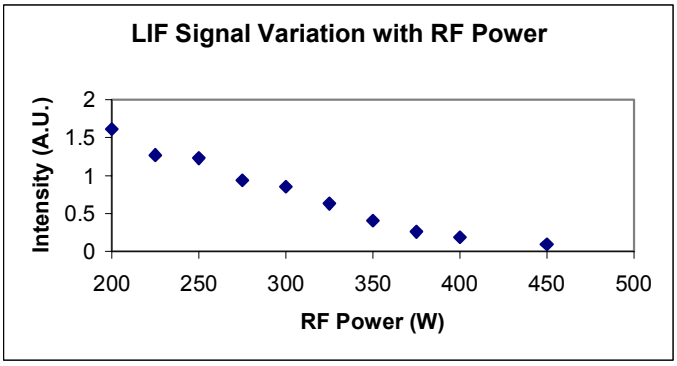

LIF signal variation for a Height of 2 mm above the load coil (ALC), for an injector flow rate of 0.9 L/min

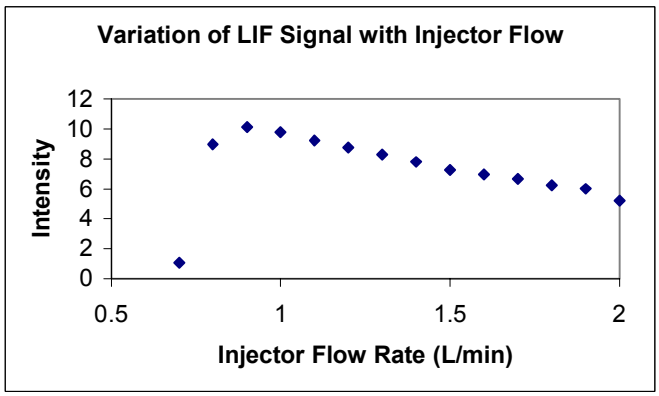

Variation of LIF signal with injector flow for 200W RF power and a height of 2 mm ALC

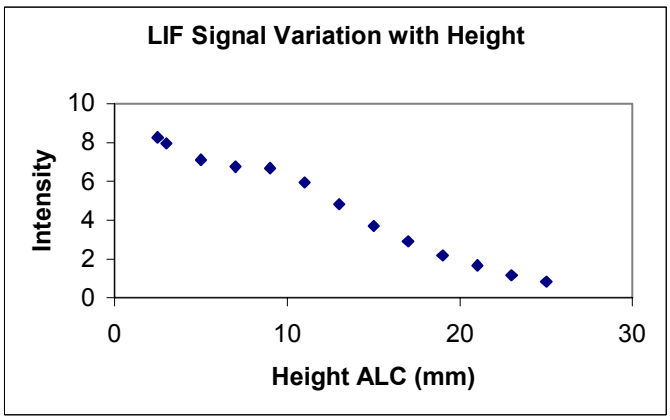

Variation of LIF signal with height for a RF power of 200W and an injector flow of 0.9 L/min

Figure 4.5-1. Variation of Hg LIF signal variation with ICP parameters

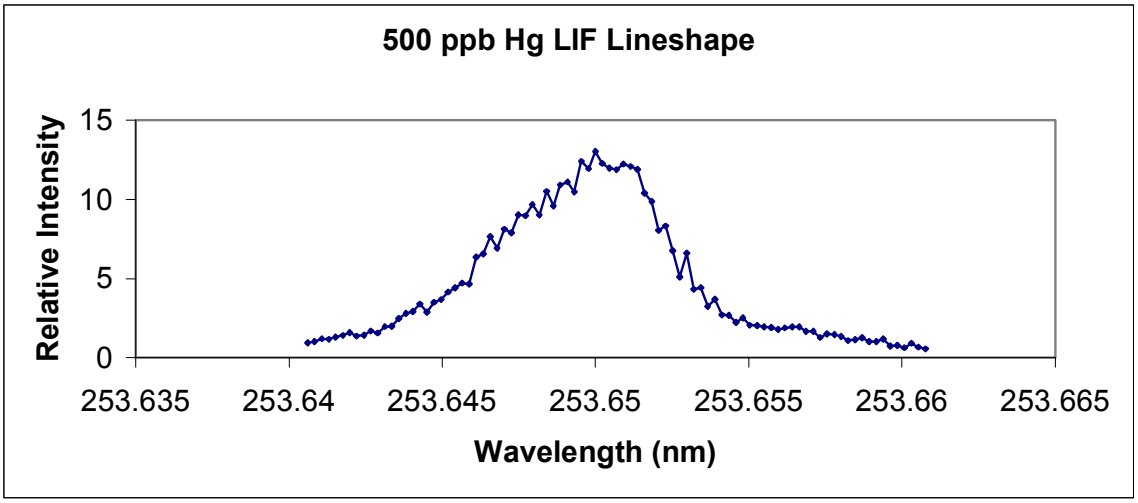

Figure 4.5-2. Mercury LIF wavelength scan.

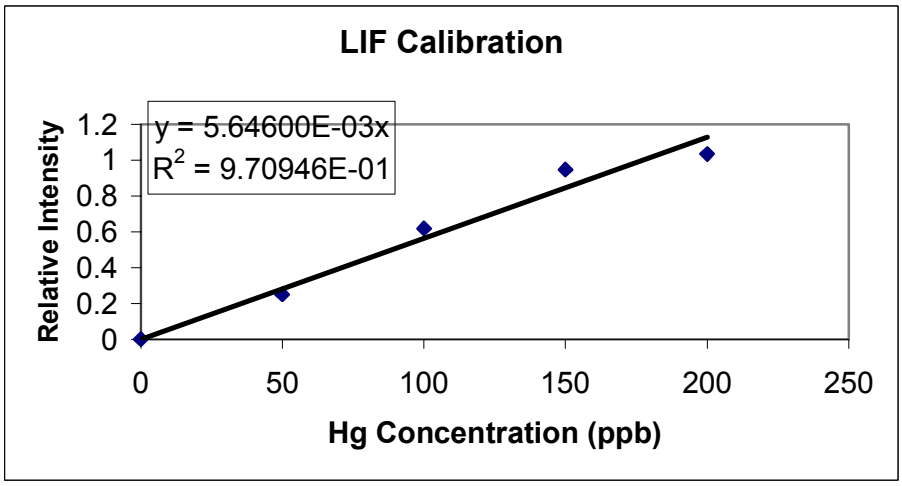

Figure 4.5-3. LIF calibration plot ICP operating conditions were optimized for RF power (200W), observation height (2 mm ALC) and injector flow rate (0.9 L/min).

4.5.2 Hg with ICP-CRDS

4.5.2.1 Introduction

CRDS has some advantages when compared with LIF. First of all, CRDS enables absolute measurements whereas LIF measurements are relative. Furthermore, since

CRDS is an absorption technique, it does not suffer from the drawbacks of LIF, mainly quenching of fluorescence and atomic level branching. For plasma diagnostic purposes, absolute absorption measurements and absence of quenching are a great advantage, especially for atomic density measurements. In addition to the analytical interest, we would like to assess the practical use of CRDS for probing plasmas. The issue of probing plasma temperature with CRDS will be discussed in another chapter.

4.5.2.2 Experiment

The main experimental apparatus for CRDS in ICP are the same as the one followed in previous work (see Chapter III).[154] The data acquisition system is the same as the one used for cold vapor Hg generation, as is the detection system and the optics. A careful re-alignment of the cavity is essential here with the plasma inside the cavity, since the presence of the ICP could induce beam steering. Whereas the plasma appears very stable to the eye, when the laser beam makes even a single pass through the plasma, noticeable deviations from its original direction as well as dispersion are noticeable. The effects of such deviations on the cavity optical modes and consequently on the stability of the ringdown time have not been fully quantified yet.

4.5.2.3 Results and Discussion

Regarding ICP parameter optimization for the absorption signal, the procedure followed was the same as for the LIF section: variation with ICP RF power, observation height and injector flow were studied (Figure 4.5-4). From these measurements, the optimal conditions could be found and analytical performance of the system could be deduced. The calibration is shown in Figure 4.5-5. A scan across the plasma shows the

line-of-sight integrated LIF distribution (see Figure 4.5-6) from which we can estimate a 3-mm absorption path-length.

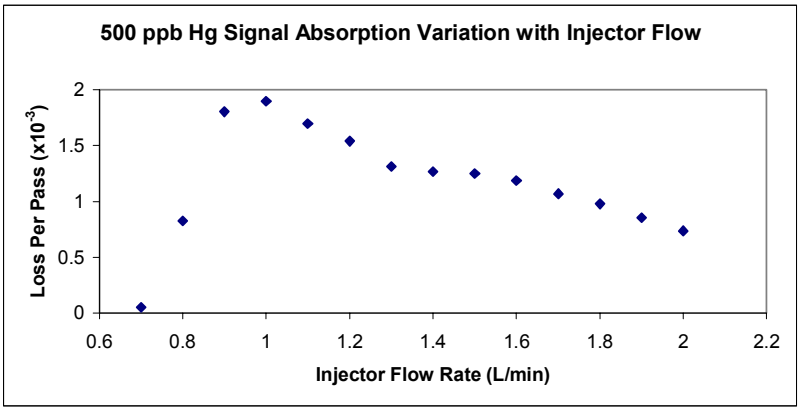

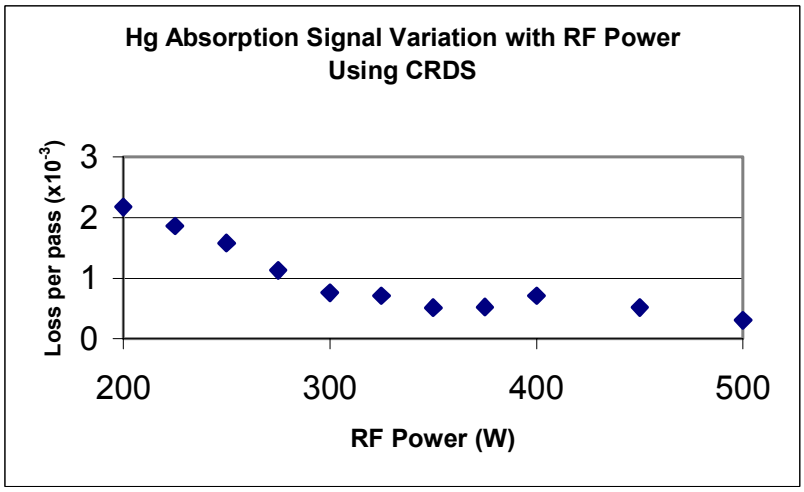

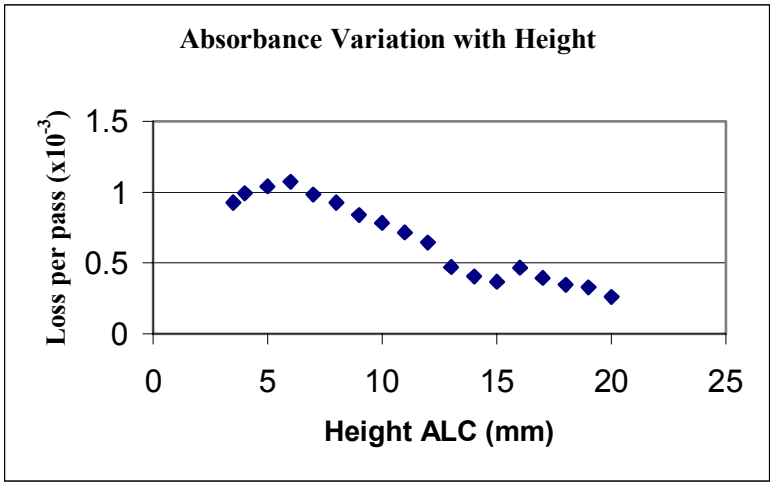

Figure 4.5-4. CRDS signal variation versus ICP parameters for a Hg concentration of 500 ppb, at a height of 5 mm ALC, with flows 15.0L/min for outer, 0.4L/min for intermediate, and 1.0 L/min for injector. In the graphs, the parameters were optimum for 1.0 L/min for the injector, 200W for the RF power and 5 mm height ALC when not specified.

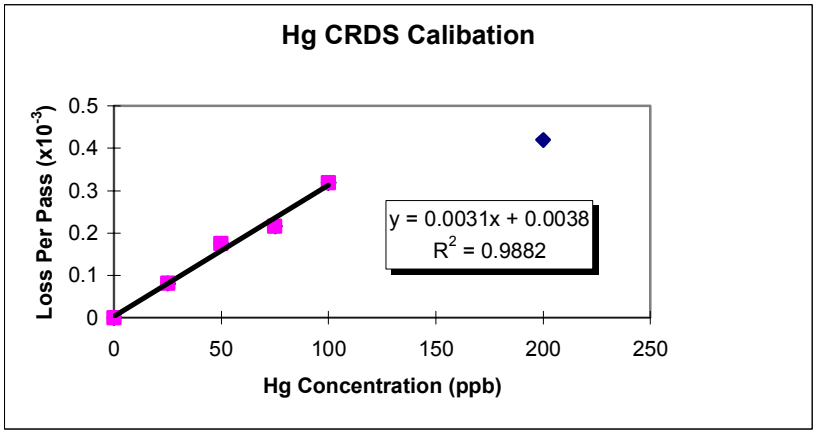

Figure 4.5-5. CRDS calibration curve obtained for optimized parameters listed above.

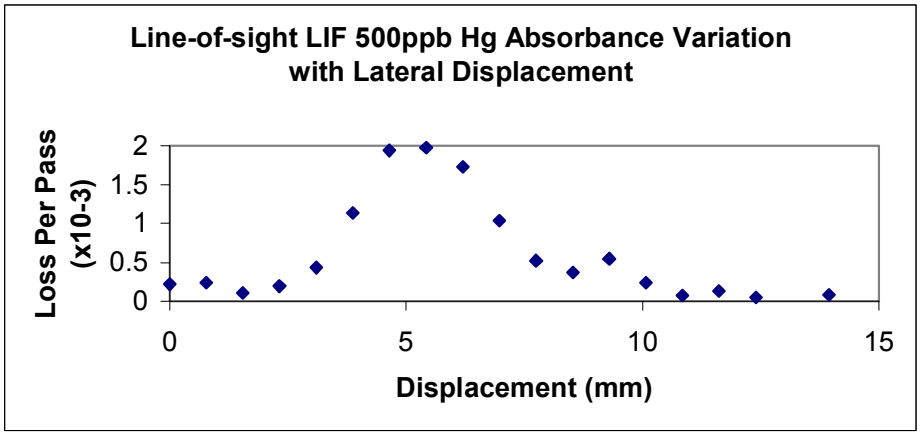

Figure 4.5-6. LIF scan across plasma. Optimized ICP parameters are the same as above.

4.5.2.4 Estimated Gaseous Detection Limit

The absorption cross section in case of a Lorentzian lineshape is:

$$\sigma_{ij} = \frac{g_j}{g_i}\frac{\lambda^4}{8\pi c}\frac{A_{ji}}{\Delta\lambda} \tag{4.3}$$

For the 253.7-nm transition of mercury, given an atomic linewidth of 3.8 pm, the cross section is equal to $3.5\text{x}10^{-18}$ m^2/atom. Assuming a 100% atomic ground state population, the gas phase detection limit is given by equation (4.1). In our case, with a cavity length of 55 cm and with an ICP RF power of 200 W, the ringdown time measured for blank solution was 0.8 μs and the relative ringdown time stability was about 1%. This gives an *apparent* mirror reflectivity of about 99.7% (decreased mirror reflectivity due to air scattering) and a minimum detectable absorbance α of $7\text{x}10^{-5}$ per pass, resulting in an estimated gaseous LOD of 2.2 ng/L for ground state Hg atoms. Assuming a mercury solution uptake rate of 2.5 mL/min, a nebulizer efficiency of 15%, an injector argon flow of 1 L/min, and a 50% ground-state Hg atom population, this should correspond to a detection limit of 12 ppb in aqueous solution.

4.5.2.5 Experimental Results and Comparison with LIF

The standard low-flow torch with a 1.5-mm diameter injector tube has a detection limit of 80 ppb while the specially designed torch with a 3-mm diameter injector tube has a detection limit of 20 ppb. This is, within a factor 2, in good agreement with the expected results derived in the previous section. It is also noteworthy that the experimental curves of absorbance variation with different ICP parameters display the same behavior as the variation of LIF signal with the same ICP parameters, that is:

- The lower the RF power, the higher the ground state population. This is in agreement with results from Kornblum and De Galan [155] where the ICP was used as an atom reservoir.
- The observation heights ALC have to be much lower than usually used. In this experiment, studies were made in the range 10-20 mm. With observation heights above 20 mm ALC, using CRDS seems difficult at this stage because the baseline fluctuations become too important.
- For the regions of the plasma explored and the parameters used, no significant influence on quenching rates in LIF was observed. This seems to indicate that the collision rate is high and did not significantly vary over the conditions studied.

4.5.2.6 Comparison of LIF and CRDS LODs

From this experiment, LIF detection limits were twice as low as CRDS LODs. However, it is worth noting that first of all the LIF baseline stability was about 9% and also that the LIF detection electronics could have been improved with faster electronics and a better optical setup. If we assume that LIF LODs could be improved by a factor of five, this would make LIF one order of magnitude more sensitive than CRDS. The main

limitation encountered for CRDS is the relatively poor reflectivity of the mirrors currently available at this wavelength. The CRDS mirrors we used for this experiment turned out to be about 99.8% reflective. Mirrors about 99.99% reflective would improve the LODs by a factor of 30 which would make CRDS definitely more sensitive than LIF and would also make the system compliant with EPA requirements.

4.5.3 Air Inductively Coupled Plasma

4.5.3.1 Introduction

One of the original motivations behind ICP-CRDS experiments was the improvement of an already existing air-ICP system developed by DIAL[156,157] for continuous metal monitoring. The system is based on emission spectroscopy and its great advantage is that it runs on air (which is present in off-gas systems) rather than argon. On such a system, emission gives enough sensitivity for most of the elements, except for mercury for which the EPA requires higher sensitivity; thus the idea of using CRDS with an air-ICP to attain better detection limits for mercury. The apparatus used for air ICP is basically the same as for argon (same low-flow torch), the main difference being that it needs to run on a higher RF power (greater than 2.6 kW).

4.5.3.2 Air ICP Absorption Background

An air ICP absorption spectral scan was obtained on a 3 nm wavelength range (Figure 4.5-7) showing a molecular spectrum of O_2 [158] that we assigned to the Herzberg $A^3\Sigma_u^+ \leftarrow X^3\Sigma_g^-$ transition and that could serve as a basis to future work. No spectral

interference was observed with mercury. A narrower scan also shows what appears to be an unassigned rotational structure (Figure 4.5-8).

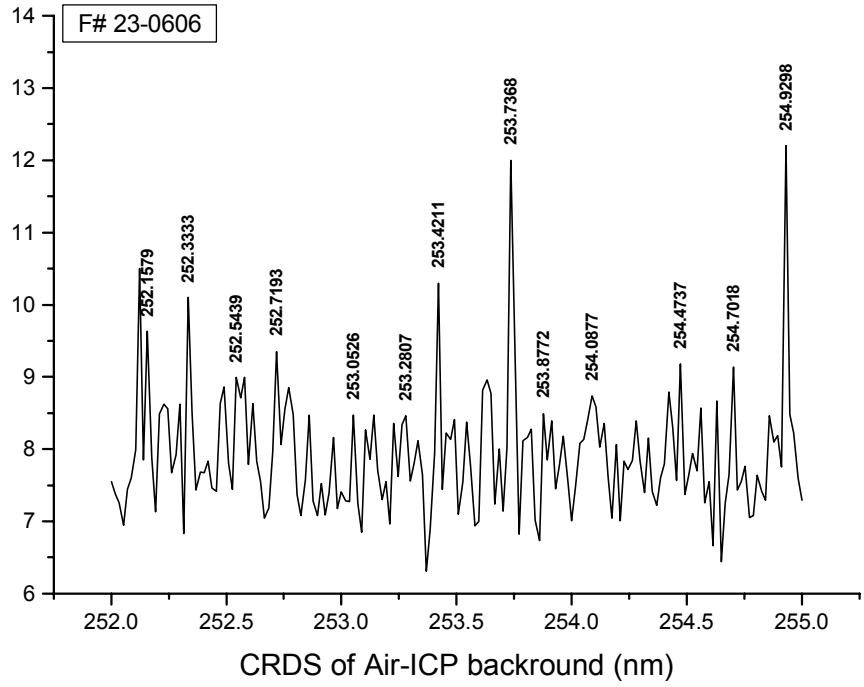

Figure 4.5-7. Air ICP 3 nm background scan.

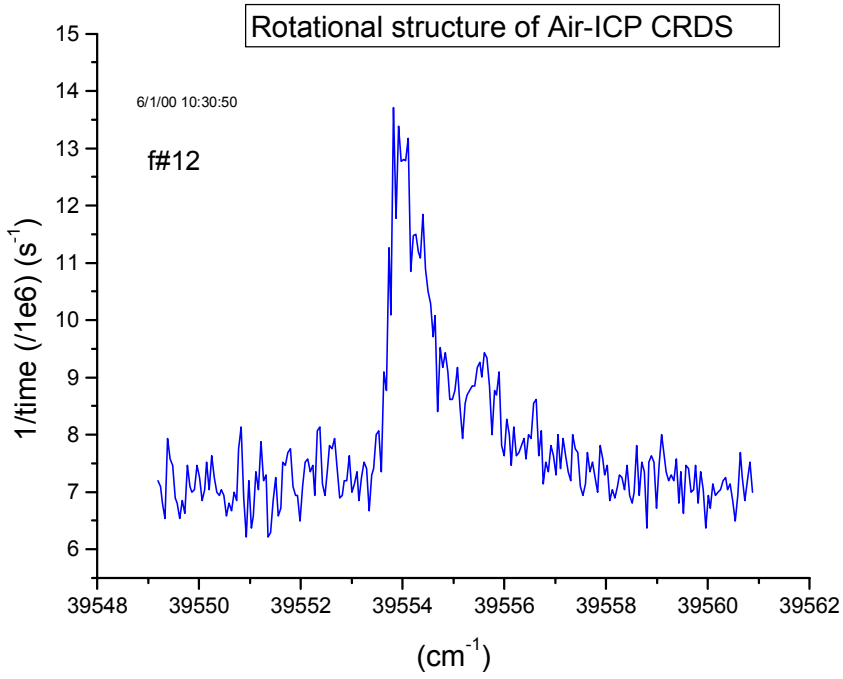

Figure 4.5-8. Rotational Structure in Air ICP.

4.5.3.3 Experimental Results : LODs

In our experiment, we only used the standard 'low-flow' torch with a 2-mm injector diameter. The RF power used for the measurements was 2.8 kW; air flows were: 26 L/min, 0.6 L/min and 1.4 L/min for main, intermediate, and central, respectively. Solution uptake rate was 2.0 mL/min. With an empty, open-air 55-cm length cavity, the ringdown time was around 550 ns. With the air ICP on, the ringdown baseline would drop to 135 ns. It is believed that such a high relative drop is due to a higher thermal gradient. Also, the stability went from 0.4% for the empty cavity (averaging 100 ringdowns) to 2-3% with the plasma on, revealing a slightly more unstable plasma than when argon is used. Because of the studies already made with the argon ICP and because the excitation temperature in an air ICP is generally higher than in argon, one should

expect a lower sensitivity in the air ICP. Also contributing to this is a shorter path-length, greater baseline fluctuations, and lower apparent mirror reflectivities because of greater optical losses introduced by the plasma. A linear calibration plot is shown in Figure 4.5-9. The 3σ detection limit extrapolated from this graph is around 3 ppm which yields a gas-phase concentration of 0.8 μg/L of total atomic mercury.

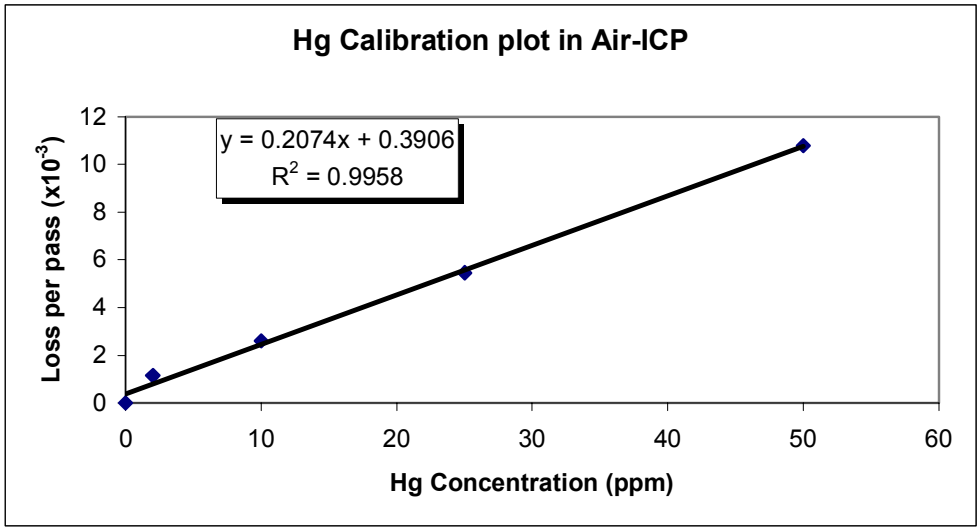

Figure 4.5-9. Hg Calibration in Air ICP.

4.5.3.4 Observation of Mercury Isotopic Abundance

By scanning the mercury absorption line with the smallest scan step (0.15 pm step in the UV), we observed several sub-peaks which were repeatable both in intensity and location from scan to scan. These spectral features were observable in the air ICP (see Figure 4.5-10) as well as in the argon ICP (see Figure 4.5-11).

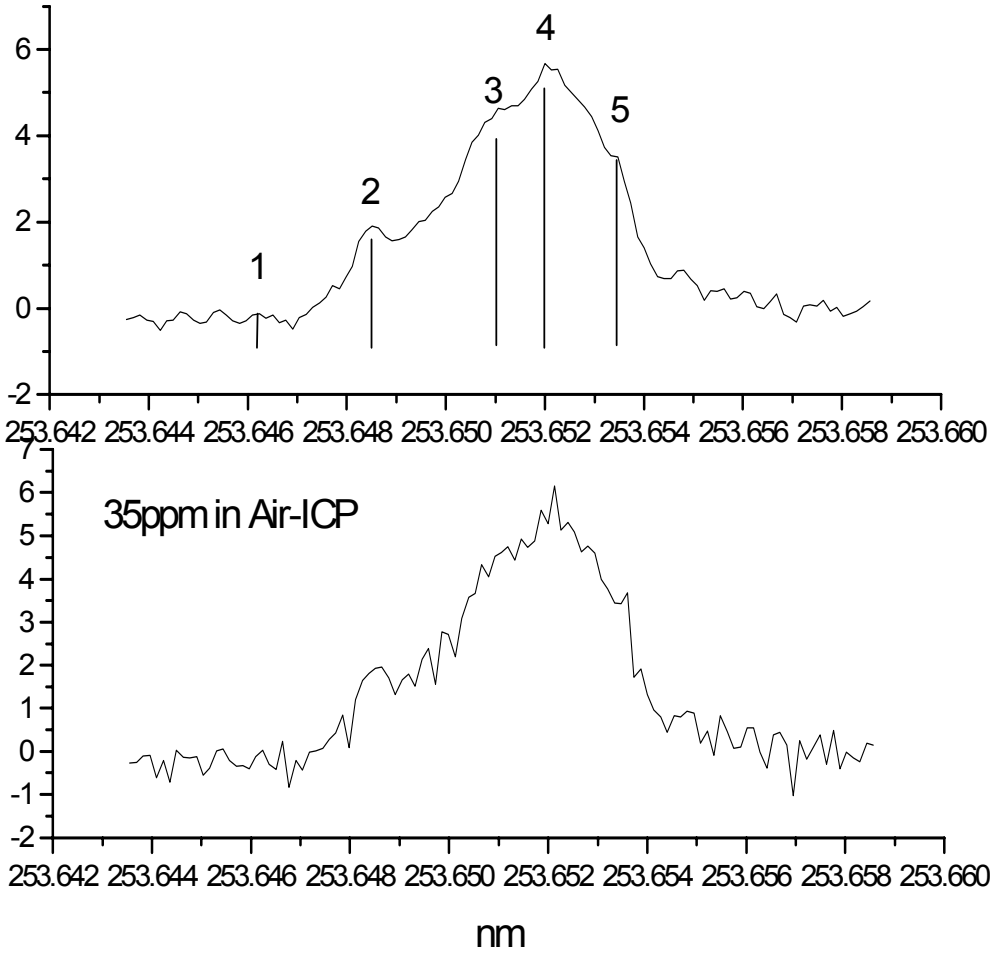

Figure 4.5-10. Hg Lineshape – Air ICP (2.8 kW, flows = 26 L/min, 0.6 L/min, 1.5 L/min)

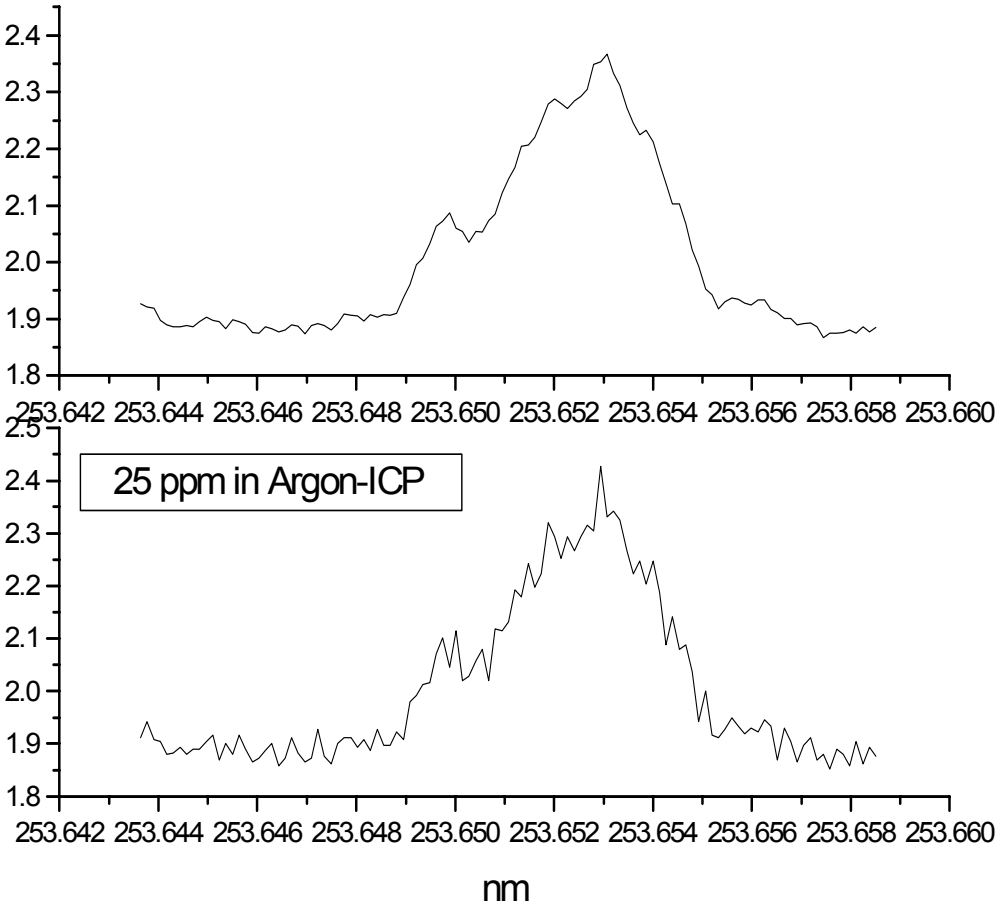

Figure 4.5-11. Hg Lineshape – Argon ICP (400 W, flows = 16 L/min, 0.2 L/min, 0.6 L/min).

The intensity ratio of these peaks matched with the theoretical isotopic abundance of mercury (see Figure 4.5-10 and Table 4.5-1, Figure 4.5-11 and Table 4.5-2), demonstrating the potential of CRDS-ICP use for isotopic analysis. Because of the linewidth of our laser and of the Lorentz and thermal broadening caused by the plasma, we were not able to resolve these peaks.

Table 4.5-1. Hg Isotopic Abundance – Theoretical and Experimental Comparison in Air ICP

Line #	Wavelength (nm)	Exp relative intensity	Exp ratio(%)	Theo relative intensity	Theo ratio(%)	Isotope assignments
1	253.6466					201c+199a
2	253.6498	2.51	13.9	14.4	16.6	198+201b
3	253.6517	5.15	28.5	23.1	26.7	200
4	253.6528	6.32	34.9	29.8	34.5	202
5	253.6535	4.11	22.7	19.1	22.1	204+201a+199b

Table 4.5-2. Hg Isotopic Abundance – Theoretical and Experimental Comparison in Ar ICP

Line #	Wavelength (nm)	Exp relative intensity	Exp ratio(%)	Theo relative intensity	Theo ratio(%)	Isotope assignments
1	253.6466					201c+199a
2	253.6498	0.092	16.1	14.4	16.6	198+201b
3	253.6517	0.157	27.5	23.1	26.7	200
4	253.6528	0.184	32.2	29.8	34.5	202
5	253.6535	0.138	24.1	19.1	22.1	204+201a+199b

4.6 Summary of Results and Future Considerations

We have demonstrated that CRDS could be used for mercury analytical measurements with either a graphite furnace, a cold-vapor mercury generation system and as well as with the ICP. For the ICP, we compared detection limits with a well-known, widely used technique which is laser-induced fluorescence. For the graphite furnace, we've obtained a ten-fold improvement compared with standard absorption-based commercial systems. Had we had a higher repetition rate laser, we could have integrated the signal and our figures of merit would have been much better. For the cold vapor generation, we could detect trace amounts of mercury close to the part-per trillion

expected gaseous sensitivity. The limit of detection for the ICP were of 20 parts per billion in acidic solution and about 4 ng/L in the gas phase in the argon ICP, which is comparable with the LIF limits of detection. It is undeniable that with improvements in the mirror reflectivity the ringdown technique would and will easily outperform LIF by several orders of magnitude, as well as standard ICP emission spectroscopy. With the improvement in diode laser spectroscopy, it is viable to imagine a small, compact, very sensitive measurement system that meets the EPA (Environment Protection Agency) requirements in sensitivity. The projected below-one part per billion would be sensitive enough to serve as an environmental continuous, real-time mercury monitor. We've also shown that the ringdown technique proved successful with the air inductively coupled plasma, even if its inherent high excitation temperature makes it a non-optimized ground-state mercury atom reservoir. From the fundamental point of view, we were able to observe rotational spectrum of molecular oxygen, enabling plasma local thermal equilibrium test measurements. Also, we were able to resolve the isotopic structure of mercury with the linewidth of the laser. A narrower linewidth would enable better resolution, which is the case for a continuous wave laser diode. Frequency doubling can and has already been done with laser diodes, so that doing cavity ringdown spectroscopy on ICP for mercury detection with a continuous wave laser diode may be realizable in the near future.

CHAPTER V

CAVITY RINGDOWN SPECTROSCOPY INVESTIGATION OF URANIUM ISOTOPES IN AN INDUCTIVELY COUPLED PLASMA

5.1 Introduction

The spectral resolution of uranium isotopes has been the topic of many analytical and spectroscopic studies.[159,160,161,162,163,164,165,166] This stems from the fact that the commonly used radiochemical method cannot be applied with isotopes having a low activity. A method for on-site isotope ratio determination in radioactive waste processing is needed. To accomplish such a task, it is necessary to take into account many parameters such as costs, instrument size, sensitivity as well as selectivity. The standard technique for determining isotopic compositions of actinide elements is thermal ionization mass spectrometry (TIMS). It is accurate and precise, but requires sample preparation and analyte separation. One of the most sensitive techniques is inductively coupled plasma mass spectrometry (ICP-MS). One of its drawbacks is the high maintenance it requires to operate and also its complexity. Typical detection limits for uranium are in the vicinity of 0.02 ng/mL,[167] but sometimes can be as low as 0.3 pg/mL.[168] Another drawback of the technique is isobaric interference – that is its

difficulty of being able to discriminate between ^{238}U and ^{238}Pu, for example. ICP emission spectrometry (ICP-ES) has been successively and extensively used for uranium isotope determination. Furthermore, it can be used for both aqueous and solid samples when used in conjunction with a nebulizer or a laser-ablation system, with achieved sensitivity of 16 ng/mL.[169] To resolve isotopic line splittings, ICP-ES needs a high-resolution spectrometer, which is typically large as well as expensive. ICP laser-induced fluorescence (ICP-LIF) studies have been reported[170]. This technique has the great advantage of being simple, low costly, highly selective and greatly sensitive. Human et al.[171] obtained a detection limit of 20 ng/mL at the 409.01 nm ionic line of uranium. Vera et al.[172] were able to measure the isotopic shift of a 1:1 $^{235}U/^{238}U$ isotopic ratio in 50 and 100 μg/mL solutions of a complex matrix. They as well reported a limit of detection of 2 μg/mL for this line. Laser ablation studies with uranium isotope ratio determination using a diode laser at 682.69 nm was realized more recently. [164] The authors of the study reported isotopically resolved spectra with the natural abundance ratio, with a detection limit of 0.6 and 1.3 μg/mL obtained with two different data collecting modes. Uranium is a relatively difficult element to atomize, so that it needs a relatively high plasma temperature compared to other elements, such as mercury and lead. Because of its low ionization potential (6.08 eV), we expect it to have a high ionic population as well as a low ground state population. In addition, uranium can fluoresce from a large number of energy levels compared with mercury or lead, making the population in each particular initial transition state lower. These factors make uranium an unfavorable candidate for high sensitivity techniques, such as traditional absorption and LIF coupled with an ICP.

This chapter, which has been previously published,[173] reports an extensive study of measurements of uranium isotopic shift for several absorption lines and compare the ringdown detection limits with figures of merit given by LIF. Transitions, line splitting and line strengths of the observed uranium lines were found in the literature.[174,175,176]

5.2 Results and discussion

5.2.1 286.57-nm U II Line

The 286.57 nm transition occurs between the ion ground state energy 0 and an upper state which has an energy of 34866 cm^{-1}. The isotope shift is large enough (1.047 cm^{-1}) at this wavelength (see Table 5.2-1) to be observed and the transition is relatively strong.

Table 5.2-1 The measured isotope shift and detection limits.

Line position (nm)	Shift up level	Shift low Level	Shift cm-1	Shift (pm)	Shift Exp	gf (exp)	CRDS DT (ng/mL)	LIF DTL
286.57 (II) U238	1.047	0	1.047	8.6	10		600	2 μg/mL
286.57 (II) U235	1.047	0	1.047	8.6	10		145	150 ng/mL
358.48 (I) U238	0.58	0	0.58	7.45	5	2.4	300	0.6 &1.3**Error! Bookmark not defined.** μg/mL
409.01 (II)	1.124	0.841	0.283	4.73	2	0.2	315	20 ng/mL[171] 325 ng/mL[177]

5.2.1.1 Isotopic Resolution

A high-resolution scan around this wavelength shows two background peaks (see Figure 5.2-1) which are very close to the OH radical rotational absorption (A-X, 1-0

band), namely Q_{12} (J''=7.5) at 286.552 and P_2 (J''=7.5) at 286.567 nm. However, the difference with these lines and the observed lines is about 0.6 pm which implies that these lines are due to something else than OH. The lines were still present even with the nebulizer turned off. One of these background lines overlaps with the ^{238}U peak (near peak 1 in Figure 5.2-1) and partly with the ^{235}U absorption peak (which is peak 2). We were not able to observe any LIF signal at this wavelength for these background absorption lines.

By subtracting the background from the signal obtained with a 1:1 $^{235}U/^{238}U$ 2.5 µg/mL mixture solution, we obtained the signal plotted in Figure 5.2-2. As one can see, the ^{238}U absorption signal is 7% smaller than that of ^{235}U. This effect could be from the background absorption feature which tends to saturate the signal of the ^{238}U transition. Laser-induced fluorescence isotopic resolution at this wavelength was determined[177] and displayed a 1:1 $^{235}U/^{238}U$ ratio. From the high resolution scan, we have measured a 10-pm isotopic splitting (a little larger than the 8 pm reported in previous publications). The small peak located on the bottom right of the ^{238}U remains unassigned.

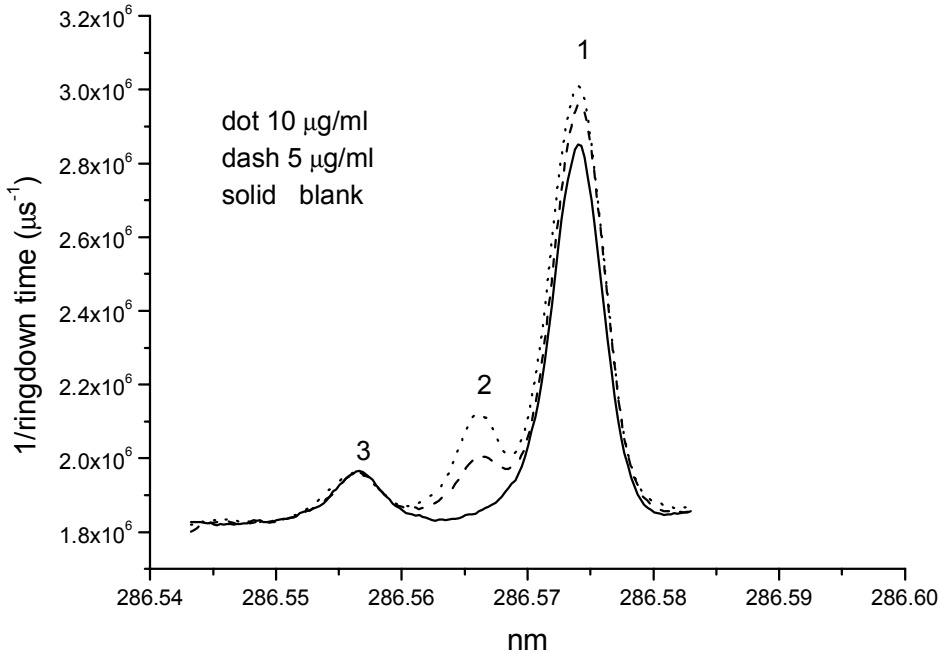

Figure 5.2-1. ICP-CRDS signal around the uranium ionic transition at 286.57 nm. The solid line is the background scan from the argon plasma without any uranium sample injection (blank). The dashed and the dotted lines represent scan of a 1:1 $^{235}U/^{238}U$ mixture with concentrations of 5 μg/mL and 10 μg/mL. Peak 1 is ^{238}U; peak 2 is ^{235}U and peak 3 is an unidentified interference from the argon plasma.

Figure 5.2-3 shows a scan of a 0.714% natural abundance $^{235}U/^{238}U$ solution where the ^{235}U solution concentration is 1.25 μg/mL. The ^{238}U peak is largely saturated so that the peak ratio does not reflect the ratio of the isotopes, but this scan shows that ^{235}U peak is still resolved at the edge of the huge ^{238}U absorption peak.

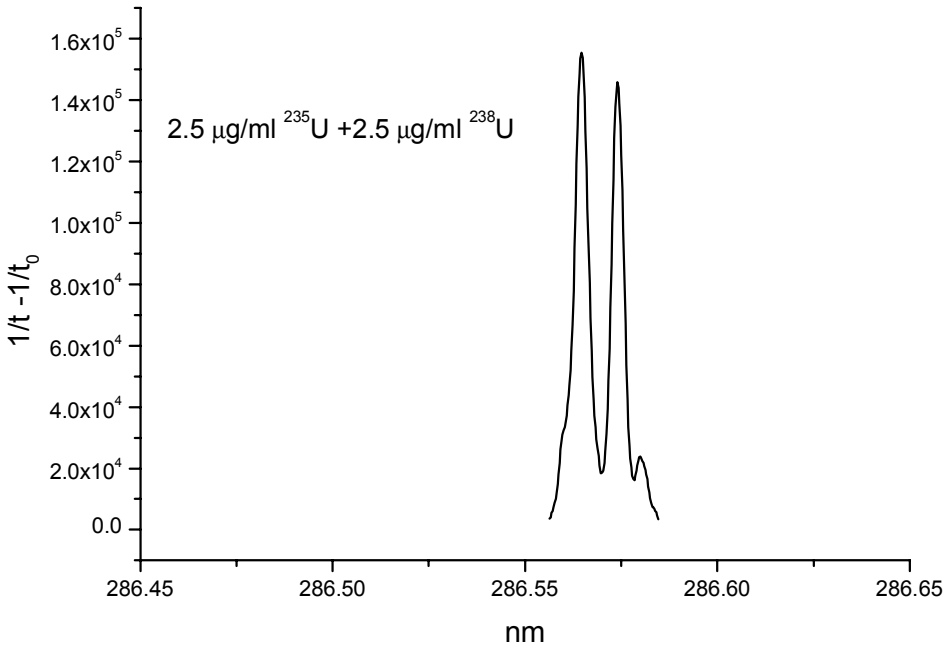

Figure 5.2-2. ICP-CRDS baseline substracted spectrum of the uranium transition line at 286.57 nm. 1:1 $^{235}U/^{238}U$ mixture with concentration of 2.5 μg/mL.

5.2.1.2 Analytical Sensitivity

At this wavelength the CRDS analytical performance is better than or equal to the reported LIF results, although the mirror reflectivity is not very high (see Table 5.2-1). Because of the background absorption feature, the 3σ detection limit of ^{238}U is worse than that of ^{235}U. With confidence, we can assert that CRDS can perform better than LIF by several orders of magnitude at this wavelength.

5.2.2 358.49-nm Neutral U I Line

In order to atomize uranium, the RF plasma power needs to be relatively high (around 350-380 W) compared with the RF plasma power used, for example, with lead or mercury (around 200 W), so that the ground state population for uranium might be

depleted. In spite of this, we were able to observe the atomic transition at 358.49 nm, partly because of the strength of the transition (weighted oscillator strength gf_{ik} equals 2.4) and partly because of the inherent high sensitivity of CRDS.

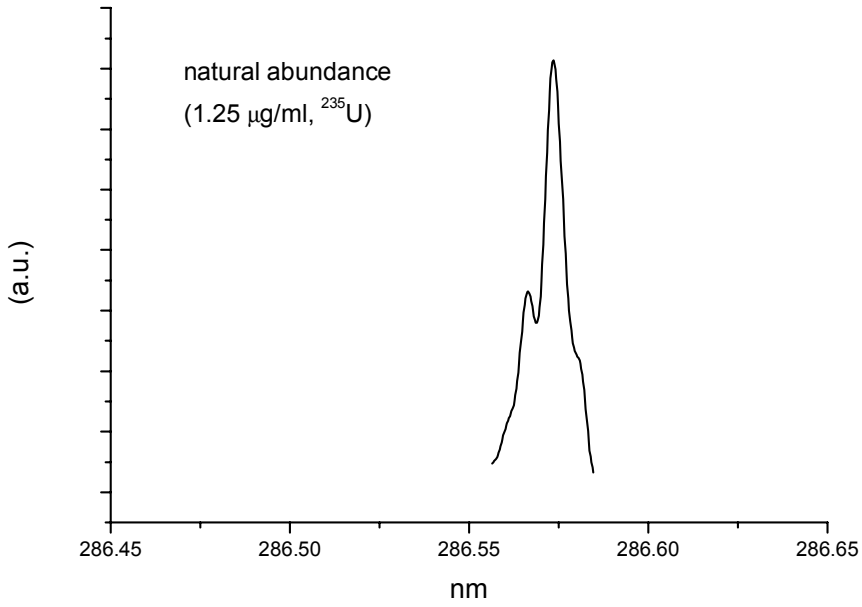

Figure 5.2-3. ICP-CRDS spectrum of the uranium ionic transition at 286.57 nm. The ratio of $^{235}U/^{238}U$ mixture is the natural isotopic ratio (0.714%); the concentration of ^{235}U is 1.25 μg/mL. The spectral intensity does not reflect the mixture ratio because of the strong absorption saturation in the ^{238}U component.

This transition, involving the ground state (0 cm^{-1} energy) and a neutral excited energy state (27887 cm^{-1}) is very strong and easily observable. The detection limit for this line is around 300 ng/mL for a liquid sample, which is lower by a factor of two compared with LIF. Figure 5.2-4 shows the spectrum obtained with a 1:1 $^{235}U/^{238}U$ mixture. The peak intensity does not reflect the isotopic ratio because of hyperfine splitting[164]. A similar feature is observed by ICP-LIF. The peaks are still well resolved

and a splitting of 5 pm was measured. No background absorption feature was observed at this wavelength.

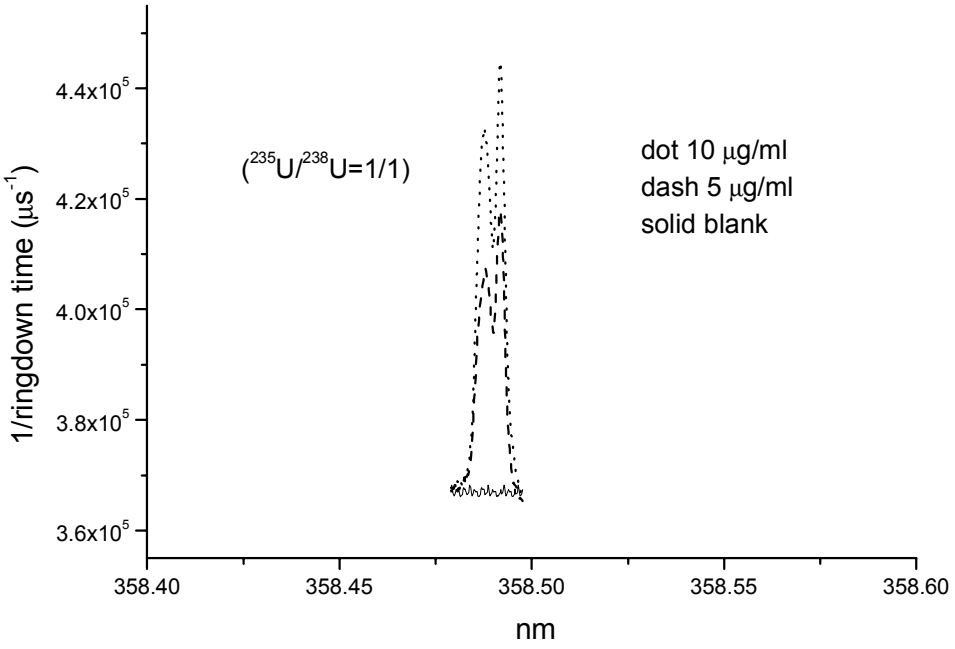

Figure 5.2-4. ICP-CRDS of the uranium atomic transition at 358.49 nm. The solid line represents the baseline from the argon plasma without the uranium sample injection (blank). The dashed and dotted lines represent the scans of a 1:1 $^{235}U/^{238}U$ mixture with concentrations of 5 μg/mL and 10 μg/mL respectively.

5.2.3 409.01-nm U I Line

This absorption line is of interest because of the two following factors:

- very high reflectivity attained by super mirrors at this wavelength.
- this wavelength range is reachable by existing compact diode laser systems

However, the isotopic splitting is only about 0.283 cm^{-1}, but still can be used for isotopic separation with good data processing and a narrower linewidth laser system. The lower state has 1749 cm^{-1} energy; the upper state has 26191 cm^{-1} energy. Figure 5.2-5 shows a

spectral scan given for a 1:1 $^{235}U/^{238}U$ mixture solution (of 2 μg/mL) and the measured isotopic splitting is about 2 pm.

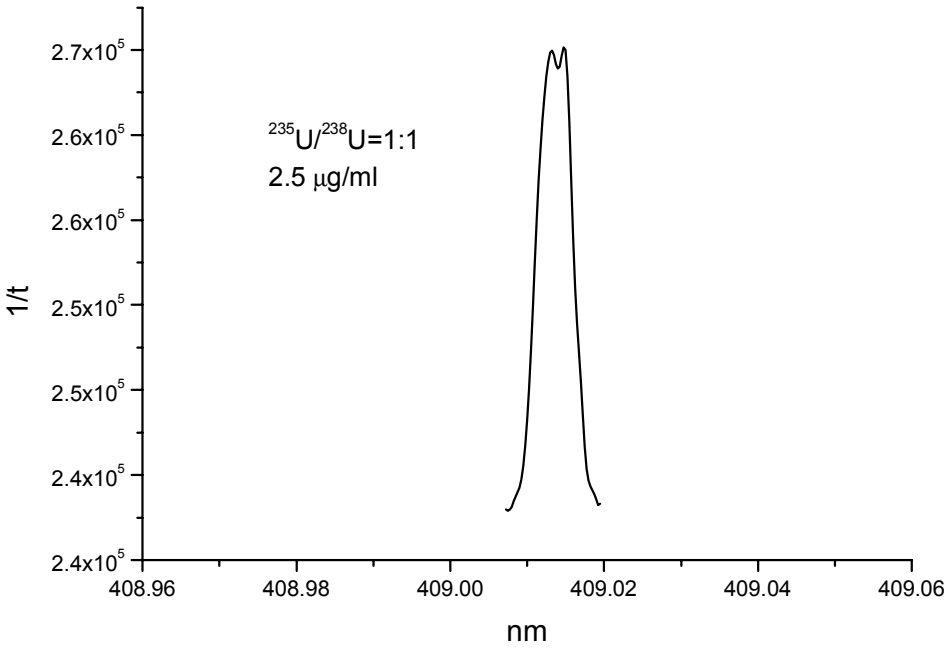

Figure 5.2-5. ICP-CRDS spectrum of the uranium ionic transition at 409.1 nm. The isotope splitting is barely resolved. 1:1 $^{235}U/^{238}U$ mixture with concentrations of 2.5 μg/mL. The bottom line represents the baseline from the argon plasma without the uranium sample injection (blank).

5.3 Summary of results

The ICP was proved to be an ion reservoir as well as an atom reservoir for uranium. Figures of merit were in the range 145-300 ng/mL. This is to be compared with the LIF detection limits found with LIF and published elsewhere. Compared to detection sensitivity obtained with ICP-MS, ICP-ES and ICP-CRDS found for other elements (like lead and mercury), this sensitivity is relatively poor. This is probably due to the low population of atomic and ionic uranium in the probed electronic states. Where detection limits on the order of μg/mL are required (such as DOE sites in USA), this technique has

proven to be successful. Furthermore, a cheap, compact ringdown system could be built by using a small, relatively cheap diode laser instead of a dye laser. Advantage of diode lasers is their ease of use as well as their very narrow linewidth (c.a. 100 MHz). The ever improving super-mirror technology could make this technique much more sensitive than what was obtained in this work. The ease of operation of cavity ringdown compared to ICP-MS for instance makes it a powerful technique that can be used on-site with minimum maintenance.

CHAPTER VI

DEMONSTRATION OF CRDS AS AN ICP DIAGNOSTIC TECHNIQUE

6.1 Introduction

Since its development, inductively coupled plasma (ICP) have been widely used as an atomization and ionization source in a range of spectroscopic techniques. Study of ICP fundamentals provides a way of refining theoretical modeling of such atmospheric plasmas. Such models are very useful in improving spectroscopic performance. Measurements can give access to fundamental ICP parameters, such as gas kinetic temperature, atomic or ionic density, and electron temperature and density. Most ICP studies have been performed with Rayleigh scattering measurements, standard atomic absorption, line broadening, and laser-induced fluorescence.

In this chapter, we prove that CRDS is yet another technique for measuring plasma fundamentals. To our knowledge, this work was the first to investigate the fundamentals of an ICP running at very low power (200W).

6.2 Abel Inversion

Abel inversion transforms a lateral line-of-sight absorption signal I(x) into a radial quantity i® across an axi-symmetric plasma. This procedure is given below:

$$i(r) = -\frac{1}{\pi}\int_{r}^{R_0}\frac{I'(x)}{\sqrt{x^2 - r^2}}dx, \tag{6.1}$$

where $I'(x)$ is the derivative of $I(x)$. In practice, the load coil is asymmetric, so that the experimental data across the plasma need to be symmetrized. The usual procedure is to fit the data with a polynomial that is plugged into the integral so as to compute the radial distribution. It is necessary to force the derivative of the lateral profile to zero so as to have a definite integral near x=0. For better results, it is possible to fit the data with a third-order spline function with a zero derivative at x=0. The inverse of the Abel inversion is given by:

$$I(x) = 2\int_{x}^{R_0}\frac{i(r)r}{\sqrt{x^2 - r^2}}dr, \tag{6.2}$$

Abel inversion can be used to compute radial intensity (or radial absorbance) given a line-of-sight intensity (or absorption) measurement across the plasma. It can also be used to deduce radial atomic profiles (like Doppler or Lorentzian broadening). In this case, it is necessary to apply the above Abel inversion for line-of-sight signals obtained for each particular wavelength. One can finally notice that $I(r)$ has units of $I(x)$ per unit length so that loss per pass becomes absorbance.

6.3 Atom Density Variation with ICP Parameters

Lead atomic density variation was investigated as a function of ICP power, lateral displacement and height. The signal intensity is strongly related with these parameters,

which are important for analytical performance. The experimental conditions of ICP operation are listed in Table 6.3-1.

Table 6.3-1. Experimental conditions for the ICP.

ICP Power (W)	Injector Flow (l/min)	Pb concentration (ppb)
200	1.0	100
500	1.5	500
700	1.8	500

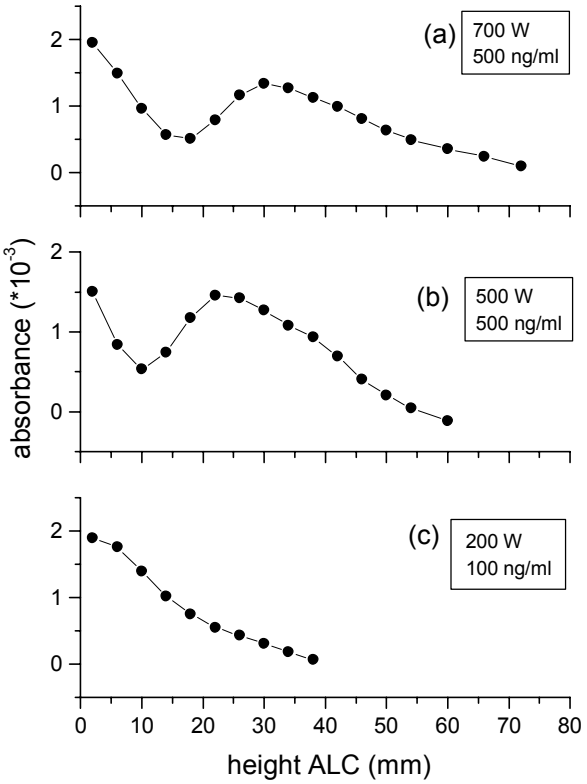

Figure 6.3-1. The vertical absorbance profile of the lead line (283.3 nm) measured using CRDS through the diameter of the torch at different ICP powers. (a) 700 W; (b) 500 W; (c) 200 W.

Figure 6.3-1 shows the line-of-sight absorption variation with height at three different ICP powers. This data was obtained by averaging 20 experimental data points, each obtained by fitting ringdown waveforms averaged over 100 laser shots. For all

powers, the signal was strongest for 2 mm above the load coil (ALC), which implies that the Pb ground-state atom density is larger low in the plasma. However for 500 W and 700 W, one observes a second maximum at 22 mm for 500 W and at 30 mm for 700 W with a valley at 10 mm and 15 mm. Similar behavior was previously reported by a laser-induced fluorescence study[178] for Ca atoms, except that a two-peak phenomenon for powers greater than 750 W only was reported. This could be due to excitation to higher states or to ionization of the Pb atoms (which does not occur as extensively at very low power) and recombination to the ground state.

As the power increases, the location of the second absorption maximum shifts further away from the coil. Furthermore, as shown in Figure 6.3-2, the central channel for high power is much narrower than for low power. This can be explained by the higher injector flow rate used for our measurements. These rates were optimized for each power so as to maximize the absorption intensity at 2 mm ALC.

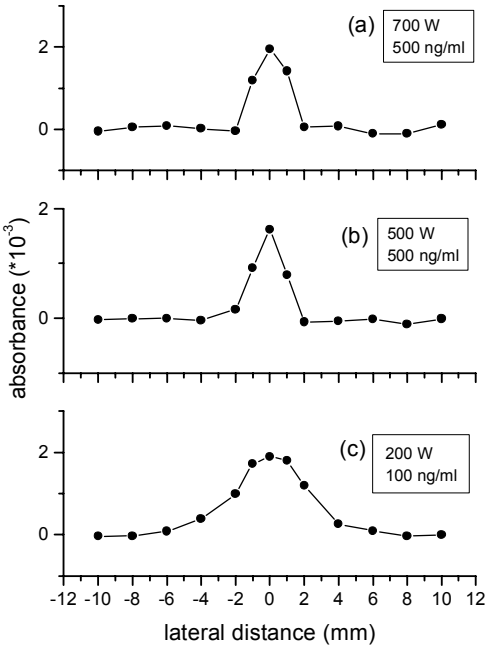

Figure 6.3-2. The lateral absorbance profile of the lead line (283.3 nm) measured using CRDS at 2 mm ALC at different ICP powers. (a) 700 W; (b) 500 W; (c) 200 W

Figure 6.3-3 shows absorbance line-of-sight measurement higher in the plasma versus lateral distance for different powers. For 500 W and 700 W, the observation height was selected to be the absorption second maximum. Because of diffusion, the size of the central channel for higher power is much wider than at 2 mm ALC (7-8 mm versus 4 mm for 200 W).

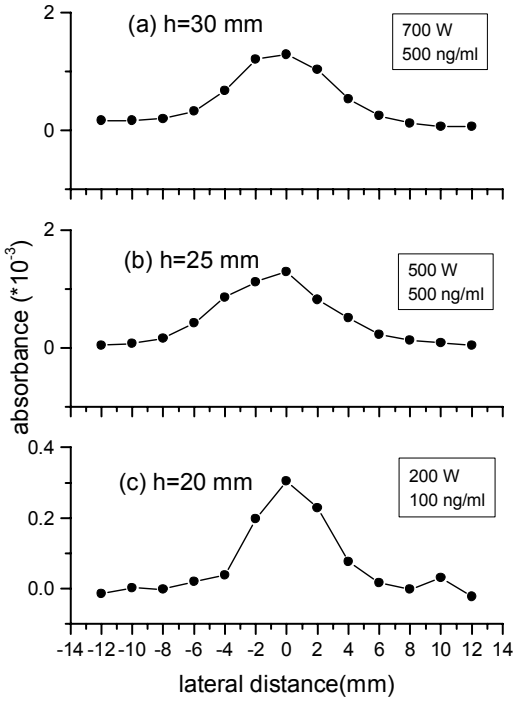

Figure 6.3-3. The lateral profile of cavity ringdown absorption intensity of lead line (283.3 nm) measured at different heights and ICP powers. (a) h = 30 mm, 700 W; (b) h = 25 mm, 500 W; (c) h = 10 mm, 200 W.

Line-of-sight measurements versus lateral distance do not reflect the real radial distribution of lead ground-state atoms, which has to be computed using Abel inversion. Figure 6.3-4a shows symmetrized lateral distance absorbance as well as the third-order spline interpolation of the experimental data. Figure 6.3-4b shows the absorption coefficient (in units of cm^{-1}) obtained from Abel inversion versus radial distance.

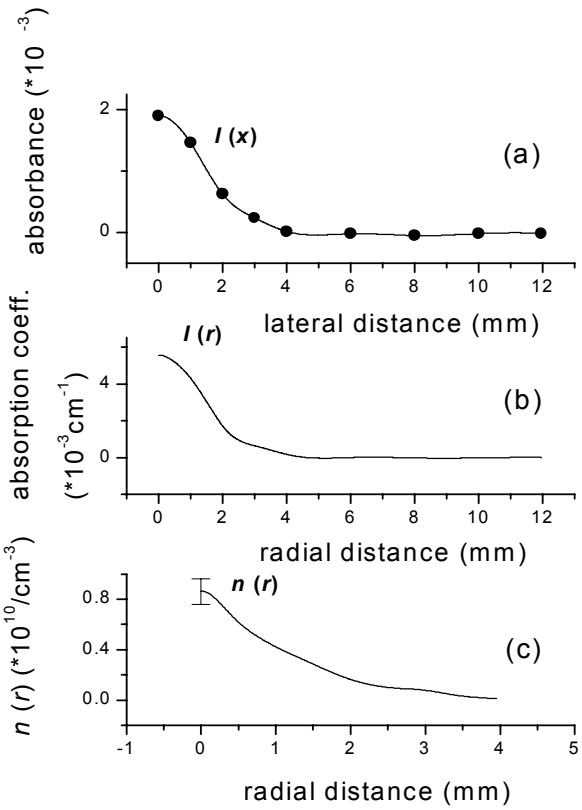

Figure 6.3-4. Example of a line-of-sight measurement (lateral profile) and its Abel inversion (radial profile) using CRDS (283.3 nm, 100 ng/mL). (a) *I (x)* is the lateral absorbance profile measured at 200 W at 2 mm ALC, square and line denote the measurement and the fitted curve, respectively; (b) *I (r)* is the radial profile of the absorption coefficient from Abel inversion of *I (x)*; (c) the radial profile of lead density calculated from the radial profile *I (r)*.

Given the ground state absorption cross section, it is then straightforward to compute the Pb ground state density radial distribution. If one assumes a Voigt profile (the convolution of a Gaussian and a Lorentzian), the absorption cross section is simply given by:

$$\sigma_{pq} = \frac{\lambda^4}{4\pi^2 c} \cdot \frac{g_p}{g_q} \cdot \frac{A_{pq} \cdot V(a,0)}{w_D} \cdot (\pi \ln 2)^{\frac{1}{2}}, \tag{6.3}$$

where A is the Einstein coefficient of spontaneous emission (in s^{-1}); w_D is the Gaussian component; *a* is a quantity (called the *a* parameter) indicating the ratio between Lorentz and Doppler widths; and V(a,0) is the value at the line center of the Voigt function and is defined as:

$$V(a,\omega) = \left(\frac{a}{\pi}\right)\int_{-\infty}^{+\infty} \frac{e^{-t^2}}{a^2 + (\omega - t)^2} dt \,, \tag{6.4}$$

The variable ω is a translated and rescaled version of the frequency (or wavelength) as defined by:

$$\omega = \frac{2(\ln 2)^{\frac{1}{2}}(\lambda - \lambda_0 - d)}{w_D} \,, \tag{6.5}$$

where λ is the wavelength, λ_0 the center of the line, and *d* the line shift.

It is worth noting that absolute gas densities are not as readily measured by optical emission or laser-induced fluorescence, since these techniques give relative intensity measurements and hence need to be calibrated. Cavity ringdown, an absorption-based technique, is already self-calibrated and directly gives absolute absorption measurements and hence absolute densities. From the Abel inverted absorbance profile, it suffices to divide by the cross-section to get absolute densities.

In the present case, the estimated absorption cross section of the 283.3 nm transition is given in Table A-2 for different line-of-sight lateral measurements of Doppler broadening and *a* parameter (see following section). For these calculations, the Einstein A_{pq} coefficient was taken to be equal to $0.58 \cdot 10^8$ s^{-1} and the degeneracy of the

atomic electronic state is 3/1. The cross section varies in the range $6.3 \cdot 10^{-13}$ to $11.5 \cdot 10^{-13}$ cm^2 from x=0 mm to x=4.0 mm across the plasma. We might infer that it is likely to remain in the same range for larger values of x. By taking a constant value for the cross section of about $8.0 \cdot 10^{-13}$ cm^2 to compute the density, we introduce an error of 20% in determination of the density. If we limit ourselves to the range 0 mm < x < 4 mm, we can interpolate the calculated cross section with a 4-th degree polynomial (Figure 6.3-5) and use it to compute a possibly more accurate radial density (Figure 6.3-6).

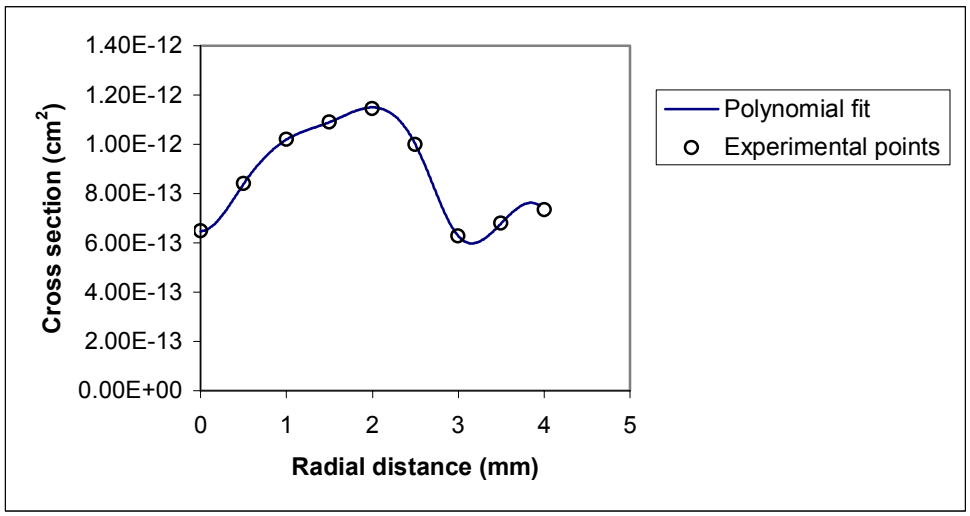

Figure 6.3-5. Interpolated cross section (in cm^2) with a polynomial of degree four.

In the central region where the plasma is cooler, using a median *a*-parameter, constant cross section leads to a slight underestimation of the number density, while in the region where the plasma kinetic temperature is higher than 3000 K, it leads to an overestimation. It is also worth noting that these atomic densities, because of the uncertainty in the A parameters found in the literature (which can be on the order of 30%-100%), are not meant to be a high precision absolute measurement, but are, within at most a factor of two, a good quantitative representation of the density.

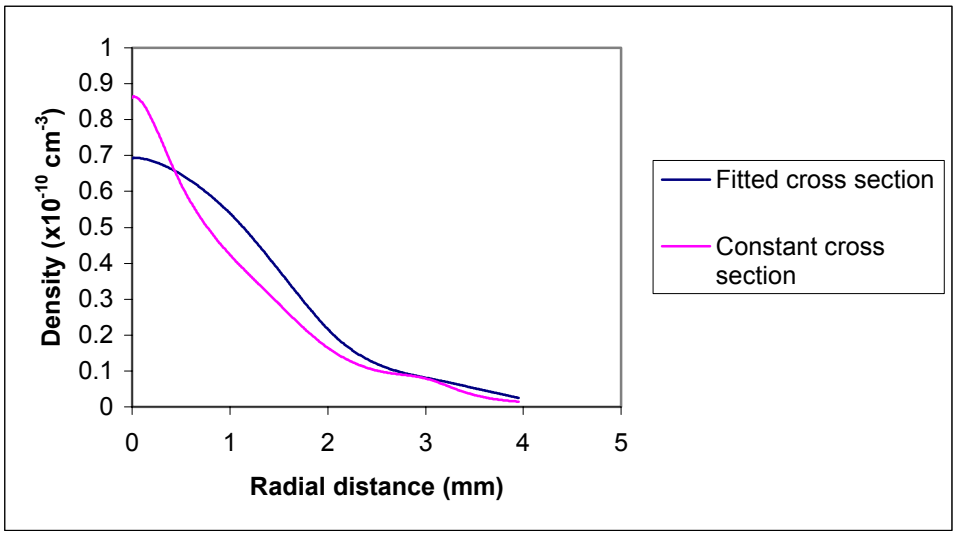

Figure 6.3-6. Graph showing the density ($x10^{10}$ cm^{-3}) versus r (in mm) obtained for a constant cross section and for an interpolated cross section.

6.4 Lineshape Measurements

6.4.1 Different Line Broadening Causes

6.4.1.1 Natural Linewidth

Because of the Heisenberg's uncertainty principle, a ground state atomic transition has a spread in frequency (or linewidth) given by ħA, where A is the Einstein coefficient of spontaneous emission, and its natural lineshape will be Lorentzian. In general, the natural broadening is of the order of 10^{-2} pm, making it negligible compared to the other broadening mechanisms present in the ICP.

6.4.1.2 Doppler Broadening: Gaussian Lineshape

In a plasma or a gas, different particles have different velocities. Because of the Doppler effect, an atom will absorb (or emit) photons with slightly shifted wavelengths. Assuming a Boltzmann distribution of particle velocities in the plasma, the average result

on the lineshape will be a Gaussian component. For an atom of mass M (in a.u.), a kinetic temperature T (in Kelvin), and a transition wavelength λ (in nanometers), the Doppler broadening (full width at half maximum) will be given in nanometers by[179]:

$$w_D = 7.16 \cdot 10^{-7} \cdot \lambda \left(\frac{T}{M} \right)^{\frac{1}{2}}, \tag{6.6}$$

ICP kinetic temperature are typically in the range 5000K-10000K. Hence, typical Doppler broadening widths for Pb at a transition wavelength of 283 nm are typically in the range 1.5 to 2.2 pm in an ICP plasma.

6.4.1.3 Pressure Broadening: Lorentz lineshape

The lifetime of an atomic or molecular energy level is changed by collisions with other species, which cause non-radiative transitions. The resulting lineshape will be approximately Lorentzian, with a width equal to $\bar{h}(A + W_T)$ where A is the transition rate (in absorption or emission) and W_T is the non-radiative transition rate due to collisions. The collisional broadening can be separated into Stark broadening involving collisions with ions and electrons, and van der Waals broadening involving collisions with neutral particles. There can also be resonance broadening when the concentration of the upper state or ground state atoms is high. In case there is no resonance broadening, Stark broadening will be predominant for a plasma with a ionization degree greater than 0.1%.

6.4.1.4 Overall Lineshape: Voigt Profile

In general, an absorption line will be a convolution of a Gaussian and a Lorentzian profile. For an atmospheric plasma, such as the ICP, and within its usual

ranges of temperature, the *a*-parameter defined as $a = (\ln 2)^{\frac{1}{2}} \frac{w_L}{w_D}$, can be close to unity. The total Lorentzian linewidth w_L can be expressed as the sum of Stark, van der Waals, and resonance broadening. We neglect natural broadening because it is much narrower than the others in an ICP plasma.

6.4.1.5 Instrumental Broadening

In case of absorption, broadening is introduced by the laser linewidth w_I. It is common procedure to assume the laser spectrum has a Gaussian lineshape. In this case, the experimental lineshape will have a total Gaussian component equal to $\sqrt{w_I^2 + w_D^2}$. Our laser had a linewidth of approximately 0.08 cm^{-1} in the UV. We opted to de-convolute the experimental spectra using a Gaussian having the same width as the laser.

6.4.2 Experimental Lineshape Analysis

Data processing was performed using the PeakFit 4.0 software package (SPSS Inc, Chicago, IL.). All experimental lineshapes were converted to wavenumber spectra, five-point smoothed, de-convoluted by a Gaussian function of FWHM equal to the linewidth of our laser, and re-smoothed by fast Fourier transform (FFT) filtering (70-80% levels) which simply zeroed the upper frequency channels of the Fourier spectrum. The peaks were then fit to a Voigt profile. The convergence criterion was set to 1% of the Gaussian width. To avoid multiple peak selection from the background, we selected an amplitude rejection threshold of 5%. The fit quality (determined by r^2, probability that the fit be the real function) depended greatly on the peak location that the program would automatically assign. To control this, we could change baseline tolerance (< 4%) (i.e., the

percentage of data points taken by the program to make a baseline estimation) and the FFT smooth level (70-80%) so as to visually obtain a good match between experimental data and calculated fit. This method of proceeding gives fits with r^2>97%. The Voigt function used by the program was defined as follows:

$$\frac{a_0 \int_{-\infty}^{+\infty} \frac{e^{-t^2}}{\left[\frac{a_3^2}{2a_2^2} + \left(\frac{x-a_1}{\sqrt{2}a_2} - t\right)^2\right]} dt}{\int_{-\infty}^{+\infty} \frac{e^{-t^2}}{\left(\frac{a_3^2}{2a_2^2} + t^2\right)} dt} \tag{6.7}$$

The fit parameters are defined as follows:

- a_0 is the amplitude
- a_1 is the line center
- a_2 is related to Doppler component by $w_D = \sqrt{2} \cdot a_2$
- a_3 is related to the *a*-parameter by $a = \frac{a_3}{\sqrt{2} \cdot a_2} = (\ln 2)^{\frac{1}{2}} \frac{w_L}{w_D}$ so that $w_L = \frac{a_3}{(\ln 2)^{\frac{1}{2}}}$

Line-of-sight lineshapes were measured for several observation heights and lateral displacements, enabling analysis of Lorentzian and Doppler components in different locations of the ICP. Data were recorded for a power of 200 W and a flow rate of 1 L/min. The data are summarized in Table A-1 (for different observation heights, ranging from 2 to 30 mm) and in Table A-2 (for several lateral positions at a height of 2 mm ALC). Figure 6.5-1 shows the experimental measurement with the corresponding fit. Figure 6.5-4 shows some linehapes for different observation heights. Figure 6.5-2 and Figure 6.5-3 show lineshapes and corresponding Voigt fits as examples.

6.5 Pb Atom Kinetic Temperature Measurements

Gas kinetic temperature in ICPs has been extensively studied in the literature. Doppler line broadening has been studied in emission as well as in absorption. Rayleigh scattering (produced mainly by neutral argon) is proportional to the scatterer density, so that it is possible to extrapolate kinetic temperature by assuming the ideal gas law ($N/V=P/kT_k$)

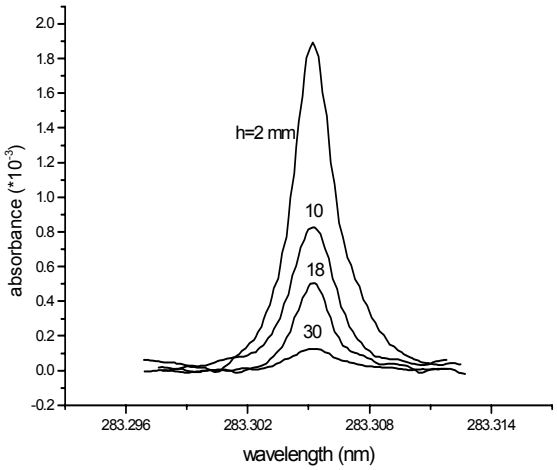

Figure 6.5-1. Measured lineshape of lead line (283.3 nm) versus height. ICP power = 200 W; lateral distance x = 0 mm; from top to bottom, h = 2, 10, 18, and 30 mm; lead solution: 100, 100, 200, and 500 ng/mL.

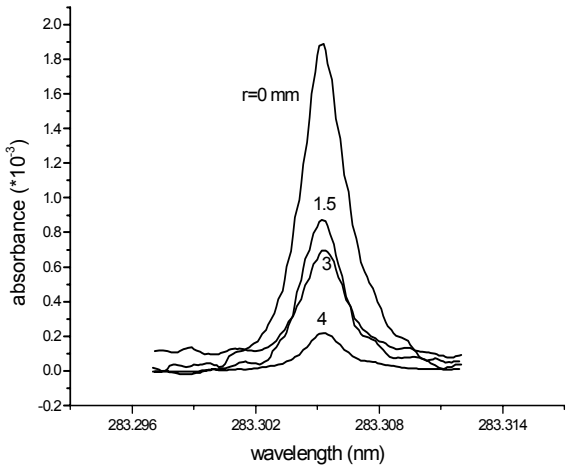

Figure 6.5-2. Measured lineshape of the lead absorption line (283.3 nm) versus lateral position. ICP power = 200 W; height (h) = 2 mm; from top to bottom, lateral positions (x) are 0, 1.5, 3, and 4 mm; lead solutions are 100, 100, 200, and 500 ng/mL.

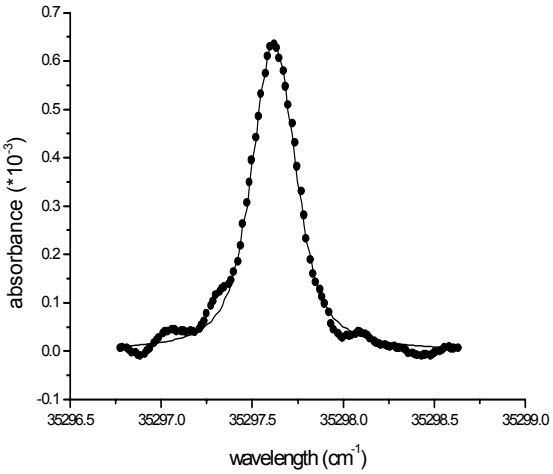

Figure 6.5-3. An example of the fitted lineshape of the ICP-CRDS absorption line (lead, 283.3 nm) measured at 200 W; height (h) = 2 mm ALC, lateral distance (x) = 1.5 mm. Dot and line denote the experimental and the fitted curves, respectively. r^2 coefficient of determination = 0.99; std error = 0.011.

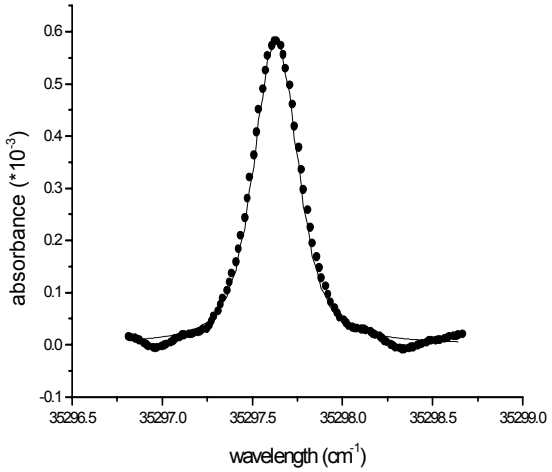

Figure 6.5-4. An example of the fitted lineshape of the ICP-CRDS absorption line (lead, 283.3 nm) measured at 200 W at 10 mm ALC through the diameter of the torch. Dot and line denote the experimental and the fitted curves, respectively. r^2 coefficient of determination = 0.99; std error = 0.0082.

Thomson scattering gives access to electron densities as well as electron temperature. Because of high electron velocities (100-1000 km/s), Thomson broadening can be around 5 nm. In Thomson scattering experiments, Rayleigh scattering can be rejected by simply masking the dispersed light around the laser central wavelength (Rayleigh scatter has a very small frequency dispersion compared to electron scattering). Argon line absorption lineshapes have already been used for temperature and electron density measurements by J.M de Regt *et al.*[180] and provide a good background for our work.

Figure 6.5-5 shows the variation of kinetic temperature with height. The stability of the Doppler lineshape was around 10% low in the plasma and reached 15% at a height of 30 mm (1 standard deviation variations). This gives an absolute uncertainty of the temperature of around 500 K (indicated on the graph by the error bars) for all temperatures. The temperature starts at 2800 K low in the plasma and decreases to about

1900 K at 30 mm ALC. The line-of-sight lateral scan is shown in Figure 6.5-6. For x<1.5 mm, the variation for linewidth are about 10%.

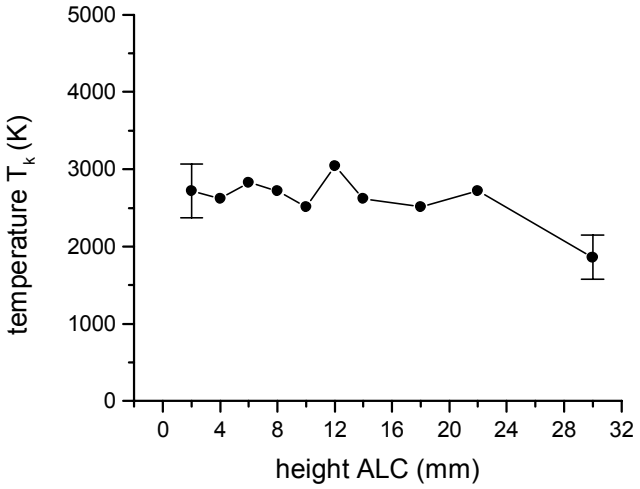

Figure 6.5-5. Vertical profile of gas kinetic temperature through the diameter of the torch. ICP power = 200 W. Two error bars show the maximum and minimum error (1 σ).

Because of increased baseline instability for x>1.5 mm, the Lorentzian component has broader fluctuations (from 20% to 30%) and the Gaussian component is subject to 15% variations. Figure 6.5-6 gives the temperature uncertainty at the edges of the lateral scan. The general trend of the temperature profile is a bell shape with maximum at 1.5 mm. This lateral scan shows cooler temperature in the center of the plasma and is very similar in its trend to the one made by J.M Regt *et al.*[180] for diode laser absorption on a 4s-4p neutral argon transition. In their experiment, their laser beam was positioned at 7 mm ALC and they used a higher RF power (0.9 kW-1.8 kW). Their Abel inverted profile starts at around 2000 K at r=2 mm and reaches a maximum temperature at r=4mm. For 0.9 kW, the maximum observed temperature was about 4000 K, which is similar to ours. Since our data reflects a line-of-sight profile, it is not possible to make a direct

comparison with their studies, other than the general variation of temperature. The shorter radial location of maximum kinetic temperature is probably due to our lower RF power. Rayleigh scattering data of kinetic temperature measurements also show similar trends to ours for a power of 750 W at a height of 5 mm ALC.[179]

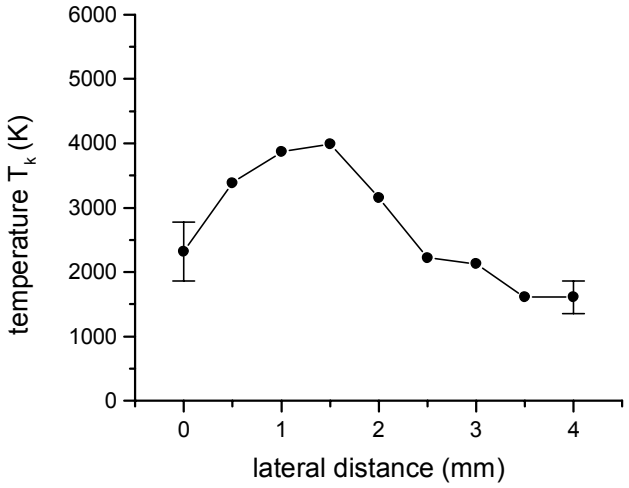

Figure 6.5-6. Lateral profile of gas kinetic temperature at 2 mm ALC at 200 W. Two error bars show the maximum and minimum error (1 σ).

6.6 Electron Density Evaluation

The Lorentz broadening component enables us to plot line-of-sight electron density versus height (Figure 6.6-1) and lateral displacement (Figure 6.6-2). The electron density is obtained by assuming that pressure broadening is entirely given by Stark broadening. Such an assumption is doubtful in atmospheric plasmas and will be discussed below. The Stark broadening is approximately given by the following formula:[181]

$$w_S \approx 2[1+1.75\times10^{-4} n_e^{1/4}\alpha(1-0.068 n_e^{1/6} T_e^{-1/2})]10^{-16} w n_e, \tag{6.8}$$

where n_e is the electron density and T_e is the electron temperature. The parameters α and w are, respectively, the ion-broadening parameter and the electron half width. These parameters are tabulated[181] and were chosen as $\alpha = 0.082$ and $w = 0.0973$ Å. The

electron density dependence on T_e is relatively weak (less than 5% by taking T_e=5000 K or 7500 K) when all other parameters are kept constant. Because of the well known relationship $T_e \approx 1.7 \cdot T_k$,[219] we took T_e=7500 K based on the higher kinetic temperature measurements. This gives electron densities of around 2×10^{14} - 5×10^{14} cm^{-3}, which is in accord with the 5×10^{14} - 5×10^{15} cm^{-3} range found in the literature.[179]

This could be attributed to the drastically lower RF power used in our experiment and our different ICP torch configuration. The electron density starts around 5×10^{14} cm^{-3} (at 2 mm ALC) in the center of the plasma, decreases to a minimum (equal to about 2×10^{14} cm^{-3}) at r=2mm and then comes back up to about 5×10^{14} cm^{-3}. Experiments made with Thomson scattering show that actually the electron density has a reversed tendency with a minimum in the center of the plasma and on the edge, and with a maximum in between.

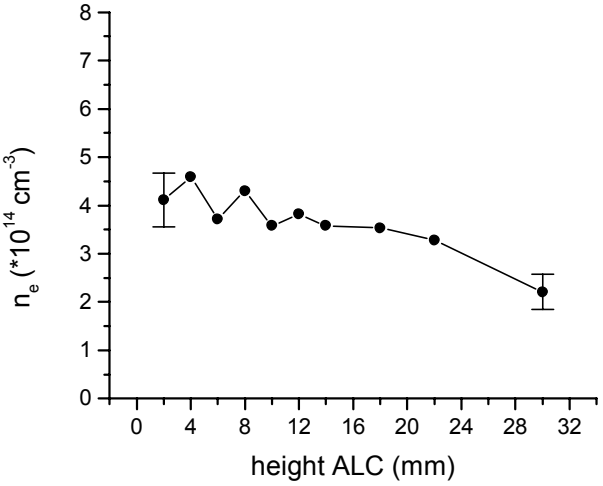

Figure 6.6-1. Vertical profile of electron density through the diameter of the torch. ICP power = 200 W. Two error bars show the maximum and minimum error (1 σ).

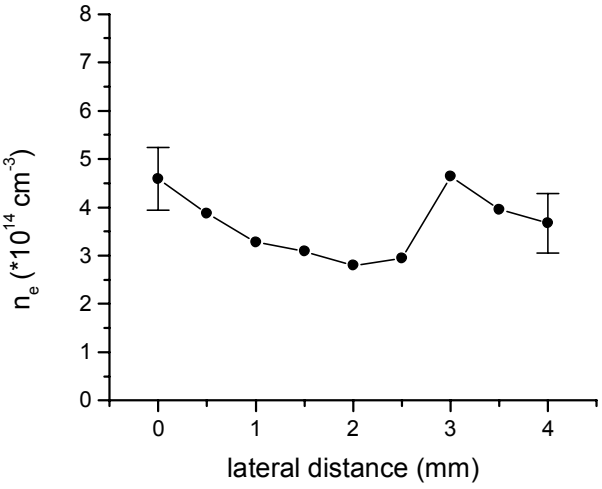

Figure 6.6-2. Lateral profile of electron density at 2 mm ACL at 200 W. Two error bars show the maximum and minimum error (1 σ).

Our observed behavior comes from the assumption that the pressure broadening is equal to the Stark broadening. This might be true in the central area of the lateral profile where electron density and temperature are higher and where van der Waals broadening is lower because of lower neutral argon density due to higher gas temperature. In their absorption study of Ar 4s-4p broadening transition, de Regt *et al.* [182] estimated van der Waals effect by a proportional neutral Ar density law as follows:

$$\gamma = \frac{\Delta\lambda_W}{n}, \tag{6.9}$$

where n is the neutral gas density deduced from the gas law and kinetic temperature measurements, $\Delta\lambda_W$ is the van der Waals broadening (in nm), and γ is a constant (in nm/m^{-3}). By assuming that at the edge of the plasma, Lorentz broadening would be completely van der Waals, they estimated that the ratio between these two widths ranged from 0.45 (at r=4 mm) to 0.95 at r=8mm. In our case, Lorentz broadening has a maximum at r=3mm, where the temperature is around 2000 K. By assuming a 50% van

der Waals / 50% Stark broadening for this point, we can estimate the electron density to be at most 2×10^{14} cm^{-3}, thus giving an estimate of its upper bound. Figure 6.6-2 shows a slight decrease of electron density with height.

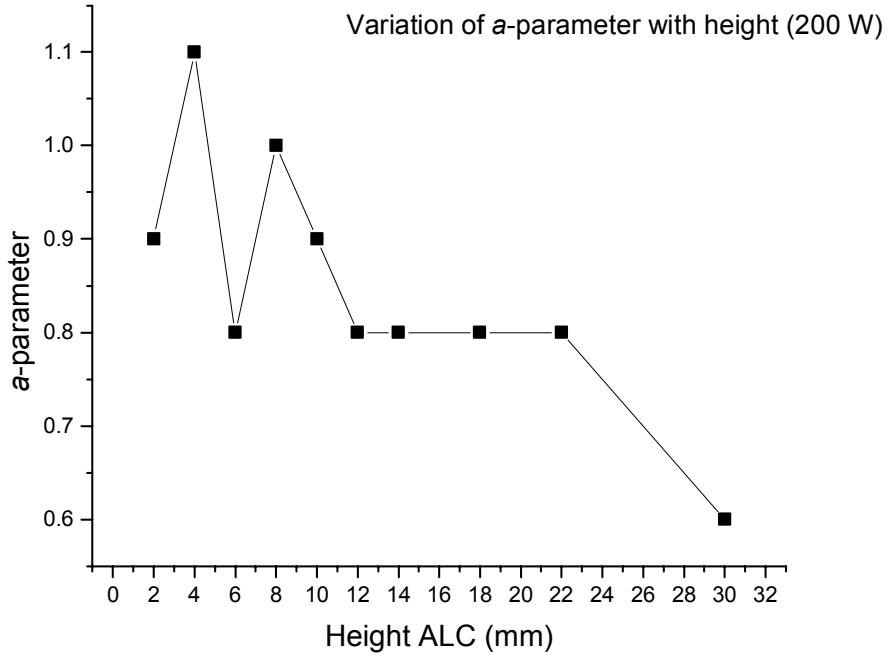

Figure 6.6-3. Variation of the *a*-parameter with height at 200 W.

Furthermore, as shown in Figure 6.6-3, the *a* parameter first increases to maximum around 6 mm ALC, then decreases with height. This seems counterintuitive because high in the plasma, the Gaussian component should drop (because of a decrease in gas temperature) while the Lorentzian component should increase because of higher gas density. This trend can be explained by combination of a faster decrease in Stark broadening (due to decrease in electron density) than the van der Waals effect increases (due to a relatively slow kinetic temperature drop), thus confirming a relatively high

Stark component in the total pressure broadening. One would expect the Lorentz width and consequently the *a*-parameter to increase again for higher heights.

6.7 Summary of results

The second study utilizing atomic absorption spectroscopy in the ICP for fundamental measurements following the work performed by de Regt *et al.*[182] with a diode laser on argon ICP has been realized. Gaussian and Lorentzian components were extracted from the atomic lead Voigt lineshape at absorption wavelength of 283.3 nm. The Gaussian component was caused by Doppler broadening and could be used to calculate the gas kinetic temperature of Pb I in the plasma. At the low power used for this plasma in order to maximize ground-state atomic number density, kinetic temperature ranged from 2000 K to 4000 K. The kinetic temperature profile exhibited a dip at the center of the plasma and a maximum at lateral displacement of 2 mm, a behavior similar to the work of de Regt *et al.*[182] The temperature was also found to slowly decrease with height. The Lorentzian component of the lineshape was mainly due to van der Waals broadening and Stark broadening which was considered to be predominant. By neglecting all other broadening processes, we could calculate the electron density in the plasma. The density was found to be in the range 2×10^{14} cm^{-3} - 5×10^{14} cm^{-3}, which can be compared to 5×10^{15} cm^{-3} for laser absorption measurements and to 5×10^{14} cm^{-3} found by Thomson scattering.[182] Considering that in this work the ICP was used with a much lower power (200 W instead of greater than 0.9 kW), these results can be compared to the ones found in the literature.

Cavity ringdown spectroscopy has been demonstrated as a powerful tool for plasma diagnostics at the fundamental level. Further improvements, such as use of a

compact laser diode system, could be done to improve, for example, laser linewidth as well as signal stability.

CHAPTER VII

ICP-CRDS MEASUREMENTS OF OH RADICAL ROTATIONAL SPECTRUM

7.1 Introduction

To this day, the hydroxyl radical has been extensively studied in many environments, such as the atmosphere,[183,184] combustion,[185,186] flames,[187,188] shocks,[189] plasmas[190,191,192] and rocket engine exhausts[193]. Its importance lies in the thermal and chemical characterization of combustion processes. Measurements of OH radical have been done in the frameworks of chemical dynamic studies,[194] kinetics[195] and temperature diagnostics[196] using a number of spectral techniques such as laser-induced fluorescence (LIF)[197] and conventional absorption techniques.[198] Spectroscopic parameters of the OH radical, including pressure-and temperature-dependent cross-sections, have been extensively documented.[199,200] Cavity ringdown spectroscopy (CRDS) has already been widely used to measure absolute concentration of the OH radical.[201,202,203,204,205,206] Among the people who first used this technique on OH radical are Meijer and co-workers[207] who measured OH radical density in air with temperature ranging from 1000 to 1400K. More recently, absolute number densities of OH radical using CRDS were made in a number of combustion studies. [208,209,210,211] All results presented in this chapter have already been published.[212]

7.2 Experimental conditions

A detailed description of the experimental setup can be found in Chapter 3. We will briefly outline the laser characteristics: output from the Narrowscan dye laser was frequency doubled with the Inrad Autotracker to give the desired wavelengths. The dye laser pulse duration was around 5-7 ns and its linewidth was measured to be less than 0.05 cm^{-1} so that the linewidth of the frequency-doubled light radiation at 308 nm was estimated to be 0.08 cm^{-1}. A 780-mm long cavity was used along with two plano-concave super mirrors (Los Gatos Research) of radii of curvature equal to six meters. The reflectivity of the mirrors at 308 nm was 99.85%. The ringdown signal was measured by a photomultiplier tube (Hamamatsu R928) and recorded using a digital oscilloscope (Tektronix TDS 410A) connected to a computer that did the exponential curve fit. For all recorded spectra, 50-100 laser shots were averaged.

For the recorded emission spectrum, a 0.5-meter monochromator (ARC SpectraPro 500) was used. The resolution of the monochromator with a 2400/mm grating was 0.016 nm. The exposure time of the CCD was set to 0.02 seconds and the signal was integrated over ten exposures.

The ICP used was a 1.6-kW, 27.12-MHz argon ICP (SEREN IPS I1600-27). The quartz torch was modified so as to run at the low power of 200 W (wider inlet tube, shorter outer tube) and would sit in a three-turn coil (see Chapter V). Plasma power was set to 200 W and argon flow rates in the outer middle and central tubes were 18.0, 0.0 and 1.0 L/min, respectively. No water aerosol was injected into the plasma torch so the OH comes from atmospheric H_2O thermal dissociation.

7.3 Theoretical considerations

7.3.1 Saturation effects in the CRD spectrum of the OH A-X 0-0 band

Figure 7.3-1a shows part of the CRD spectrum for the OH A-X (0-0) band around 208 nm measured at 10 mm ALC. The ICP operating conditions were described in the previous paragraph. In CRDS, multi-exponential behavior is an indication of some kind of saturation. This saturation effect can have multiple reasons.[213,207,214,215,210] One of this reasons can be that the laser linewidth is larger than the absorption linewidth. The consequence of this is that part of the laser beam will have a shorter ringdown time while the wings of the laser spectral profile will decay with a longer decay time. The overall effect on the ringdown curve is a different ringdown time for shorter times and longer ringdown times for longer times resulting in multi-exponential behavior. In our case, the plasma-broadened OH linewidth (FWHM) is around 0.6 cm^{-1}, while the laser linewidth was estimated to be around 0.08cm^{-1}, implying that the previously described effect will not occur. However, while scanning strong lines in the P_1, P_2, Q_1, Q_2, R_1, R_2, Q_{21} and R_{21} branches, multi-exponential behavior was observed for the ringdown curves. This effect could result in an underestimation of the number density of up to 40%.

The OH absorption spectrum was simulated using the software LIFBASE[216] (see Figure 7.3-1b). Simulations parameters are listed at the bottom of the figure. As expected, larger deviations (40%) are observed with a strong $R_1(10)$ line while the relative intensity of the weaker lines match well.

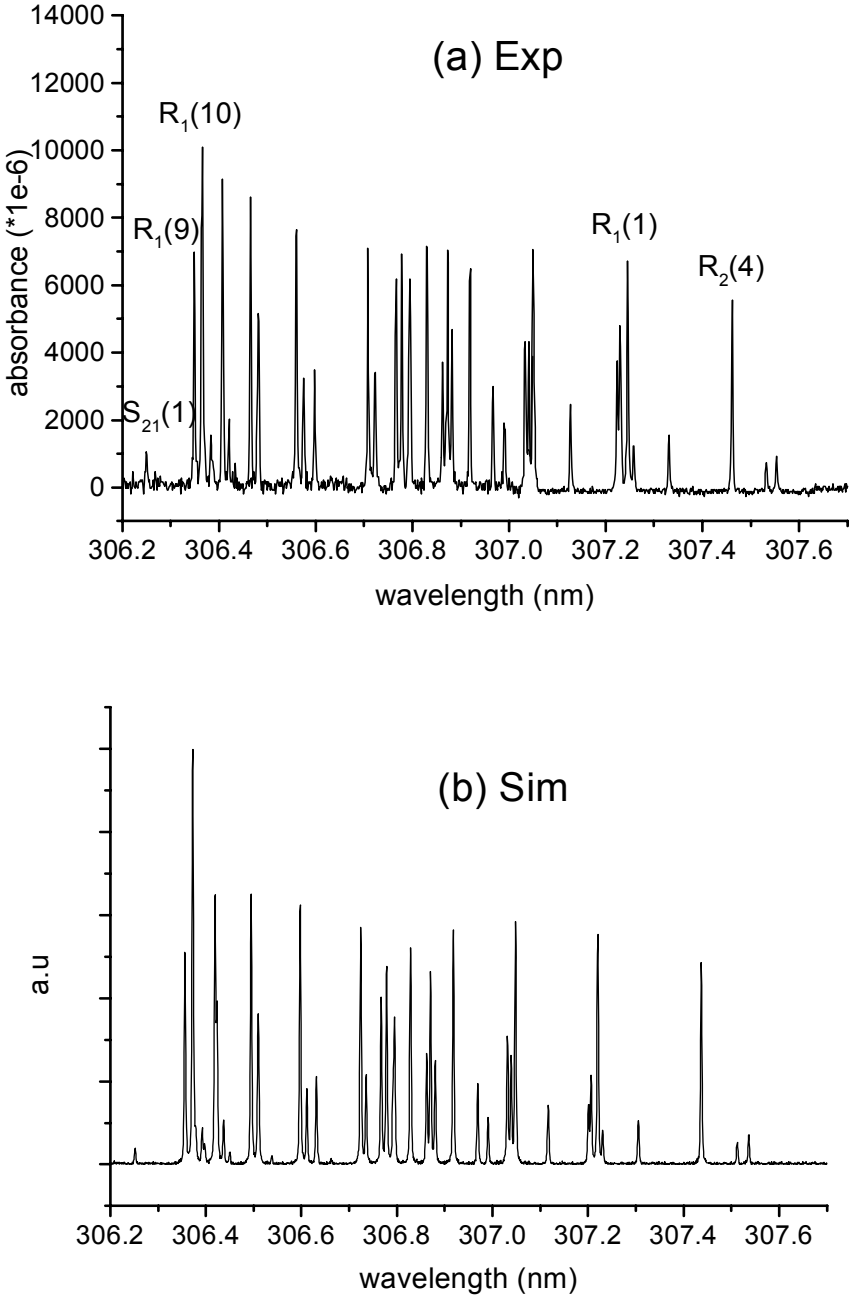

Figure 7.3-1 (a) Part of CRD spectrum of the OH $A^2\Sigma^+ - X^2\Pi$ (0-0) band recorded in the atmospheric-pressure argon inductively coupled plasma. Plasma power = 200 W; h (ALC) = 10 mm; x = 0 mm. (b) Part of the simulated absorption spectrum based on the Boltzmann distribution. The simulation conditions: resolution = 0.004 nm; lineshape = Voigt; Lorentzian component = 30%; Tr = Tv = 2000 K; pressure = 760 torr; 0.5% noise is added to the spectrum.

For the $S_{21}(1)$ line used for OH total density measurements, it was verified that the ringdown curve was single exponential on the range up to 5τ, where τ is the ringdown time and a fitting window of width 3τ was used for measurements. The single exponential decay criterion was set as 1% or less variation in the ringdown time on different fitting windows (τ to 5τ).

7.3.2 Plasma gas temperature from lineshape measurements

In an atmospheric pressure plasma, the mechanisms involved in lineshape broadening are resonance broadening, Doppler broadening, Stark broadening and van der Waals broadening[217,218] (see Chapter IV), the predominant being the three listed last. Doppler broadening will give rise to the Gaussian component of the lineshape, while the three others will be responsible for the Lorentzian component of the lineshape. These effects will contribute to give an overall Voigt profile (see Chapter IV). The influence of each component depends of the species under study (atoms, ions or molecules), the plasma operating conditions and the position of observation. The plasma gas kinetic temperature can easily be derived from the Gaussian component by using the following Doppler equation:

$$\omega_D = 7.16\times10^{-7}\,\lambda_0\sqrt{\frac{T}{M}} \tag{7.1}$$

where λ_0 is the line central wavelength, T is the kinetic absolute temperature and M the atomic mass in atomic units. The laser linewidth is assumed to have a near-Gaussian lineshape, so that the experimental linewidth first has to be de-convoluted by a Gaussian curve of width 0.08 cm^{-1}. Extracting the Voigt Gaussian width from the de-convoluted lineshape yields the kinetic temperature of the plasma. To do this, a commercial software

package (PeakFit 4.0 for Windows, by INSO Corporation) was used. The steps followed are the same as in Chapter 4, namely conversion of the wavelengths to wave numbers, baseline substraction, de-convolution of the experimental linewidth, smoothing of the curve obtained with 20-30% smoothing levels for an overall 98% noise reduction. Amplitude rejection threshold was set to 5% in order to obtain the fit of only one peak. The noise added by the de-convolution method was removed by FFT high frequency domain truncation so as to obtain the best parameter of fit r^2>0.98. A typical fit to the experimental data is shown in Figure 7.3-2. The data was recorded at a height above the load coil of 10 mm, at the center of the plasma. The calculated line-of-sight plasma gas temperatures were in the range of 1800 to 2000K at different plasma heights and are plotted in Figure 7.3-3. The temperatures are accurate within a 10% uncertainty.

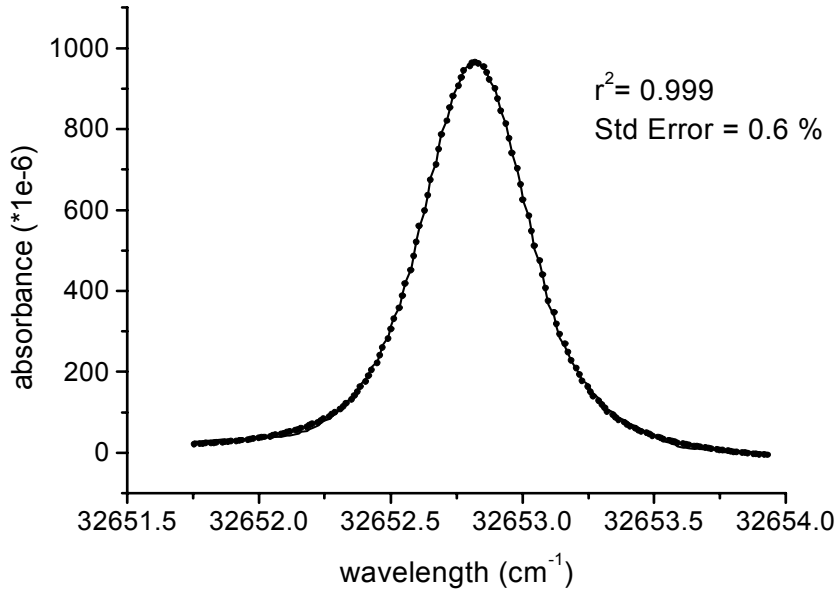

Figure 7.3-2 An example of the fitted lineshape of the $S_{21}(1)$ rotational line in the OH (0-0) band recorded at 200 W and 10 mm ACL through the central of the plasma torch. The dots and the line denote the fitted and the experimental curves, respectively. r^2 coefficient of determination = 0.999; standard error is equal to 0.006.

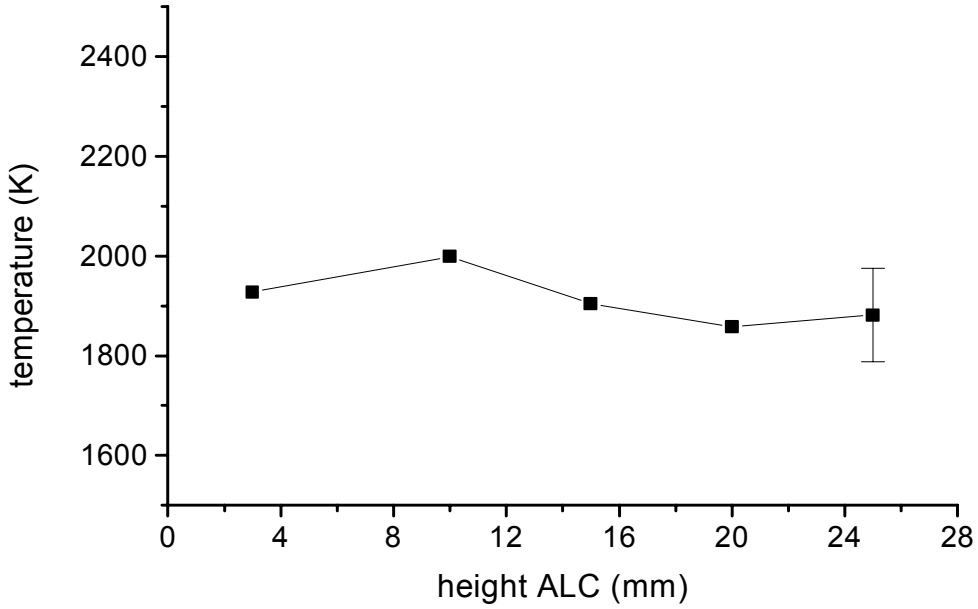

Figure 7.3-3 Vertical profile of gas kinetic temperature measured by CRDS of the $S_{21}(1)$ rotational line in the OH (0-0) band through the central of the plasma torch. Plasma power = 200 W. The maximum uncertainty of the measured temperature is 10% at the tail of plasma.

7.3.3 Local Thermal Equilibrium

Atmospheric-pressure plasmas are often considered to be in or close to local thermal equilibrium (LTE). Factors making this assumption erroneous include large velocity and large temperature gradients within the plasma. A plasma is said to be near LTE when it can be described by multiple temperatures, such as electron temperature (Te), ionization temperature (Ti), excitation temperatures (Tex), and gas kinetic temperature (Tk). Empirically, it has been verified that Te>Ti>Tex>Tk and the ratio Te/Tk stays in the range 1.4 to 1.7 in the ICP.[219] In LTE plasmas, it is assumed that all these temperatures are equal. A plasma is considered to be in LTE whenever the ratio Te/Tk is smaller than 1.1. A single LTE temperature is required to describe the

distribution of the various species composing the plasma; this assumes a single Boltzmann distribution. The plasma considered in this work is low-power, low-flow, and at atmospheric pressure. Measurements of Te/Tk in the past[220,221,222] indicate, for a normally operated ICP, that this ratio is about 1.1. Thus, the plasma used in this work may be assumed to be in LTE. To verify this assertion, an emission spectrum of OH A-X (0-0) band was recorded (shown in Figure 7.3-4a). The spectrum was acquired with 0.08-nm resolution in the middle of the plasma at a height of 10 mm above the load coil. Figure 7.4-2b shows the simulated emission spectrum of this band based on a Boltzmann distribution in the LTE approximation. In order to match the computed spectrum with the experimental one, the rotational and vibrational temperatures had to be set to 2000K. It was verified that a 5% variation of temperature would generate visible differences between these two spectra. The spectral simulation was obtained with LIFBASE software. As shown in Figure 7.3-4, the recorded and computed spectra are identical. This verification enables us to assume that the plasma is in LTE and that only one temperature is required to describe the thermal distribution of the OH radical in the ICP. Furthermore, we previously established that the kinetic temperature was in the range 1800-2000K. This temperature matches, within a 10% accuracy, the LTE temperature found above. This observation tends to support that within the range of heights of observation used in this study, the plasma is in LTE.

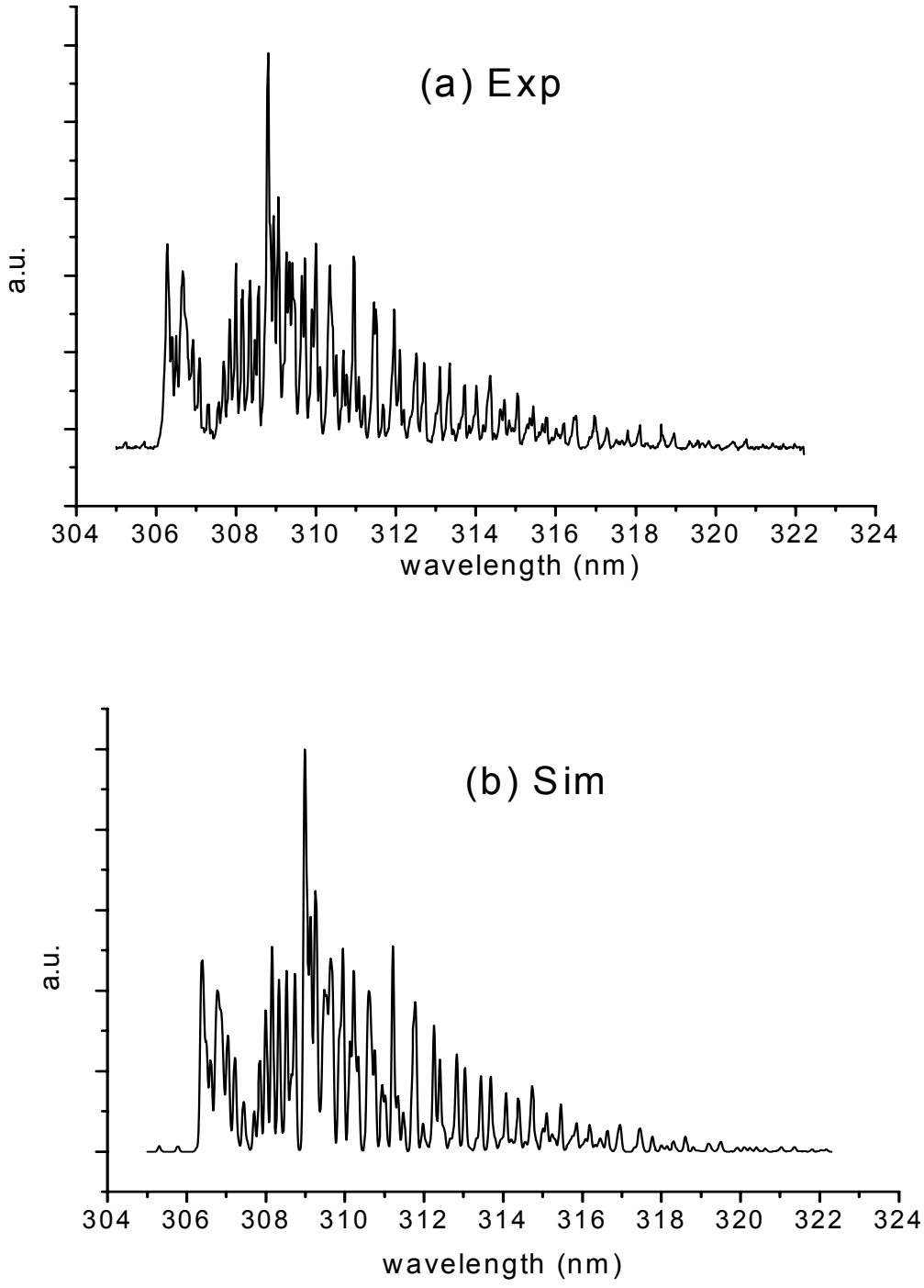

Figure 7.3-4 Emission spectra of the OH $A^2\Sigma^+ - X^2\Pi$ (0-0) band in the atmospheric-pressure argon ICP. Plasma power = 200 W; h (ALC) = 10 mm; x = 0 mm. (a) Measured emission spectrum through an CCD spectrometer; (b) Simulated emission spectrum based on the Boltzmann distribution; Tr = Tv = 2000 K. The spectral resolution is 0.08 nm.

7.4 Total OH density variation with plasma height

7.4.1 Rotational absolute absorption and absorption cross-section

The absolute absorbance in a rotational energy level can be derived from the ringdown time by the following integral over frequency:

$$\sigma_{total}^{ij} nl = \int \frac{l}{c}\left(\frac{1}{\tau} - \frac{1}{\tau_0}\right) d\nu \tag{7.2}$$

where n is the OH number density for initial state of the $S_{21}(1)$ transition, l is the height-dependent absorption pathlength, and σ_{total}^{ij} the total absorption cross section of the transition integrated over frequency. The latter can be derived from the following formula:

$$\sigma_{total}^{ij} = \int \sigma_{ij(\nu)} d\nu = \frac{1}{8\pi c \nu_0^2} \frac{(2J'+1)}{(2J''+1)} A_{ij} \tag{7.3}$$

where c is the speed of light, ν_0 the central frequency of the transition, A_{ij} the Einstein spontaneous emission coefficient; subscripts i and j represent the OH ground state (X) and first excited electronic state (A), respectively. For the $S_{21}(1)$ rotational line, these parameters can be found in reference 184. Figure 7.4-1 presents different lineshapes of the $S_{21}(1)$ line of OH A-X (0-0) band as measured at different plasma heights. Experimental conditions of the ICP were described in the previous section. The spectra were obtained with an average of 100 laser shots, with a scanning rate of 0.0003 nm. OH number density can be obtained through Equations (1) and (2) by integrating over wavenumber (or frequency). The OH number density for the $S_{21}(1)$ line (J''=1.5) is presented in Figure 7.4-2 at different plasma heights. For heights above the load coil

larger than 25 mm, baseline noise was too important to make measurements although OH radicals are still present for a height such as 30 mm ALC.

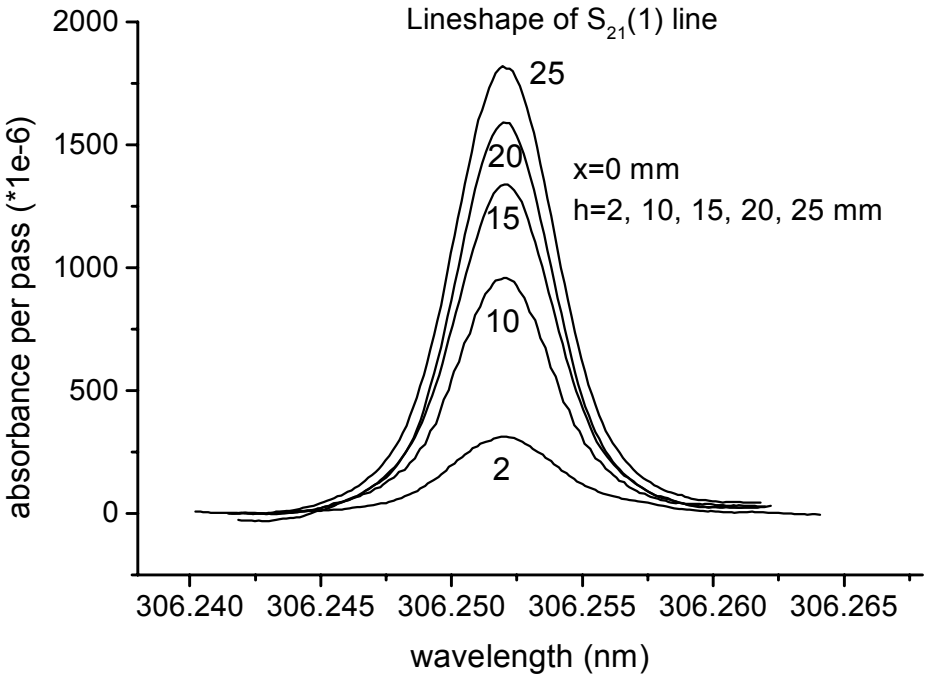

Figure 7.4-1 Measured ringdown spectral lineshapes of the $S_{21}(1)$ rotational line in the OH (0-0) band at different plasma heights. Plasma power = 200 W; x = 0 mm; h (ALC) = 2, 10, 15, 20, and 25 mm from the bottom to the top.

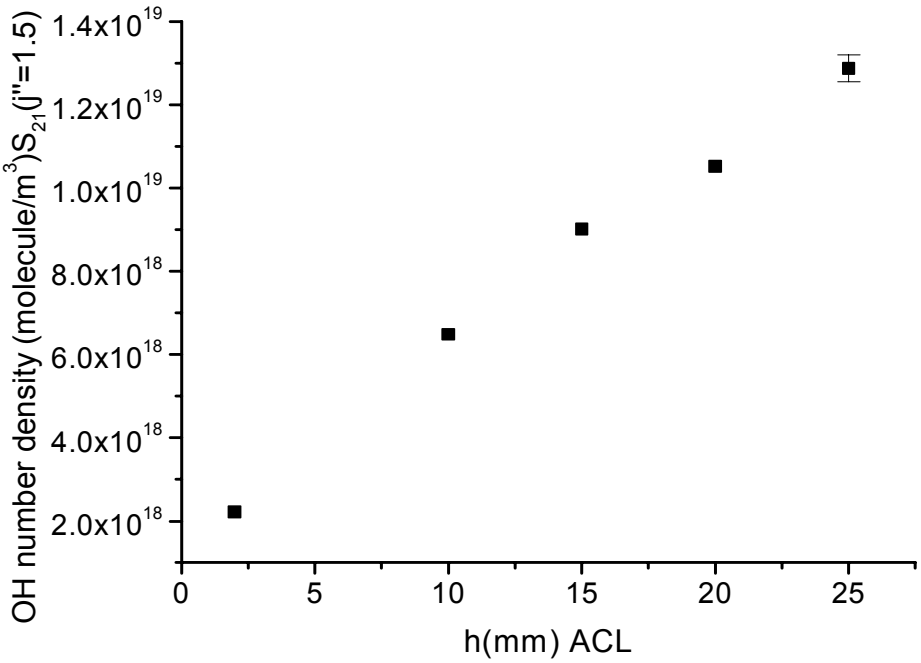

Figure 7.4-2 The spatially-averaged OH density in the $S_{21}(1)$ rotational line vs. plasma height (ALC) at x = 0 mm. Plasma power = 200 W.

7.4.2 Calculation of the total OH density

In the case of LTE approximation, the density of molecular species follows the Boltzmann function distribution. The relationship giving the individual OH vibrational-rotational energy level as a function of the total OH population is given by the following formula:

$$N_{V,J} = N_0 f_B(V,J) = N_0 \frac{1}{Q_e Q_V Q_r} e^{\frac{-E_v(V)}{kT_v}} (2J+1) e^{\frac{-E(J)}{kT_r}} \tag{7.4}$$

where $N_{V,J}$ is the number density of the vibrational-rotational energy level labeled (V,J); N_0 is the total number density; $f_B(V,J)$ is the fraction of the Boltzmann distribution; Q_e, Q_V and Q_r are the electron, vibrational and rotational partition functions, respectively; Q_e

is equal to the electronic degeneracy $g_e=(2-\delta_{0,\Lambda})(2S+1)$ where 2S+1 is the spin multiplicity of the state and $\delta_{0,\Lambda}$ is equal to one for Σ states and zero for all others. For the OH $X^2\Pi$ ground state, $g_e=4$. From the above formula, one can see that a Boltzmann plot will have a slope related to temperature and an intercept at the origin proportional to the total number density. For a Boltzmann plot, it is common to use five or six different emission or absorption lines. In our case, we focused on the measured density population in the single vibrational-rotational transition $S_{21}(1)$. In accordance with the LTE assumption, we set $T_v=T_r=T_k$, where T_k was extracted from the Gaussian lineshape component. The vibrational partition function Q_v in the harmonic oscillator approximation is given by:

$$Q_V = \frac{1}{1-e^{\frac{-1.4388w}{T_V}}} \tag{7.5}$$

where ω is the vibrational frequency ($\omega_{OH}=3737.7941\ cm^{-1}$) and T_v is the vibrational temperature. The rotational partition function is calculated from the energy levels as following:

$$Q_r = \sum_J (2J+1)\cdot e^{\frac{-1.4388w}{T_{rV}}} \tag{7.6}$$

The rotational energy E(J) of each line of the OH A-X (0-0) band is tabulated in reference 184. The rotational energy of the ground state J''=1.5 rotational level of the $S_{21}(1)$ line in the OH (0-0) band is $0.056cm^{-1}$. The rotational partition function was calculated using values of J'' up to 30.5, where $E(30.5)=15716.026\ cm^{-1}$.

7.4.3 Experimental Results

Figure 7.4-3 represents the total OH number density computed with Equation (4). Since no Abel inversion was attempted in this work as it was in others,[223,224,225,226] it is the line-of-sight number density at the center of the plasma which ranges from $1.7x10^{20}$ to $8.5x10^{20}$ m^{-3} for observation heights varying from 2 mm ALC to 25 mm ALC. Hence, the higher in the plasma, the higher the OH number density. This could be due to air entrainment which increases with height in the plasma. The overall density range of our experiment matches with the range found when OH was measured in flames. [210,227]

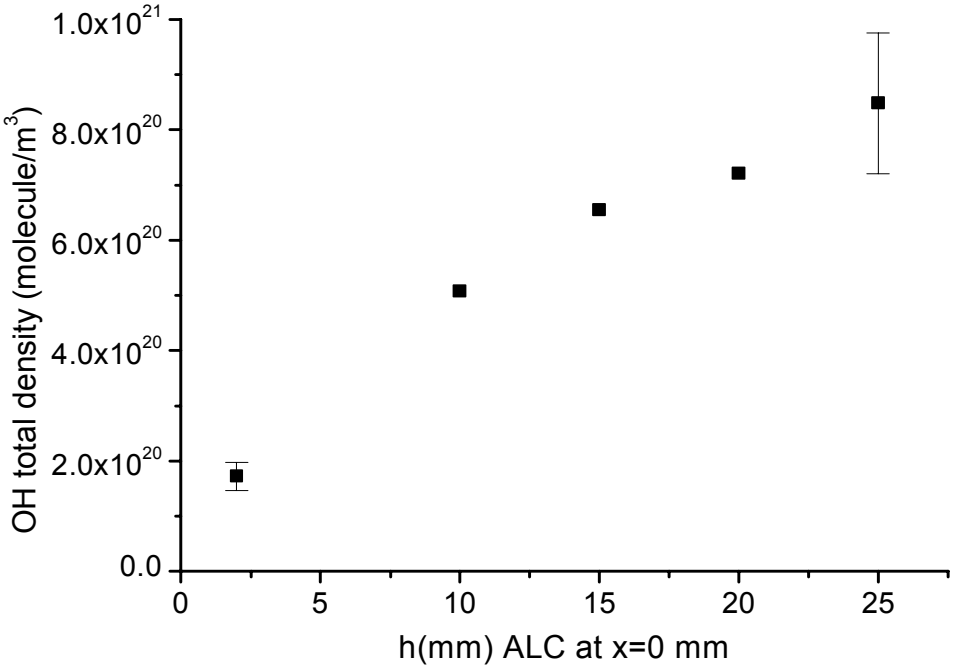

Figure 7.4-3 The spatially-averaged total OH density profile vs. plasma height in the atmospheric pressure argon ICP. Plasma power = 200 W. The maximum and the minimum errors are shown by the error bars.

The OH number density uncertainty is subject to a number of factors. The preponderant factors are (1) temperature; (2) the fact that we are using line-of-sight

integrated absorbance instead of an Abel-inverted radial absorbance profile; and (3) the total absorption cross section calculated from equation (3). It was verified that a 10% uncertainty in temperature generated a 13% variation in the total OH density. For example, a change in temperature from 1800K to 2000K will induce a Boltzmann fraction change from 0.0141 to 0.0124. The difference between line-of sight and radial profile may be as high as 30%. It is estimated that the overall measurement uncertainty in the total OH density is on the order of 30%.

7.4.4 Ab initio calculation of some spectroscopic parameters of OH

7.4.4.1 General Procedure

The computational procedure for the ground state as well as for the excited state are very similar and are of general extent to any molecular computation of spectral parameters. First, we need to optimize the geometry of the molecule by minimizing the energy versus all geometrical parameters of the molecule. In a diatomic molecule, there is only one parameter that is the internuclear distance. That is done by the piece of code listed below.

```
O
H 1 R*
R=1.0
*ACES2(CALC=CCSD, BASIS=AUG-CC-PVTZ, MULT=2, DROPMO=1,
MEM=130000000, REF=UHF, SPHERICAL=ON)
```

The variable R is the internuclear distance in Angstroms, with initial guess of 1.0. The star indicates to the Aces II (University of Florida, Quantum Theory Project) interpreter which parameters to optimize versus energy. The method of calculation is Coupled Cluster singles and doubles (CCSD) method. The basis chosen is aug-cc-PVTZ

(correlation consistent polarized valence triple-zeta augmented basis). Because of the smallness of the molecule, we could afford using a basis that is computationally expensive for better accuracy. The program also requires the spin multiplicity of the state (2 for the hydroxyl radical). We also instruct Aces II to drop the first orbital, the memory size to allocate, to use Unrestricted Hartree Fock, and to use Spherical Harmonics instead of Cartesian harmonics. This piece of code gives us the bond length for the ground state (listed in Table 7.4-1 below).

7.4.4.2 Results

The results of the computations done with XAces 2 are listed in Table 7.4-1. As one can see, for the ground state, the computed values are closer than 1% to the values found in the literature.[228] For the excited state however, the vibrational frequency is off by 30%, while the state energy and internuclear distance are in good agreement.

Table 7.4-1. Comparison of literature values and calculation with Aces II for OH ground and first excited state. Re is the equilibrium internuclear distance; Te is the energy of the bottom of the electronic potential well.

	R_e (Å) ($X\ ^2\Pi$)	R_e (Å) ($A\ ^2\Sigma+$)	T_e (cm^{-1}) ($A\ ^2\Sigma^+$)	ω_e (cm^{-1}) ($X\ ^2\Pi$)	ω_e (cm^{-1}) ($A\ ^2\Sigma^+$)
Literature	0.96966	1.0121	32684.1	3737.76	3178.8
Aces II	0.97067	1.0099	32847.0	3756.64	2335.3

7.5 Concluding remarks

CRDS was applied to make line-of-sight measurements of OH radicals in a low flow, low-power, atmospheric-pressure argon inductively coupled plasma. The estimated population of the $S_{21}(1)$ line was calculated from the OH absorption spectrum. The line-of-sight-averaged total OH number density profile versus plasma height was plotted and

total OH density was estimated to be in the range $1.7x20^{20}$-$8.5x10^{20}$ m^{-3}, the highest density being in the tail of the plasma. Kinetic temperatures as a function of height were deduced from the Gaussian lineshape component. Temperatures were found in the range of 1800-2000K with an uncertainty of 10%. Comparison of the measured OH emission spectrum with a simulation enabled a test of the local thermal equilibrium assumption.

CRDS has once again been proven to be robust enough and sufficiently versatile to be used for plasma diagnostics to measure gas temperatures and investigate the thermodynamic properties of atmospheric-pressure plasmas and hopefully can also be applied to combustion systems.

CHAPTER VIII

CONCLUSION

In the present framework, Cavity Ringdown Spectroscopy (CRDS) has been successively coupled with an inductively coupled plasma (ICP) for analytical as well as plasma diagnostics purposes. More precisely, CRDS has been used as an atomic analytical tool for mercury and its sensitivity was compared to laser-induced fluorescence (LIF) in Chapter IV. Furthermore, CRDS was successively used to perform analytical mercury and lead measurements with a graphite furnace atomizer and ten-fold better figures of merit were demonstrated compared with a standard-absorption commercially available instrument with no use of matrix modifiers. CRDS was also used to record isotopically resolved spectra of uranium in the ICP (Chapter V) for ions as well as for atoms, and limits of detection were compared with available LIF data. Plasma diagnostics, such as temperature evaluation and electron density estimation by absorption lineshape measurements were done on atomic lead (Chapter VI). Abel inverted absorption profile across the plasma was determined for absolute ground-state lead density measurements. Spectra on OH were recorded and used for integrated line-of-sight density estimation of a particular rotational level. Kinetic temperature (by lineshape

broadening) and rotational temperature (by spectral simulation) were estimated to be the same, satisfying the condition for local thermal equilibrium of the plasma (Chapter VII).

It is important to emphasize that this work is the first extensive absorption study on the ICP. In the past, atomic species have been predominantly studied in the ICP with emission and with LIF and their limits of detection are well documented. Previously, there was only one publication reporting spectrometric measurements of sodium ground state atoms in the ICP. Furthermore, our work is the first to date to investigate the ICP used under such low-power conditions which turned out to be, as we demonstrated, a very good atom reservoir for lead and mercury. As the reflectivity of the mirrors will increase in the ultraviolet with improvement of coating techniques, it is expected that aqueous limits of detection for these elements will be below one part per trillion. This project was also an opportunity to design a new, low-flow ICP torch with a wider central channel and a lower outer shield. More recently, a research group has used the ringdown technique to characterize a N_2 low pressure ICP.[229]

Since its early developments, cavity ringdown, has been done with continuous-wave diode lasers, and has been proven to be a very powerful, high-resolution spectroscopic technique that enables absolute absorbance measurements. For example, use of a diode laser coupled with an ICP could provide a small, compact, portable uranium isotopic spectrometer that would easily work in the sub-parts per million levels, as needed in radioactive waste processing facilities. Use of a narrow linewidth laser system would also enable to resolve mercury isotopes.

Compared to LIF, a technique capable of virtually doing single atom detection, CRDS has its advantages and limitations. Unlike LIF, it provides absolute measurements.

Conversely, ringdown is sensitive to light scattering while LIF is not if appropriate excitation and emission wavelengths are chosen. This could be a problem in environments where soot is present, such as combustion environments

APPENDIX

Table A-1. Parameter variation with height derived from lineshape fitting.

h (mm)	w_G (pm)	w_L (pm)	$w_{\exp}$ (pm)	a	T (K)	Pb (ng/mL)
2	0.74	0.84	2.39	0.9	2755	100
4	0.72	0.94	2.50	1.1	2608	100
6	0.75	0.76	2.24	0.8	2830	100
8	0.74	0.88	2.40	1.0	2755	100
10	0.71	0.73	2.16	0.9	2536	100
12	0.78	0.78	2.30	0.8	3061	200
14	0.72	0.73	2.23	0.8	2608	200
18	0.71	0.72	2.12	0.8	2536	200
22	0.74	0.67	2.10	0.8	2755	200
30	0.61	0.45	1.89	0.6	1872	500

Table A-2. Parameter variation with lateral derived from lineshape fitting.

r (mm)	w_G (pm)	w_L (pm)	$w_{\exp}$ (pm)	a	T (K)	σ_{pq} from Voigt (10^{-13} cm^{-3})	Pb (ng/mL)
0	0.68	0.94	2.43	1.2	2326	6.48	100
0.5	0.82	0.79	2.39	0.8	3383	8.40	100
1	0.88	0.67	2.31	0.6	3896	10.2	100
1.5	0.89	0.63	2.27	0.6	3985	10.9	100
2	0.79	0.57	2.03	0.6	3140	11.5	200
2.5	0.66	0.60	1.87	0.8	2191	10.0	200
3	0.65	0.95	2.45	1.2	2126	6.27	200
3.5	0.56	0.81	2.05	1.2	1578	6.80	200
4	0.56	0.75	1.98	1.1	1578	7.34	500

Table A-3. Comparison of detection limit (ng/mL) from ICP-CRDS with those from various methods.

Element	Wavelength (nm)	Method			
		ICP-ES	ICP-LIF	ICP-MS	ICP-CRD
Pb	283.3	140	1	0.2	0.3

REFERENCES

1 Hodges, J.T., Looney, J.P., van Zee, R.D., Appl. Opt., 1996, 257, 487

2 Slanger, T.G., Huestis, D.L., Cosby, P.C., Naus, H., and Meijer, G.J., Chem. Phys., 1996, 105, 9393

3 Engeln, R. and Meijer, G., Rev. Sci. Instrum., 1996, 67, 2708

4 O'Keefe, A., Lee, O., American Laboratory, 1989, December, 19

5 Jongma, R.T., Boogarts, M.G.H., Holleman, I., Meijer, G., J. Mol. Spectrosc., 1994, 165, 303

6 Diau, E.W., Yu, T., Wagner, M.A.G., Lin, M.C., J. Phys. Chem., 1994, 98, 4034

7 Jongma, R.T., Boogaarts, M.G.H., Holleman, I., Miejer G., Rev. Sci. Instrum., 1995, 66, 2821

8 Scherer, J.J., Voelkel, D., Rakestraw, D.J., Paul, J.B., Collier, C.P., Saykally, R.J., O'Keefe, A., Chem. Phys. Lett., 1995, 245, 273

9 Yu, T., Lin, M.C., J. Phys. Chem., 1994, 98, 9697

10 Spanjaars, J.J.L., ter Meulen, J.J., Meijer, G., J. Chem. Phys., 1997, 107, 2242

11 Herbelin, J.M., McKay, J.A., Kwok, M.A., Uenten, R.H., Urevig, D.S., Spencer, D.J., Bernard, D.J., Appl. Opt. 1980, 19, 144

12 Anderson, D.Z., Frisch, J.C., Masser C.S., Appl. Opt., 1984, 23, 1238

13 Hobbs, P.C.D.; Appl. Opt. 1997, 36, 903.

14 Allen, M.G., et al. Appl .Opt. 1995, 34, 3240.

15 Cherrier, P.P. & Reid, J.; Nucl. Inst. Meth. Phy. Res. 1987, A257, 412.

16 He, Y.; Orr, B.J. Applied Physics B (Lasers and Optics), vol.B75, no.2-3, Sept. 2002. p. 267-80

17 Orr, B.J.; He, Y. *In:* Technical Digest. Summaries of papers presented at the Conference on Lasers and Electro-Optics. Conference Edition (IEEE Cat. No.02CH37337). Washington, DC, USA: Opt. Soc. America, 2002. p. 627 vol.1

18 Yabai He; Orr, B.J. Chemical Physics Letters, vol.335, no.3-4, 23 Feb. 2001. p. 215-20

19 Levenson, M.D.; Paldus, B.A.; Spence, T.G.; Harb, C.C. Optics Letters, vol.25, no.12, 15 June 2000. p. 920-2

20 Jun Ye; Hall, J.L. Physical Review A (Atomic, Molecular, and Optical Physics), vol.61, no.6, June 2000.

21 Jun Ye; Hall, J.L. *In:* Quantum Electronics and Laser Science Conference (QELS 2000). Technical Digest. Postconference Edition. TOPS Vol.40 (IEEE Cat. No.00CH37089). Salem, MA, USA: Opt. Soc. America, 2000. p. 181-2

22 Seiser, N. ; Robie, D.C.; Chemical Physics Letters , vol.282, no.3-4, 16 Jan. 1998. p. 263-7.

23 Engeln, R. ; Berden, G.; van den Berg, E.; Meijer, G.; Journal of Chemical Physics , vol.107, no.12, 22 Sept. 1997. p. 4458-67.

24 Berden, G. ; Engeln, R.; Christianen, P.C.M.; Maan, J.C.; Meijer, G.; Physical Review A (Atomic, Molecular, and Optical Physics) , vol.58, no.4, Oct. 1998. p. 3114-23.

25 Naus, H. ; Ubachs, W.; Journal of Molecular Spectroscopy , vol.193, no.2, Feb. 1999. p. 442-5.

26 Naus, H. ; Ubachs, W.; Applied Optics , vol.38, no.15, 20 May 1999. p. 3423-8.

27 Sneep, M. ; Ubachs, W.; Journal of Quantitative Spectroscopy and Radiative Transfer , vol.78, no.2, 1 May 2003. p. 171-8.

28 Newman, S.M. ; Lane, I.C.; Orr-Ewing, A.J.; Newnham, D.A.; Ballard, J.; Journal of Chemical Physics , vol.110, no.22, 8 June 1999. p. 10749-57.

29 Miller, H.C. ; McCord, J.E.; Choy, J.; Hager, G.D.; Journal of Quantitative Spectroscopy and Radiative Transfer , vol.69, no.3, 1 May 2001. p. 305-25.

30 O'Keefe, A. ; Scherer, J.J.; Cooksy, A.L.; Sheeks, R.; Heath, J.; Saykally, R.J.; Chemical Physics Letters , vol.172, no.3-4, Sept. 1990. p. 214-18.

31 Romanini, D. ; Lehmann, K.K.; Journal of Chemical Physics , vol.99, no.9, 1 Nov. 1993. p. 6287-301.

32 Romanini, D. ; Lehmann, K.K.; Journal of Chemical Physics , vol.102, no.2, 8 Jan. 1995. p. 633-42.

33 Romanini, D. ; Lehmann, K.K.; Journal of Chemical Physics , vol.105, no.1, 1 July 1996. p. 68-80.

34 Zalicki, P. ; Ma, Y.; Zare, R.N.; Wahl, E.H.; Owano, T.G.; Kruger, C.H. ; Applied Physics Letters , vol.67, no.1, 3 July 1995. p. 144-6.

35 Pearson, J. ; Orr-Ewing, A.J.; Ashfold, M.N.R.; Dixon, R.N.; Journal of Chemical Physics , vol.106, no.14, 8 April 1997. p. 5850-73.

36 Kotterer, M. ; Maier, J.P.; Chemical Physics Letters , vol.266, no.3-4, 28 Feb. 1997. p. 342-6.

37 Linnarz, H. ; Motylewski, T.; Vaizert, O.; Maier, J.P.; Apponi, A.J.; McCarthy, M.C.; Gottlieb, C.A.; Thaddeus, P.; Journal of Molecular Spectroscopy , vol.197, no.1, Sept. 1999. p. 1-11.

38 Motylewski, T. ; Linnartz, H.; Review of Scientific Instruments , vol.70, no.2, Feb. 1999. p. 1305-12.

39 Ball, C.D. ; McCarthy, M.C.; Thaddeus, P.; Astrophysical Journal, Letters , vol.523, no.1, pt.2, 20 Sept. 1999. p. L89-91.

40 Ball, C.D. ; McCarthy, M.C.; Thaddeus, P.; Journal of Chemical Physics , vol.112, no.23, 15 June 2000. p. 10149-55.

41 Provencal, R.A. ; Paul, J.B.; Roth, K.; Chap, C.; Casaes, R.N.; Saykally, R.J.; Tschumper, G.S.; Schaefer, H.F., III; Journal of Chemical Physics , vol.110, no.9, 1 March 1999. p. 4258-67.

42 Tschumper, G.S. ; Gonzales, J.M.; Schaefer, H.F., III; Journal of Chemical Physics , vol.111, no.7, 15 Aug. 1999. p. 3027-34.

43 Shucheng Xu ; Yonglin Liu; Guohe Sha; Cuohao Zhang; Jinchun Xie; Journal of Physical Chemistry A , vol.104, no.38, 28 Sept. 2000. p. 8671-6.

44 Bucher, C.R. ; Lehmann, K.K.; Plusquellic, D.F.; Fraser, G.T.; Applied Optics , vol.39, no.18, 20 June 2000. p. 3154-64.

45 Abrams, M.L. ; Valeev, E.F.; Sherrill, C.D.; Crawford, T.D.; Journal of Physical Chemistry A , vol.106, no.11, 21 March 2002. p. 2671-5.

46 Pushkarsky, M.B. ; Zalyubovsky, S.J.; Miller, T.A.; Journal of Chemical Physics , vol.112, no.24, 22 June 2000. p. 10695-8.

47 Lehr, L. ; Hering, P.; Applied Physics B (Lasers and Optics) , vol.B65, no.4-5, Oct. 1997. p. 595-600.

48 Lehr, L. ; Hering, P.; IEEE Journal of Quantum Electronics , vol.33, no.9, Sept. 1997. p. 1465-73.

49 Wheeler, M.D. ; Newman, S.M.; Orr-Ewing, A.J.; Journal of Chemical Physics , vol.108, no.16, 22 April 1998. p. 6594-605.

50 Howie, W.H. ; Lane, I.C.; Orr-Ewing, A.J.; Journal of Chemical Physics , vol.113, no.17, 1 Nov. 2000. p. 7237-51.

51 Muller, T. ; Vaccaro, P.H.; Perez-Bernal, F.; Iachello, F.; Chemical Physics Letters , vol.329, no.3-4, 20 Oct. 2000. p. 271-82.

52 Labazan, I. ; Milosevic, S. ; AIP Conference Proceedings , no.559, 2001. p. 307-9.

53 Labazan, I. ; Milosevic, S.; Chemical Physics Letters , vol.352, no.3-4, 30 Jan. 2002. p. 226-33.

54 Zalyubovsky, S.J. ; Dongbing Wang; Miller, T.A.; Chemical Physics Letters , vol.335, no.3-4, 23 Feb. 2001. p. 298-304.

55 Thaddeus, P. ; McCarthy, M.C.; Spectrochimica Acta, Part A (Molecular and Biomolecular Spectroscopy) , vol.57A, no.4, 15 March 2001. p. 757-74.

56 Cormier, J.G. ; Ciurylo, R.; Drummond, J.R.; Journal of Chemical Physics , vol.116, no.3, 15 Jan. 2002. p. 1030-4.

57 Samura, K. ; Hashimoto, S.; Kawasaki, M.; Hayashida, A.; Kagi, E.; Ishiwata, T.; Matsumi, Y.; Applied Optics , vol.41, no.12, 20 April 2002. p. 2349-54.

58 Hippler, M. ; Quack, M.; Journal of Chemical Physics , vol.116, no.14, 8 April 2002. p. 6045-55.

59 Robinson, A.G. ; Winter, P.R.; Zwier, T.S.; Journal of Chemical Physics , vol.116, no.18, 8 May 2002. p. 7918-25.

60 Ashworth, S.H. ; Allan, B.J.; Plane, J.M.C.; Geophysical Research Letters , vol.29, no.10, 15 May 2002. p. 65-1-4.

61 Dahnke, H. ; von Basum, G.; Kleinermanns, K.; Hering, P.; Murtz, M.; Applied Physics B (Lasers and Optics) , vol.B75, no.2-3, Sept. 2002. p. 311-16.

62 Atkinson, D.B. ; Spillman, J.L.; Journal of Physical Chemistry A , vol.106, no.38, 26 Sept. 2002. p. 8891-902.

63 Ruth, A.A. ; Gash, E.W.; Staak, M.; Fiedler, S.E.; Physical Chemistry Chemical Physics , vol.4, no.21, 1 Nov. 2002. p. 5217-20.

64 Mazurenka, M.I. ; Fawcett, B.L.; Elks, J.M.F.; Shallcross, D.E.; Orr-Ewing, A.J.; Chemical Physics Letters , vol.367, no.1-2, 2 Jan. 2003. p. 1-9.

65 Nizamov, B. ; Dagdigian, P.J.; Journal of Physical Chemistry A , vol.107, no.13, 3 April 2003. p. 2256-63.

66 Ito, F. ; Nakanaga, T.; Journal of Chemical Physics , vol.119, no.11, 15 Sept. 2003. p. 5527-33.

67 Proceedings of 8th International Symposium on Laser-Aided Plasma Diagnostics. Doorwerth, Netherlands, 22-26 Sept. 1997

68 Spence, T.G. ; Paldus, B.A.; Wahl, E.H.; Aderhold, D.D.; Xie, J.C.; Owano, T.G.; Laux, C.O.; Kruger, C.H.; Zare, R.N., 25th Anniversary, IEEE Conference Record - Abstracts. 1998 IEEE International Conference on Plasma Science (Cat. No.98CH36221). New York, NY, USA: IEEE, 1998. p. 122.

69 Sadeghi, N. ; Booth, J.-P.; Campargue, A.; Romanini, D., 19th Summer School and International Symposium on the Physics of Ionized Gases. 19th SPIG. Contributed Papers and Abstracts of Invited Lectures, Topical Invited Lectures and Progress Reports. Belgrade, Yugoslavia: Univ. Belgrade, 1998. p. 313.

70 Campargue, A. ; Romanini, D.; Sadeghi, N., Journal of Physics D (Applied Physics) , vol.31, no.10, 21 May 1998. p. 1168-75.

71 Grangeon, F. ; Monard, C.; Dorier, J.-L.; Howling, A.A.; Hollenstein, Ch.; Romanini, D.; Sadeghi, N., Frontiers in Low Temperature Plasma Diagnostics III. Book of Papers. Lausanne, Switzerland: Ecole Polytechnique Federale de Lausanne, Feb. 1999. p. 237-40.

72 Grangeon, F. ; Monard, C.; Dorier, J.-L.; Howling, A.A.; Hollenstein, Ch.; Romanini, D.; Sadeghl, N., Plasma Sources, Science and Technology , vol.8, no.3, Aug. 1999. p. 448-56.

73 Boogaarts, M.G.H. ; Smets, A.H.M.; van de Sanden, M.C.M.; Schram, D.C., Frontiers in Low Temperature Plasma Diagnostics III. Book of Papers. Lausanne, Switzerland: Ecole Polytechnique Federale de Lausanne, Feb. 1999. p. 215-18.

74 Booth, J.P. ; Romanini, D.; Katchanov, A.; Biennier, L.; Cunge, G., Frontiers in Low Temperature Plasma Diagnostics III. Book of Papers. Lausanne, Switzerland: Ecole Polytechnique Federale de Lausanne, Feb. 1999. p. 219-22.

75 Booth, J.P. ; Cunge, G.; Biennier, L.; Romanini, D.; Kachanov, A., Chemical Physics Letters , vol.317, no.6, 11 Feb. 2000. p. 631-6.

76 Engeln, R. ; Letourneur, K.G.Y.; Boogaarts, M.G.H.; van de Sanden, M.C.M.; Schram, D.C., Chemical Physics Letters , vol.310, no.5-6, 10 Sept.

77 Linnartz, H. ; Vaizert, O.; Motylewski, T.; Maier, J.P.; Journal of Chemical Physics , vol.112, no.22, 8 June 2000. p. 9777-9.

78 Boogaarts, M.G.H. ; Bocker, P.J.; Kessels, W.M.; Schram, D.C.; Van De Sanden, M.C.M.; Chemical Physics Letters , vol.326, no.5-6, 25 Aug. 2000. p. 400-6.

79 Hemerik, M.M. ; Kroesen, G.M.W.; Proceedings of Frontiers in Low Temperature Plasma Diagnostics IV. Eindhoven, Netherlands: Eindhoven Univ. Technol, 2001. p. 83-6.

80 Orr-Ewing, A.J.; Proceedings of Workshop on Frontiers in Low Temperature Plasma Diagnostics. Limburg, Netherlands, 25-29 March 2001

81 Hoefnagels, J.P.M. ; Stevens, A.A.E.; Kessels, W.M.M.; van de Sanden, M.C.M.; Proceedings of Frontiers in Low Temperature Plasma Diagnostics IV. Eindhoven, Netherlands: Eindhoven Univ. Technol, 2001. p. 205-8.

82 Macko, P. ; Romanini, D.; Sadeghi, N.; Proceedings of Frontiers in Low Temperature Plasma Diagnostics IV. Eindhoven, Netherlands: Eindhoven Univ. Technol, 2001. p. 223-6.

83 Yalin, A.P. ; Lommatzsch, U.; Zare, R.N.; Laux, C.O.; Kruger, C.H.; IEEE Conference Record - Abstracts. PPPS-2001 Pulsed Power Plasma Science 2001. 28th IEEE International Conference on Plasma Science and 13th IEEE International Pulsed Power Conference (Cat. No.01CH37255). Piscataway, NJ, USA: IEEE, 2001. p. 449.

84 Yalin, A.P. ; Zare, R.N.; Laux, C.O.; Kruger, C.H.; Applied Physics Letters , vol.81, no.8, 19 Aug. 2002. p. 1408-10.

85 Yalin, A.P. ; Laux, C.O.; Kruger, C.H.; Zare, R.N.; Plasma Sources, Science and Technology , vol.11, no.3, Aug. 2002. p. 248-53.

86 Hoefnagels, J.P.M. ; Stevens, A.A.E.; Boogaarts, M.G.H.; Kessels, W.M.M.; van de Sanden, M.C.M.; Chemical Physics Letters , vol.360, no.1-2, 3 July 2002. p. 189-93.

87 Kotterer, M. ; Conceicao, J.; Maier, J.P.; Chemical Physics Letters , vol.259, no.1-2, 30 Aug. 1996. p. 233-6.

88 Macko, P. ; Cunge, G.; Sadeghi, N.; Journal of Physics D (Applied Physics) , vol.34, no.12, 21 June 2001. p. 1807-11.

89 Kessels, W.M.M. ; Hoefnagels, J.P.M.; Boogaarts, M.G.H.; Schram, D.C.; van de Sanden, M.C.M.; Journal of Applied Physics , vol.89, no.4, 15 Feb. 2001. p. 2065-73.

90 Kessels, W.M.M. ; Leroux, A.; Boogaarts, M.G.H.; Hoefnagels, J.P.M.; van de Sanden, M.C.M.; Schram, D.C.; Journal of Vacuum Science & Technology A (Vacuum, Surfaces, and Films) , vol.19, no.2, March-April 2001. p. 467-76.

91 Kessels, W.M.M. ; Boogaarts, M.G.H.; Hoefnagels, J.P.M.; Schram, D.C.; van de Sanden, M.C.M.; Journal of Vacuum Science & Technology A (Vacuum, Surfaces, and Films) , vol.19, no.3, May 2001. p. 1027-9.

92 van Beek, M.C. ; ter Meulen, J.J.; Chemical Physics Letters , vol.337, no.4-6, 6 April 2001. p. 237-42.

93 Schwabedissen, A. ; Brockhaus, A.; Georg, A.; Engemann, J.; Journal of Physics D (Applied Physics) , vol.34, no.7, 7 April 2001. p. 1116-21.

94 Creatore, M. ; van Hest, M.F.A.M.; Benedikt, J.; van de Sanden, M.C.M.; Amorphous and Heterogeneous Silicon-Based Films - 2002. Symposium (Materials Research Society Symposium Proceedings Vol.715). Warrendale, PA, USA: Mater. Res. Soc, 2002. p. 101-7.

95 Scherer, J.J. ; Paul, J.B.; Collier, C.P.; Saykally, R.J.; Journal of Chemical Physics , vol.102, no.13, 1 April 1995. p. 5190-9.

96 Scherer, J.J. ; Paul, J.B.; Collier, C.P.; Saykally, R.J.; Journal of Chemical Physics , vol.103, no.1, 1 July 1995. p. 113-20.

97 Scherer, J.J. ; Paul, J.B.; Collier, C.P.; O'Keefe, A.; Saykally, R.J.; Journal of Chemical Physics , vol.103, no.21, 1 Dec. 1995. p. 9187-92.

98 Vaizert, O. ; Motylewski, T.; Wyss, M.; Riaplov, E.; Linnartz, H.; Maier, J.P.; Journal of Chemical Physics , vol.114, no.18, 8 May 2001. p. 7918-22.

99 Linnartz, H. ; Vaizert, O.; Cias, P.; Gruter, L.; Maier, J.P.; Chemical Physics Letters , vol.345, no.1-2, 7 Sept. 2001. p. 89-92.

100 Cias, P. ; Vaizert, O.; Denisov, A.; Mes, J.; Linnartz, H.; Maier, J.P.; Journal of Physical Chemistry A , vol.106, no.42, 24 Oct. 2002. p. 9890-2.

101 Vaizert, O. ; Furrer, P.; Cias, P.; Linnartz, H.; Maier, J.P.; Journal of Molecular Spectroscopy , vol.214, no.1, July 2002. p. 94-5.

102 Pfluger, D. ; Motylewski, T.; Linnartz, H.; Sinclair, W.E.; Maier, J.P.; Chemical Physics Letters , vol.329, no.1-2, 13 Oct. 2000. p. 29-35.

103 Macko, P. ; Plasil, R.; Kudrna, P.; Hlavenka, P.; Poterya, V.; Pysanenko, A.; Bano, G.; Glosik, J.; Czechoslovak Journal of Physics , vol.52, suppl.D [CD-ROM], 2002. p. D695-704.

104 Czyiewski, A. ; Ernst, K.; Franssen, G.; Karasinski, G.; Kmieciak, M.; Lange, H.; Skubiszak, W.; Stacewicz, T.; Chemical Physics Letters , vol.357, no.5-6, 17 May 2002. p. 477-82.

105 Benedikt, J. ; Letourneur, K.G.Y.; Wisse, M.; Schram, D.C.; van de Sanden, M.C.M.; Diamond and Related Materials , vol.11, no.3-6, March-June 2002. p. 989-93.

106 John, P. ; Rabeau, J.R.; Wilson, J.I.B.; Diamond and Related Materials , vol.11, no.3-6, March-June 2002. p. 608-11.

107 Wills, J.B. ; Smith, J.A.; Boxford, W.E.; Elks, J.M.F.; Ashfold, M.N.R.; Orr-Ewing, A.J.; Journal of Applied Physics , vol.92, no.8, 15 Oct. 2002. p. 4213-22.

108 Quandt, E. ; Kraemer, I.; Dobele, H.F. Europhysics Letters , vol.45, no.1, 1 Jan. 1999. p. 32-7.

109 Chuji Wang ; Mazzotti, F.J.; Miller, G.P.; Winstead, C.B.; Applied Spectroscopy , vol.56, no.3, March 2002. p. 386-97.

110 Meijer, G. ; Boogaarts, M.G.H.; Jongma, R.T.; Parker, D.H.; Wodtke, A.M.; Chemical Physics Letters , vol.217, no.1-2, 7 Jan. 1994. p. 112-16.

111 Cheskis, S. ; Derzy, I.; Lozovsky, V.A.; Kachanov, A.; Stoeckel, F.; Proceedings of the SPIE - The International Society for Optical Engineering , vol.3172, 1997. p. 616-24.

112 Cheskis, S. ; Derzy, I.; Lozovsky, V.A.; Kachanov, A.; Romanini, D.; Applied Physics B (Lasers and Optics) , vol.B66, no.3, March 1998. p. 377-81.

113 Lozovsky, V.A. ; Derzy, I.; Cheskis, S.; Chemical Physics Letters , vol.284, no.5-6, 6 March 1998. p. 407-11.

114 Mercier, X. ; Therssen, E.; Pauwels, J.F.; Desgroux, P.; Chemical Physics Letters , vol.299, no.1, 1 Jan. 1999. p. 75-83.

115 Mercier, X. ; Jamette, P.; Pauwels, J.F.; Desgroux, P.; Chemical Physics Letters , vol.305, no.5-6, 28 May 1999. p. 334-42.

116 Derzy, I. ; Lozovsky, V.A.; Cheskis, S.; Chemical Physics Letters , vol.306, no.5-6, 18 June 1999. p. 319-24.

117 Stolk, R.L. ; ter Meulen, J.J.; Diamond and Related Materials , vol.8, no.7, July 1999. p. 1251-5.

118 Luque, J. ; Jeffries, J.B.; Smith, G.P.; Crosley, D.R.; Applied Physics B (Lasers and Optics) , vol.B73, no.7, Nov. 2001. p. 731-8.

119 Luque, J. ; Jeffries, J.B.; Smith, G.P.; Crosley, D.R.; Chemical Physics Letters, vol.346, no.3-4, 5 Oct. 2001. p. 209-16.

120 Xie, J. ; Paldus, B.A.; Wahl, E.H.; Martin, J.; Owano, T.G.; Kruger, C.H.; Harris, J.S.; Zare, R.N.; Chemical Physics Letters , vol.284, no.5-6, 6 March 1998. p. 387-95.

121 Scherer, J.J. ; Rakestraw, D.J.; Chemical Physics Letters , vol.265, no.1-2, 31 Jan. 1997. p. 169-76.

122 Scherer, J.J. ; Aniolek, K.W.; Cernansky, N.P.; Rakestraw, D.J.; Journal of Chemical Physics , vol.107, no.16, 22 Oct. 1997. p. 6196-203.

123 Scherer, J.J. ; Voelkel, D.; Rakestraw, D.J.; Applied Physics B (Lasers and Optics) , vol.B64, no.6, June 1997. p. 699-705.

124 McIlroy, A.; Chemical Physics Letters , vol.296, no.1-2, 30 Oct. 1998. p. 151-8.

125 Mercier, X. ; Pillier, L.; Pauwels, J.-F.; Desgroux, P.; Comptes Rendus de l'Academie des Sciences, Serie IV (Physique, Astrophysique) , vol.2, no.7, Sept. 2001. p. 965-72.

126 Stolk, R.L. ; ter Meulen, J.J.; Journal of Chemical Physics , vol.117, no.18, 8 Nov. 2002. p. 8281-91.

127 Emig, M. ; Billmers, R.I.; Owens, K.G.; Cernansky, N.P.; Miller, D.L.; Narducci, F.A.; Applied Spectroscopy , vol.56, no.7, July 2002. p. 863-8.

128 Pillier, L. ; Moreau, C.; Mercier, X.; Pauwels, J.F.; Desgroux, P.; Applied Physics B (Lasers and Optics) , vol.B74, no.4-5, April 2002. p. 427-34.

129 Staicu, A. ; Stolk, R.L.; ter Meulen, J.J.; Journal of Applied Physics , vol.91, no.3, 1 Feb. 2002. p. 969-74.

130 Spuler, S. ; Linne, M.; Applied Optics , vol.41, no.15, 20 May 2002. p. 2858-68.

131 Wen-Bin Yan ; Krusen, C.; Dudek, J.; Lehmann, K.; Rabinowitz, P.; 13th Annual IEEE/SEMI Advanced Semiconductor Manufacturing Conference. Advancing the Science and Technology of Semiconductor Manufacturing. ASMC 2002 (Cat. No.02CH37259). Piscataway, NJ, USA: IEEE, 2002. p. 319-23.

132 Wen-Bin Yan; Proceedings of the SPIE - The International Society for Optical Engineering , vol.4648, 2002. p. 156-64.

133 Stry, S. ; Hering, P.; Murtz, M.; Applied Physics B (Lasers and Optics) , vol.B75, no.2-3, Sept. 2002. p. 297-303.

134 Jongma, R.T. ; Boogaarts, M.G.H.; Holleman, I.; Meijer, G.; Review of Scientific Instruments , vol.66, no.4, April 1995. p. 2821-8.

135 Romanini, D. ; Kachanov, A.A.; Sadeghi, N.; Stoeckel, F.; Chemical Physics Letters , vol.264, no.3-4, 10 Jan. 1997. p. 316-22.

136 Yong Shim Yoo ; Jae Won Hahn; Jae Wan Kim; Jae Yong Lee; Hai-Woong Lee; Hankook Kwanghak Hoeji , vol.9, no.4, Aug. 1998. p. 240-4.

137 Stewart, G. ; Atherton, K.; Culshaw, B.; 14th International Con on Optical Fiber Sensors. Confrence Proceedings (SPIE Vol.4185). Bellingham, WA. USA & Florence, Italy: SPIE & CNR, 2000. p. 448-51.

138 Cormier, J.G. ; Hodges, J.T.; Drummond, J.R.; AIP Conference Proceedings , no.645, 2002. p. 401-12.

139 Gopalsami, N. ; Raptis, A.C.; Meier, J.; Review of Scientific Instruments , vol.73, no.2, Feb. 2002. p. 259-62.

140 Czyzewski, A. ; Ernst, K.; Karasinski, G.; Lange, H.; Rairoux, P.; Skubiszak, W.; Stacewicz, T.; Acta Physica Polonica B , vol.33, no.8, Aug. 2002. p. 2255-65.

141 Brown, S.S. ; Stark, H.; Ravishankara, A.R.; Applied Physics B (Lasers and Optics) , vol.B75, no.2-3, Sept. 2002. p. 173-82.

142 Todd, M.W. ; Provencal, R.A.; Owano, T.G.; Paldus, B.A.; Kachanov, A.; Vodopyanov, K.L.; Hunter, M.; Coy, S.L.; Steinfeld, J.I.; Arnold, J.T.; Applied Physics B (Lasers and Optics) , vol.B75, no.2-3, Sept. 2002. p. 367-76.

143 W. L. Clevenger, B. W. Smith, and J. D. Wine Fordner; Critical reviews in analytical chemistry, Vol. 27, no. 1, (1997); pp. 1-12

144 Fengxiang H. Han. Amos Banin, Yi SU, David L. Monts, M. John Plodinec, William L. Kingery, Glover E. Triplett; Naturwissenschaften (2002) 89; pp. 497-504

145 Jongman, Rienk T.; Boogaarts, Maarten G.H.; Holleman, Iwan; Meijer, Gerard; Review of Scientific Instruments, Apr95, Vol. 66 Issue 4, p 2821

146 Tao, S.; Mazzotti, F. J.; Winstead, C. B; Miller, G. P.; The Analyst 125, no. 6 (2000): 1021-1023

147 H. Edner, G. W. Faris, A. Sunesson and S. Svanberg, Appl. Opt. 28, 921 (1989)

148 Omenetto, N.; Matveev, O.I.; *Resto*, W.; Badini, R.; Applied Physics B (Lasers and Optics), vol.B58, no.4, April 1994. pp. 303-7

149 Human, H.G.C.; Omenetto, N.; Cavalli, P.; Rossi, G.; Spectrochimica Acta, Part B (Atomic Spectroscopy), vol.39B, no.9-11, 1984. pp. 1345-63

150 Omenetto, N.; Human, H.G.C.; Spectrochimica Acta, Part B (Atomic Spectroscopy), vol.39B, no.9-11, 1984. pp. 1333-43

151 Rezaaiyaan, R.; Hieftje, G.M.; Anderson, H.; Kaiser, H.; Applied Spectroscopy, vol.36, no.6, Nov.-Dec. 1982. pp. 627-31

152 NIST Atomic Spectra Database, www.nist.gov

153 Boumans, P.W.J.M.; Vrakking, J.J.A.M.; Spectrochimica Acta, Part B (Atomic Spectroscopy), vol.42B, no.4, 1987. pp. 553-79

154 Miller, G.P.; Winstead, C.B.; Journal of Analytical Atomic Spectrometry 12, no. 9 (1997): 907

155 Kornblum, G.R.; De Galan, L.; Spectrochimica Acta, Part B (Atomic Spectroscopy), vol. 32B, no. 2, 1977. pp. 71-96

156 Miller, G.P., Baldwin, D.P., Zamzow, D.S. and Zhu Z, October 1998, "Air-ICP: A Molecular Solution to Measuring Exhaust Gas Toxic Metal Emissions", 25th FACSS Conference, Austin Texas

157 Miller, G.P., Wiser, R. and Tao, S., Baldwin, D.P., Zamzow, D.S., Eckels, D.E., October 1999, "Testing of a Continuous Sampling Air-ICP System as a Continuous Emission Monitor at the Diagnostic Instrumentation and Analysis Laboratory", Ames Laboratory-USDOE Report IS-5138

158 R. W. B. Pearse and A. G. Gaydon; “The Identification of Molecular Spectra”; London; Chapman and Hall ; New York : Wiley, 1976

159 L. E. Burkhart, G. L. Stukenbrocker, S. Adams, Phys. Rev. 75, 83 (1949)

160 R. K. Womge, V. J. Petterson, V. A. Fassel, Appl. Spectrosc. 33, 206 (1979)

161 R. A. Keller, R. Engelman, Jr. E. F. Zalewski, J. Opt. Soc. Am. 69, 739 (1979)

162 J. A. Goleb, Anal. Chem. 35, 1978 (1963)

163 J. A. Vera, G. M. Murray, S. J. Weeks and M. C. Edelson, Spectrochim. Acta 46B, 1689 (1991).

164 B. W. Smith, A. Quentmeier, M. Bolshov and K. Niemax, Spectrochim. Acta 54B, 943 (1999).

165 W. Pietsch, A. Petit, A. Briand, Spectrochim. Acta 53B, 751 (1998).

166 P. G. Russ III, J. M. Bazan, Spectrochim. Acta 42B, 49 (1987).

167 A. Montaser and D. W. Golightly, Inductively Coupled Plasma in Analytical Atomic Spectrometry, [VCH Publishers, Inc. 1992].

168 J. H. Aldstadt, J. M. Huo, L. L. Smith, M. D. Erickson, Anal. Chim. Acta 319, 135 (1996).

169 P. W. J. M. Boumans and J. J. A. M. Vrakking, Spectrochim. Acta 41B, 1235 (1986).

170 N. Omenetto, H. G. C. Human, P. Cavalli and G. Rossi, Spectrochim. Acta 39B, 115 (1984).

171 H. G. C. Human, N. Omenetto, P. Cavalli, and G. Rossi, Spectrochim. Acta, Part B 39, 1345 (1984)

172 J. A. Vera, G. M. Murray, S. J. Weeks, and M. C. Edelson, Spectrochim. Acta, Part B 46, 1689 (1991)

173 Chuji Wang, Fabio J. Mazzotti, George P. Miller, Christopher B. Winstead, Applied Spectroscopy, Vol. 57, No. 91167 (2003)

174 P. A. Voigt, Phys. Rev. A 11, 1845 (1975)

175 T.M. Bieniwski, J. Opt. Soc. Am. B 1, 300 (1984)

176 J. Blaise and L. J. Radziemski, Jr., J. Opt. Soc. Am. 66, 644 (1976)

177 Y. Su, C. Wang, F. J. Mazzotti, G. P. Miller, C. B. Winstead, and D. L. Monts, unpublished data

178 G. Gillson and G. Horlick, Spectrochim. Acta, Part B 41, 1299 (1986)

179 A. Montaser and D. W. Golightly, Inductively Coupled Plasma in Analytical Atomic Spectrometry, VCH Publishers, Inc., New York (1992)

180 J. M. de Regt, R. D. Tas, and J. A. M. van der Mullen, J. Phys. D: Appl. Phys. 29, 2404 (1996)

181 H. R. Griem, Plasma Spectroscopy, McGraw-Hill Inc, New York (1964)

182 De Regt, J.M.; Tas, R.D.; van der Mullen, J.A.M.; Journal of Physics D (Applied Physics), vol.29, no.9, 14 Sept. 1996. p. 2404-12

183 H. P. Dom, R. Neuroth, and A. Hofzumahaus, J. Geophys. Res., 1--, No D4, 7397 (1995)

184 A. Goldman and J. R. Gillis, J. Quant. Spectrosc. Radiat. Transfer, 25, 111 (1981)

185 W. C. Gardiner, editor, Combustion Chemistry, (Springer-Verlag, New York 1984)

186 D. R. Crosley, Combust. Flame, 78, 153 (1989)

187 G. Meijer, M. G. H. Boogaarts, R. T. Jongma, D. H. Parker, and A. M. Wodtke, Chem. Phys. Lett., 217, 112 (1994)

188 G. T. Linteris, V.D. Knyazev, and V. I. Babushok, Combustion and Flame, 129, No. 3, 221 (2002)

189 E. C. Rea, A. Y. Chang, and R. K. Hanson, J. Quant. Spectrosc. Radiat. Transfer, 37, 117 (1987)

190 C. O. Laux, T. G. Spence, C. H. Kruger, and R. N. Zare, Plasma Sources Science & Technology, 12, 125 (2003)

191 D. N. Shin, C. W. Park, and J. W. Hahn, Korean Chem. Soc., 21, 228 (2000)

192 Chuji Wang, F. J. Mazzotti, G. P. Miller, and C. B. Winstead, Appl. Spectrosc., 56, 386 (2002)

193 C. F. Su, T. Miller, F. Y. Yueh, and R. L. Cook, 34th AIAA Plasma Dynamics and Lasers Conference, 23-24 June, 2003, Orlando, Florida

194 J. J. L. Spaanhaars, J. J. ter Meulen, and G. Meijer, J. Chem. Phys., 107 (7), 2242 (1997)

195 A. McIlroy, Israel J. Chem., 38, 55 (1999)

196 P. A. Greet, W. J. R. French, G. B. Burns, P. F. B. Williams, and R. P. Lowe, K. Finlayson, Ann. Geophysics, 16, 77 (1998)

197 A. C. Eckbreth, Laser Diagnostics for Combustion Temperature and Species, Abacus Press, Tunbridge Wells, UK and Cambridge, US 1988

198 D. R. Crosley, NASA Conf. Pub., CP-3245 (1994)

199 J. Luque and D. R. Crosley, J. Chem. Phys, 109, 439 (1998)

200 C. Carlone and F. W. Dalby, Canada J. Phys., 47, 1946 (1969)

201 A. O'Keefe and D. A. G. Deacon, Rev. Sci. Instrum., 59, 2544 (1988)

202 K. W. Busch and M. A. Busch, editor, ACS symposium Series 720: Cavity Ringdown Spectroscopy: An Ultratrace-Absorption Measurement Technique, Oxford University Press (1999)

203 K. K. Lehmann, US Patent number 5,528,040 (1996)

204 G. P. Miller and C. B. Winstead, "Cavity Ringdown Laser Absorption Spectroscopy", invited chapter in Encyclopedia of Analitycal Chemistry: Instrumentation and Applications, 10734, Ed. R.A. Meyers: John Wiley & Sons Ltd, Chichester, UK (2000)

205 G. Berden, R Peeters, and G. Meijer, International Reviews in Physical Chemistry, 19, 4, 565 (2000)

206 D. B. Atkinson, Analyst, 128, 117 (2003)

207 R. T. Jongma, M. G. H. Boogaarts, I. Holleman, and G. Meijer, Rev. Sci. Instrum., 66 (4), 2821 (1995)

208 S. Cheskis, I. Derzy, V. A. Lozovsky, A. Kachanov, and D. Romanini, Appl. Phys. B, 66, 377 (1998)

209 V. A. Lozovsky, I. Derzy, and S. Cheskis, Chem. Phys. Lett., 284, 407 (1998)

210 X. Mercier, E. Therssen, J. F. Pauwels, and P. Desgroux, Chem. Phys. Lett., 299, 75 (1999)

211 M. C. Van Beek and J. J. Ter Meulen, Chem. Phys. Lett., 333, 237 (2001)

212 Wang Chuji, Mazzotti Fabio J., Koirala Sudip P., Winstead Christopher B., Miller George P., Applied Spectroscopy 58, no. 7, 784-791 (2004)

213 P. Zalicki and R. N. Zare, J. Chem Phys., 102 (7), 15 (1995)

214 J. T. Hodges, J. P. Looney and R. D. van Zee, Appl. Opt. 35, 4112 (1996)

215 J. T. Hodges, J. P. Looney and R. D. van Zee, J. Chem. Phys. 105 (23), 10278 (1996)

216 J. Luque, LIFBASE, Window version 1.9.130 (2003)

217 A. Montaser and D. W. Golightly, Inductively Coupled Plasma in Analytical Atomic Spectrometry, VCH Publishers, Inc. (1992)

218 D. S. Baer and R. K. Hanson, J. Quant. Spectrosc. Transfer, 47 (6), 455 (1992)

219 F. H. A. G. Fey, W. W. Stoffels, J. A. M. van der Mullen, B. van der Sijde, and D. C. Schram, Spectrochim. Acta, 46B, 855 (1991)

220 E. L. Bydder and G. P. Miller, Spectrochim. Acta 43B, 819 (1988)

221 G. P. Miller, Spectrochim. Acta 44B, 395 (1989)

222 E. L. Bydder and G. P. Miller, Spectrochim. Acta 44B, 165 (1989)

223 M. M. Prost, Spectrochim. Acta 37B, 541 (1982)

224 M. W. Blades, Applied Spectrosco. 37, 371 (1983)

225 P. Yang and R. M. Barnes, Spectrochim. Acta 44B, 561 (1988)

226 S. Nakamura, Spectrochim. Acta part B 54, 1899 (1999)

227 R. Peeters, G. Berden, and G. Meijer, Appl. Phys. B 73, 65 (2001)

228 Chemistry Webbook, NIST, http://webbook.nist.gov/chemistry

229 B. Bakowski, G. Hancock, R. Peverall, G. A. D. Ritchie, and L. J. Thornton; J. Phys. D: Appl. Phys. 37 (2004) 2064–2072